ELASTIC PROPERTIES OF POROUS SILICON SUPERLATTICES

ANNA MARIA POLOMSKA


CENTRE FOR NFLD. STUDIES
MEMORIAL UNIVERSITY
OF NEWFOUNDLAND

Elastic Properties of Porous Silicon Superlattices

by

Anna Maria Polomska

A Thesis Submitted in Partial Fulfilment of
the Requirements for the Degree of

Doctor of Philosophy

Department of Physics and Physical Oceanography
Memorial University of Newfoundland

January, 2010

St. John's Newfoundland

Abstract

The elastic properties of porous silicon single layers and superlattices were determined by means of Brillouin light scattering. The quality of the Brillouin spectra dependent on the porosity of the porous layer and significant improvement was observed with the increase of porosity. The morphology and thicknesses of the porous silicon films were studied using scanning electron microscope. The porosity of both single and multilayered films was calculated using gravimetric method.

The elastic constants of p-Si superlattices composed of layers of various porosity were compared to values of effective elastic constants obtained from the model proposed by Grimsditch and Nizzoli [M. Grimsditch and F. Nizzoli, Phys. Rev. B, **33**, 8, 5891, 1986] which was reported to be applicable for other types of semiconducting superlattices. As the model requires the elastic constants of the constituent layers of the superlattice as input, the set of elastic constants was determined for each single porous silicon layer assuming cubic symmetry.

The bulk phonon velocities and respective elastic constants of single layers and superlattices decreased with increasing average porosity of the film. The effective elastic constants of the superlattices were calculated directly from the spectra collected at smallest incident angle as well as obtained through the fitting of data with expressions for angular dependence of the velocities of the bulk phonons. The fitting was done with and without constraints on the values of elastic constants ($c_{11} > c_{33}$).

The longitudinal and transverse elastic constants of the superlattice (c_{33} and c_{44}) showed excellent agreement with the model for all the approaches, while the values of c_{11} and c_{13} agreed only when the constraints were imposed.

Based on the results only partial agreement with a model may be concluded. An excellent agreement for two elastic constants for all superlattices may either mean the other two cannot be determined due to uncertainties involved in the experiments or that the model needs corrections in order to work for superlattices created by electrochemical etching of a crystalline parent wafer.

Acknowledgments

Dr. Todd Andrews, *supervisor*, to making sure that

> *Our imagination is stretched to the utmost, not, as in fiction, to imagine things which are not really there, but just to comprehend those things which 'are' there.*
>
> [R. Feynman]

And then, in the order of appearance

Mamuś, *mom*, for constantly reminding me that

> *Patience and perseverance have a magical effect before which difficulties disappear and obstacles vanish.*
>
> [J.Q. Adams]

Ojciec, *dad*, for making me remember that

> *Life is not a matter of holding good cards, but of playing a poor hand well.*
>
> [R. L. Stevenson]

Late and missed Babcia Jania, *Nan*, and Babcia Marysia, *Nan*, for teaching me that

> *One ought to know how to walk on the sunny side of life.*
>
> [M. Rodziewiczówna]

Miszczu Połom, *brother*, for knowing before I even had a chance to read that

> *Fear is the original sin. Almost all of the evil in the world has its origin in the fact that some one is afraid of something.*
>
> [L. M. Montgomery]

Marek Bromberek, *Maareek*, Lance Parsons and Jordan Peckham, *Sheldon & Leonard*, so even now

> *I think physicists are the Peter Pans of the human race. They never grow up and they keep their curiosity.*
>
> [I. I. Rabi]

Tim Harlick, *Gilbert Blythe, Howard Roark and Mr. Darcy*, because

> *To say "I love you" one must first know how to say "I".*
>
> [A. Rand]

Contents

List of Tables

List of Figures

List of Symbols

A - area of the etched sample

α - anisotropy ratio

c_{ijkl}, c_{IJ} - elastic stiffness constant

C - contrast

$d^{[\zeta]}$ - thickness of the constituent layer in SL

δ_{ij} - Kronecker's delta

δx_i - uncertainty in value of x_i

e_r - etch rate

ε - dielectric permittivity

$f_{\#}$ - ratio of lens focal length to its diameter

$f^{[\zeta]}$ - thickness ratio of the constituent layer in SL

F - body force

$\mathfrak{F}$ - finesse

G - body torque

Γ_{ij} - Kelvin–Christoffel matrix

γ_{ij} - empirical parameter describing dependence of elastic constant $c_{ij}onporosity$

$\gamma_{T,L}$ - empirical parameter describing dependence of phonon velocity $v_{T,L}onporosity$

γ_Y - empirical parameter describing dependence of Young's modulus on porosity

h - layer thickness

eta - real part of the refractive index n

i - imaginary number defined as $\mathrm{i}^2 = -1$

I - electric current

j - electric current density

k - wave vector

k_i - incident light wave vector

k_s - scattered light wave vector

κ - imaginary part of the refractive index n

l_i - direction cosines

L_i - mirror spacing

Λ - modulation wavelength (period) of the superlattice

λ - acoustic phonon wavelength

λ_i - incident light wavelength

λ_s - scattered light wavelength

m - mass

$\boldsymbol{M}$ - transformation matrix between the strain tensors

$\boldsymbol{\mu}$ - strain tensor

n - refractive index

$\hat{\boldsymbol{n}}$ - vector parallel to the normal

ν - bulk phonon frequency

ν_i - incident light frequency

ν_R - surface phonon frequency

ν_s - scattered light frequency

ν_F - free spectral range

N - refractive index of crystalline silicon

ν - frequency of bulk acoustic phonon

ν_R - frequency of surface acoustic phonon

∇ - nabla

∇_{iJ} - divergence of the stress tensor

∇_{Ij} - symmetric gradient operator

ω - angular frequency

$\boldsymbol{q}$ - acoustic phonon wave vector

$\boldsymbol{r}$ - position of an arbitrary point in the medium

r_x, r_y, r_z - components of $\boldsymbol{r}$ with respect to rectangular coordinate system

$\boldsymbol{R}$ - new position of an arbitrary point in the medium

R_x, R_y, R_z - components of $\boldsymbol{r}$ with respect to rectangular coordinate system

ρ - density of the material

S - surface

$\boldsymbol{\sigma}$ - stress tensor

t - time

T - traction force

θ - scattering angle

θ_i, θ_i' - incident angle

θ_s, θ_s' - angle between the normal and scattered light

$\boldsymbol{u}$ - displacement vector

U_S - elastic energy

$\boldsymbol{v}$ - velocity of the particle

v_L - velocity of longitudinal bulk phonon

v_R - velocity of surface Rayleigh phonon

v_T - velocity of transverse bulk phonon

v_- - velocity of quasi-transverse bulk phonon v_+ - velocity of quasi-longitudinal bulk phonon V - volume

x - axis in the Cartesian (orthogonal) coordinate system indicating [100] direction

$\hat{x}$ - unit vector along x-axis

ξ - porosity of the p-Si layer

y - axis in the Cartesian (orthogonal) coordinate system indicating [010] direction

$\hat{y}$ - unit vector along y-axis

Y - Young's modulus

z - axis in the Cartesian (orthogonal) coordinate system indicating [001] direction

$\hat{z}$ - unit vector along z-axis

List of Abbreviations

A - aperture

BF - bandpass filter

BLS - Brillouin light scatering

c-Si - crystalline silicon

f - collecting lens

FPI - Fabry-Pérot interferometer

FSR - free spectral range

FWHM - full width at half maximum

L - lens

LGM - longitudinal guided mode

M - mirror

P (PR) - prism

p-Si - porous silicon

QL - quasi-longitudinal bulk phonon

QT - quasi-transverse bulk phonon

S - sample

SL - superlattice

SEM - scanning electron microscopy

TFP-1 - tandem Fabry-Pérot interferometer

VNDF - variable neutral density filter

Chapter 1

Introduction

1.1 Overview of Early Work

The fact that the electrochemical etch of monocrystalline silicon wafers under the appropriate conditions leads to the formation of porous silicon (p-Si) was discovered and first reported by Uhlir in the fifties [1] while studying electropositive of silicon in solutions of hydrofluoric acid. The discovery of p-Si was initially of limited interest but the attraction to the material was renewed when the idea of formation of silicon on insulator structures was presented in the early seventies [2]. The attractiveness of p-Si boomed with the discovery of visible room temperature photoluminescence in 1990 [3]. The material drew attention yet again when its biocompatibility [4] and biodegradability [5] were shown.

1.1.1 Properties of Porous Silicon

A piece of silicon in an HF-based electrolyte behaves like a Schottky diode [6] and under reversed bias (anodic or cathodic for n- and p-type Si, respectively) a space charge region is present in the Si electrode. The studies of current - voltage curve on the junction shows that the formation of p-Si is possible if the Si wafer is biased and current densities are below critical values. Additionally, in case of n-type or semi-insulating p-type Si, light must be supplied [7].

The etching process of p-Si is self-limited (which means that the electrochemical etching occurs mainly at the pore tips [6] and the already formed porous structure is not affected other than by a slight chemical etching [7]) and the etch rate is a linear function of current density for fixed electrolyte composition [8]. The porosity ξ of the etched layer, defined as the percentage of void space in the material [9], depends on the current density j (increase of ξ with increasing j), electrolyte composition (decreasing ξ with increasing [HF]) and the doping of the parent crystalline silicon substrate [7].

The pore morphologies depend primarily on the dopant type and its concentration in the parent c-Si wafer. Typical, although rough characteristics of different types of p-Si are summarized in Table 1.1. The size of the pores is independent of their morphology [10] and accordingly qualifies the pores into one of the three categories - macropores, mesopores and micropores. Macroporous Si has pores and interpore distances larger than 50 nm, mesoporous Si is characterized by dimensions between

10 and 50 nanometers and in microporous Si pore sizes are below 10 nm.

The crystalline structure of p-Si samples is the same as that of silicon crystals [14] - diamond structure consisting of two intercepting cubic face centered lattices displaced along the cell diagonal by a quarter of the length [15]. A detailed study of p-Si carried out by Pickering et al. [16] however, showed differences in morphological properties in the layers formed in degenerate or non-degenerate c-Si of resistivity in the range of 0.01-25 Ω cm. In the case of degenerate samples (in which the number of electrons in the conduction band approaches that of a metal) the resulting layer morphology was a network of $\sim$10 nm pores that under optimum conditions retain the single crystal character of the original material. The studies of non-degenerate p-Si indicate the existence of amorphous phases. Porous silicon is also characterized by a high surface to volume ratio (a few hundreds square meters per cubic centimeter [17]). Additionally, the surface of p-Si can be locally activated by irradiation so it can react with various chemicals [18].

The conductivity of p-Si in meso- and microporous layers is a few orders of magnitude lower than the crystalline substrate. This phenomenon in microporous layers is associated with quantum confinement of charge carriers, whereas in the structures

Table 1.1: Morphologies of porous silicon.

Type	Pore Size [nm]	Morphology
n^+	100-1000	preferential pore growth along high symmetry directions [11]
n^-	10-100	preferential pore growth along high symmetry directions [11]
p^+	10-100	branched, ordered, preferred growth in [001] direction [12], [13]
p^-	<10	interconnected network uniformly distributed over the film [12]

with pores of larger dimensions the increase in electric resistance is explained by a model based on constrictions of conductive paths by surface traps [19]. As the differences in structural properties of p-Si, controlled in the formation process, result in the diversity of electrical properties of the material [20], the latter one can be tailored accordingly. The reports on thermal conductivity provide data varying over a wide range [21] depending on the morphology of the films and conditions in which they were prepared, but show generally that it is lower than that of c-Si.

The luminescence of p-Si consists of three bands - blue, visible and infrared [22]. The first one is observed from hydrothermally etched p-Si after oxidation [23] and from electrochemically etched p-Si that was illuminated with white light after anodization [24]. The visible band can be observed from wafers subjected to both electrochemical etching and chemical dissolution and is associated with widening of the Si bandgap through quantum confinement [3]. The luminescence in the infrared was reported in samples prepared by high-temperature oxidation of porous silicon [25].

The interest in p-Si is nowadays driven not only by the adjustable and controllable properties described above but also by the fact that its applications cover a wide spectrum, from mechanics through biotechnology, electronics and energy, to use in chemical sensing and optics [26, 27]. The use of p-Si in some applications is limited by the elastic properties of this material and by its mechanical instability observed, for example, during the drying process [28].

In mechanics, one of the very few large scale applications p-Si layers is in the

fabrication of SOI layers [29]. The sensitivity of the pore size to dopant concentration and the wide range of elastic constants values allow creation of a wide range of pore and crystallite sizes. Electrochemical pore formation is used to micromachine precise structures yielding straight walls to depths of as much as 150 μm with high aspect ratio [30], bridges, membranes and cantilevers [31].

Porous silicon is also used in the field of biotechnology for filters [32] and determination of particle size [33] due to the consistent and regulated pore size, especially in the case of meso- and macroporous silicon. Additionally, the regularity of macropore arrays in Si makes it useful for biochips. The p-Si photonic structures offer advantages that can be useful for biomolecular screening and medical diagnostics [34]. The growth of mammalian cells [35], phosphates and biological species in the presence of protein [36] was observed on nanostructured Si and membranes. It has been shown that macroporous silicon provides an environment for adhesion and growth of osteoblasts and collagen fibers which, together with high mineralization rate, make it a promising material for bone tissue engineering [37]. Additionally p-Si can find use in technological applications such as biosensors which release drugs or essential chemicals depending on the chemical environment. Due to their biocompatibility and biodegradability, p-Si bilayers provide continuous drug release and can be used for anticancer agent delivery [38] and as insulin providers [39]. Porous silicon layers with fine pore distribution are expected to enhance catalytic activity and have been considered as a coupling matrix for enzyme reactors integrated with Si [40] and modified

surfaces of p-Si layers are employed for selective binding of proteins from complex mixtures [41].

In microelectronics p-Si finds use as a buffer layer [2] and as high quality, stable capacitors [42], fully compatible with Si technology. They combine an electrochemically enlarged surface and superior dielectrics.

In the field of energy p-Si finds use in solar cells both in surface texturization which results in increased efficiency, antireflection coating [43] and as gettering sites for impurities diffusing from the bulk [44]. Porous silicon is also used for fabrication of fuel cells for portable electronic devices [45]. Microporous silicon filled with an oxidizer creates a very potent explosive due to the huge surface area [46].

Chemical and biological sensing makes use of the fact that pore surfaces are sensitive to only certain materials which by binding to p-Si single and multilayered films change their properties. This thereby permits determination of the presence and level of concentration of the substance in the environment. Taking advantage of a change in electrical resistance upon exposure to the environment allows the use of p-Si single layers in chemical sensors sensitive to organic gases [47], the presence of pollutants, humidity [48] and as little as 0.5 ppm benzene [49]. The change in the Bragg wavelength of multilayered p-Si films when in contact with chemicals allows production of small inexpensive detectors [50]. Carefully tailored p-Si was shown to work as biosensors activated by enzymes (glucose) [51].

Due to its interesting optical properties p-Si is considered a promising photonic

material. The particular type of p-Si that finds application in optical components are p-Si multilayered films, including those characterized by a modulation length Λ significantly smaller than the wavelength of the visible light [7]. One dimensional p-Si photonic crystals are used as building blocks for optical modulators [52]. Bragg mirrors [53], surface wave structures [54], Fabry-Pérot interference filters [55], narrow band filters [56] light emitting diodes, optical switches [57], grating structures [58] and refractometers [59] have been realized using p-Si-based multilayered films. Bragg filters and Fabry-Pérot interference structures made from p-Si were also investigated for suitability in sensing applications [60] while randomly structured p-Si multilayered stacks can serve as the ideal material for optical modeling [61].

1.1.2 Elastic Properties of Porous Silicon Single Layers

As the focus of this work is on the elastic properties of p-Si single layers and superlattices, the work done to date regarding the mechanical properties of the material was examined more carefully. Considering the range of porosities, morphologies and doping levels of the material the research area is extensive. Many of the reports include comprehensive work, investigating the changes of the elasticity of the p-Si layers with porosity, layer thickness or dopant type.

Investigations of porous silicon by means of X-ray diffraction by Barla [62] showed that the material behaves like a nearly perfect crystal. The mismatch between the p-Si and c-Si lattice parameters and Young's modulus were determined for layers of

various porosity. Measurements of the microhardness (the hardness of a material as determined by forcing an indenter into the surface of a material under very light load [63]) of p-Si suggest that there is no connection between the morphology of the layers and the hardness. The influence of the crystalline substrate on the p-Si layer is pointed out as the Vickers parameter (ability of material to resist deformation [64]) decreases with increasing layer thickness and porosity [13].

The investigation of elastic properties of p-Si single layers shows dependence of the values of the elastic constants on the porosity of the samples. Da Fonseca *et al.* [65], [66] used high frequency microechography and acoustic signature in order to characterize p-Si layers. Analysis of the porosity dependence of the surface Rayleigh and bulk transverse and longitudinal modes suggested that their velocities decreased linearly with increasing porosity.

Andrews *et al.* [67] determined the elastic stiffness constants of a p^+ type 30% porous layer using the Brillouin light scattering technique. This study also showed that single layers of p-Si are not isotropic, as often approximated while investigating the elastic properties of the material, but retain the cubic symmetry of the parent material.

Brillouin light scattering was also used to investigate the elastic properties of p-Si by Beghi *et al.* [68]. The work describes the study of low porosity n- and high porosity p-type p - Si and explores the physical properties of a 1 μm thick region. For n-type p-Si layers the authors observed broadening of the peak due to longitudinal mode and

its shift towards lower frequencies, disappearance of the peak due to the transverse mode, and shift towards lower frequencies of the peak assigned to the Rayleigh surface mode. The reported velocity of the bulk longitudinal phonon was found to be higher than that of c-Si. This was attributed to a skin layer with porosity lower than the nominal porosity of the film. No bulk peaks were observed from high porosity p-type layers but the presence of three surface peaks was reported.

Brillouin spectroscopy of p-type p-Si has shown two well resolved acoustic phonon peaks associated with the surface and film modes of the thick ($\sim$25 μm) 80% porous, (100) oriented layers investigated by Lockwood *et al.* [69]. The morphology of the samples, determined using transmission electron microscopy and Raman scattering, resembles interconnected spheres with diameters of order of 3 nm. The bulk phonon velocities were estimated using the porosity dependence of the phonon velocity presented by Da Fonseca [65]. It is also noted that the intensity of scattered light is at least order of magnitude larger than that from c-Si. This is attributed to the fact that a sample of such high porosity is transparent to the excitation wavelengths. Both ripple and elasto-optic mechanisms of scattering are present, resulting in a substantial increase in the intensity.

A systematic study of acoustic modes in p-Si with porosity varying from 57% to 83% and layer thickness from 1 to 22 μm, prepared from (100) oriented, p-type Si was carried out by Fan *et al.* [70]. Three acoustic modes were observed: surface Rayleigh, bulk transverse and bulk longitudinal. The bulk phonon velocities were

found to decrease with increasing layer thickness, approaching an asymptotic value for films thicker than 10 μm. This was attributed to the presence of a transition layer between the p-Si layer and the crystalline substrate within which its elastic properties vary from those of the p-Si to those of c-Si. The surface Rayleigh mode was found to be nearly independent of thickness for layers thicker than 10 μm. The almost linear decrease of velocity with increasing porosity in thick layers (>10 μm) agrees with the prediction made by da Fonseca [65]. In addition, elastic constants of p^+ (heavily doped) 70% porous layers are determined assuming elastic isotropy.

The same group [71] performed Brillouin light scattering experiments to probe the acoustic properties of chemically modified p-Si films. It was shown that passivation with organic chain compounds changes the frequency shift of the peaks originating from the acoustic modes. The character of the changes depends on the mass, chain length and the presence of the dipole moment of the molecules as well as to the type of bond that it creates with the p-Si film.

Andrews *et al.* [72] used Brillouin light scattering spectroscopy to study the propagation of surface Rayleigh phonon in low porosity, heavily doped layers. For all studied layers the Rayleigh surface phonon velocity was found to be lower than that for c-Si and exhibited weak or negligible dispersion. The porosity dependence of the velocity is related to the resistivity of the substrate. The porosity dependence of the surface Rayleigh phonon velocity for layers formed from c-Si substrates with resistivity smaller than 0.01 Ω cm is different from that of porous layers fabricated from c-Si

with resistivity larger than 0.01 Ω cm. This difference is attributed to the combined effects of rapid native oxidation of the lightly p-doped layers compared to heavily p-doped layers and differences in porosity gradient and morphology.

A study of p-Si films of comparable porosity, formed from p^-, p^+ and n^+ c - Si was done by Andrews *et al.* [73]. The morphology and geometry of the pores exhibited by the films were found to influence the values of the acoustic phonon velocities. The elastic stiffness constants and the Young's modulus (assuming elastic isotropy) calculated for ~60% porous p^- (lightly doped) silicon film were found to be nearly three times smaller than those obtained from p^+ samples of the same porosity.

A recent report by Aliev *et al.* [74] of acoustic transmission measurements of the longitudinal phonon velocities in heavily doped, (100) p-type porous Si layers of porosity between 25% and 85% show dependence on the porosity. The velocities obtained for heavily doped samples are higher than those reported for lightly doped ones. The fit parameters of the empirical equation relating the velocity of the bulk phonon and porosity, proposed by da Foncesa [65], suggested also the porous layer had a relatively well-ordered structure.

1.2 Elastic Properties of Multilayered Structures

Most studies of the elastic properties of multilayered films have been carried out in metallic superlattices (SL). This is because of the significant changes of the elastic constants with variation of the modulation wavelength. The behavior of the elastic

moduli depended on the modulation wavelength and on the materials that make up the superlattice. However, while most previous BLS studies of superlattices have focused on the metallic ones due to anomalies in their elastic properties [75–81] there have been some studies on semiconducting superlattices.

GaAs/$Ga_{1-x}Al_xAs$ superlattices with periods ranging from 45 Å to 250 Å were examined by Raman and Brillouin scattering [82]. The surface-wave velocities obtained from the measurement were slightly higher than the value calculated for the mean homogeneous medium. It was suggested that the reason for the difference is the stresses in the alternating layers that comprise the SL.

Similar GaAs/AlAs films of nonmetallic character were investigated using BLS to determine elastic constants for both constituent GaAs and AlAs layers and the superlattice [83]. The sound velocities and the elastic constants were found to be independent of the modulation wavelength of the superlattice up to ~100 nm. The elastic constants of the constituent layers were used to obtain the effective elastic constants of the SL according to the Grimsditch-Nizzoli model [84] and the experimental values were found to be in agreement with the model values within uncertainty for all modulation wavelengths. No anomaly in elastic properties was observed.

BLS experiments of semiconducting a-Si:H/a-$SiHN_x$:H Fibonacci quasiperiodic multilayered films with different numbers of sequences [85] were performed. The observation of the surface Rayleigh mode allowed the evaluation of effective elastic constant c_{44}. The Grimsditch-Nizzoli model [84] was modified for this kind of mate-

rial [86] and the calculated values of c_{44} for the case of such quasiperiodic systems showed good agreement with experiment. No elastic anomaly was observed in these structures. Meanwhile, in the study of amorphous a-Si:H/a-SiN_x:H superlattices, the surface velocity was found to depend not on the modulation wavelength but only on the relative thickness ratios of the constituent layers [87].

BLS was also used to investigate the elastic properties of a family of polymeric Langmuir - Blodgett films (stacks of amphiphilic organic molecules deposited monolayer after monolayer). In these films the first layer was made of a polyglutamate backbone molecule and is of hexagonal symmetry, with the z-axis in the plane of the film while the second layer is built of hydrocarbon side-chain molecules and is assumed to be isotropic [88]. The resulting multilayered film had orthorombic symmetry but it was assumed to be hexagonal in the analysis of Brillouin spectra and determination of phonon velocities and elastic constants. With both bulk and surface modes observed [89] a complete set of elastic constants was determined and were found to independent of the numbers of layers when the film consisted of more than 10 layers. The ratios of transverse elastic constants, c_{44}/c_{66}, and longitudinal elastic constants, c_{11}/c_{33} were found to be lower than for ordinary solids. The study showed a decrease in each of the effective elastic constants c_{11}, c_{12}, c_{13}, c_{33}, c_{55} and c_{66} with an increasing monolayer thickness. With the exception of c_{33}, the effective elastic constants determined using the Grimsditch-Nizzoli model [84] assuming hexagonal symmetry of the superlattice, showed good agreement with the experimental values.

The analysis also yielded the individual layer thickness with an excellent accuracy.

Forrest *et al.* [90] used BLS to investigate the mechanical properties of thin polystyrene and polyisoprene films incorporated in a multilayers. Their results showed good agreement between the measured elastic constants and those calculated using Grimsditch-Nizzoli [84] model. The agreement held even when the layer thicknesses were significantly smaller than the unperturbed size of the polymer molecules. The result suggest that the mechanical properties of the polymers change very little when the molecules are forced into confined geometries.

Simplification of the symmetry was also used by Carlotti [91]. In this work, the structure of tetragonal $In_{0.5}Ga_{0.5}As/InP$ superlattices were approximated to be cubic. The elastic constants, determined using BLS technique, agreed with the theoretical ones calculated using the Grimsditch-Nizzoli model.

The Grimsditch-Nizzoli model was also used to determine effective elastic constants of various superlattices with constituent layers made of single atom materials and agreement between the theory and experiment has been reported. Such agreement is reported in case of Si_m/Ge_n superlattices [92], where m and n denote the number of deposited monolayers. The elastic constants tensor of the constituent layers and of the Si/Ge superlattice was determined using the angular dependence of the surface acoustic phonon velocity. The symmetry of the films was assumed by the authors to be cubic.

Superlattices made of Si and Ge constituent layers with modulation wavelengths

between 1.4 nm and 5.6 nm with different thickness ratio of the constituent layers were studied by means of BLS by de Bernabé *et al.* [93]. The elastic constants tensor was calculated using the Grimsditch-Nizzoli model assuming the tetragonal symmetry of the superlattice. The magnitude of the differences between elastic constants c_{11} and c_{33} and c_{44} and c_{66} justified the approximation of the symmetry as cubic. This assumption was kept in an extension of that study [94]. No anomalies in behaviour of elastic constants were observed. The values for elastic constants c_{44} were determined and a comparison to the effective elastic constants was made. It was found that for the theoretical and experimental values of elastic constants of Si_{4n}/Ge_n and Si_{3n}/Ge_n superlattices agreed within uncertainty whereas for Si_n/Ge_n, Si_n/Ge_{3n} and Si_n/Ge_{4n} structures the measured values of c_{11} exceeded the calculated ones by up to 14%. The differences between the superlattices and the lack of agreement with the Grimsditch-Nizzoli model for some of them was explained by the differences in the interfaces (relaxed Si-Ge alloy for Si_m/Ge_n with m>n structures versus compressed Si-Ge alloys for Si_m/Ge_n with m$\leq$n with distances equal to Ge-Ge and Si-Si ones, respectively).

Preliminary results of the work presented in this thesis [95] showed crude agreement between the effective elastic constants calculated using Grimsditch-Nizzoli model and determined experimentally via BLS from p-Si superlattices. The reason for the lack of agreement is at the moment unknown, however it could be associated with poor quality of the layer of lower porosity and the approximation of the single layers by isotropic material.

1.3 Overview of the Present Work

In the present work the elastic properties of p-Si single layers and superlattices have been investigated using the Brillouin light scattering technique. The primary goal of this work is to determine the elastic properties of p-Si superlattices composed of layers of various porosities and to compare them to values obtained from the model for effective elastic constants proposed by Grimsditch and Nizzoli [84]. It is noted that this model requires as input the elastic constants of the constituent layers of the SL. The morphology and thicknesses of the porous silicon films were studied using scanning electron microscopy (SEM). A gravimetric method was used to determine the porosity of single layer films and hence the SL constituent layers.

The importance of this research on a fundamental level lies largely in the fact that p-Si superlattices differ significantly from other types of semiconducting multilayered films. They are created from the same original crystalline material by etching the consecutive layers. The direction of layer creation is reversed, i.e. rather than depositing materials on the top of each other, the layers are etched starting from the top of the sample. The obtained structures consist of crystalline silicon and pores filled with air. The constituent layers keep the cubic symmetry of the parent material but are not uniform. Furthermore, the validity of the effective medium model could be influenced in case of this system due to its porous structure. Although there is no definite periodicity in the plane of the layers, for the modulation wavelength Λ of tens of nanometers the pore sizes become comparable with the layer thickness. The

investigated superlattices consist of 250 bilayers. One of the constituent layers in the bilayer is always kept the same (59%) while the other changes for each superlattice, ranging in porosity from 33% to 72%. Such a porosity range is selected to investigate not only the suitability of the model in describing this particular system but also the possible dependence of elastic constants on morphology of the layers and porosity combinations.

In addition to current applications (Bragg mirrors, rugate filters, microcavities, waveguides, etc.) p-Si superlattices gain importance as acoustic band devices. The band gap is attributed to contrast in the elastic properties of the constituent layers [96] and the propagation of acoustic waves can be completely suppressed in the characteristic bandwidth [97]. The knowledge of constituent and effective elastic constants is therefore crucial for this kind of material.

Chapter 2

Theory

2.1 Elasticity Theory

The position of any arbitrary point in a continuous medium in equilibrium can be defined by an equilibrium position vector $\boldsymbol{r} = r_x\hat{x} + r_y\hat{y} + r_z\hat{k}$, where r_x, r_y and r_z are components of $\boldsymbol{r}$ with respect to a rectangular coordinate system. When the points are displaced from their equilibrium positions the body either undergoes a rigid transformation (translation or rotation) or is deformed (strained) [98]. The new position vector can be defined as $\boldsymbol{R}$ with coordinates R_i that are functions of the components of the equilibrium position vector r_i [99]. The displacement $\boldsymbol{u}$ of a particle located at $\boldsymbol{r}$ in the equilibrium state, as shown in Fig. 2.1 is then defined as

$$\boldsymbol{u}(r_i) = \boldsymbol{R}(r_i) - \boldsymbol{r}(r_i), \tag{2.1}$$

where $i = x, y, z$.

The displacement of a given point in the medium is determined if the displacement

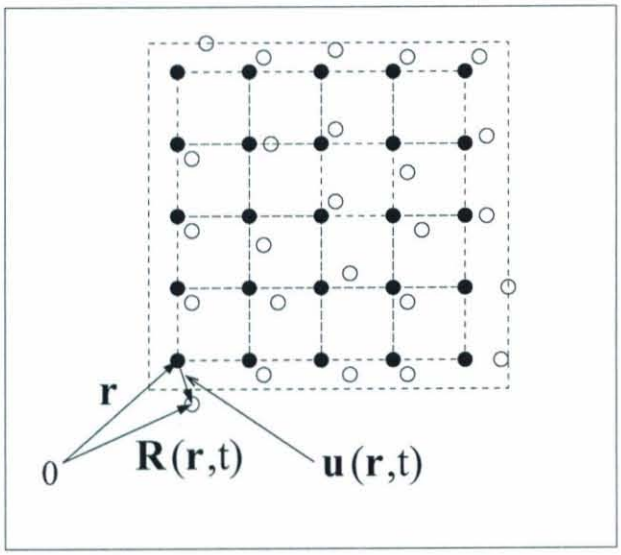

Figure 2.1: Position of a point in a continuous medium in equilibrium and in a deformed state.

vector $\boldsymbol{u} = \boldsymbol{u}(r_i, t)$ is given. The displacement vector $\boldsymbol{u}$ itself is not enough to define the transformation, however, as it has nonzero values for both material deformations and rigid transformations. A quantity that remains zero for all combinations of rigid rotations and translations but is nonzero for deformations is the differential form of (2.1) at constant time [100]

$$d\boldsymbol{u}(r_i) = d\boldsymbol{R}(r_i) - d\boldsymbol{r}(r_i). \tag{2.2}$$

Deformation is, however, usually defined by a more convenient quantity that also meets the conditions of being non-zero for deformations while remaining zero for

translations and rotations, namely $d\boldsymbol{u}^2$:

$$\begin{aligned} d\boldsymbol{u}^2 &= d\boldsymbol{R}^2(r_i) - d\boldsymbol{r}^2(r_i) \\ &= (dR_x)^2 + (dR_y)^2 + (dR_z)^2 - (dr_x)^2 - (dr_y)^2 - (dr_z)^2. \end{aligned} \tag{2.3}$$

Solving equation (2.2) for $d\boldsymbol{R}$ one obtains for each individual component

$$dR_i = du_i + dr_i \tag{2.4}$$

so Eq. (2.3) can be rewritten as

$$\begin{aligned} d\boldsymbol{u}^2 &= (du_x + dr_x)^2 + (du_y + dr_y)^2 + (du_z + dr_z)^2 - (dr_x)^2 - (dr_y)^2 - (dr_z)^2 \\ &= (du_x)^2 + 2du_x dr_x + (du_y)^2 + 2du_y dr_y + (du_z)^2 + 2du_z dr_z. \end{aligned} \tag{2.5}$$

Each ordinary differential element can be written as the sum of partial derivatives, i.e. $du_x = \frac{\partial u_x}{\partial r_x}dr_x + \frac{\partial u_x}{\partial r_y}dr_y + \frac{\partial u_x}{\partial r_z}dr_z$. Using Einstein's summation convention $du_i = \frac{\partial u_i}{\partial r_k}dr_k$ where $i, k = x, y, z$. Eq. (2.5) takes then the form

$$\begin{aligned} d\boldsymbol{u}^2 = &(\tfrac{\partial u_x}{\partial r_x}dr_x + \tfrac{\partial u_x}{\partial r_y}dr_y + \tfrac{\partial u_x}{\partial r_z}dr_z)^2 + 2(\tfrac{\partial u_x}{\partial r_x}dr_x + \tfrac{\partial u_x}{\partial r_y}dr_y + \tfrac{\partial u_x}{\partial r_z}dr_z)\, dr_x \\ &+ (\tfrac{\partial u_y}{\partial r_x}dr_x + \tfrac{\partial u_y}{\partial r_y}dr_y + \tfrac{\partial u_y}{\partial r_z}dr_z)^2 + 2(\tfrac{\partial u_y}{\partial r_x}dr_x + \tfrac{\partial u_y}{\partial r_y}dr_y + \tfrac{\partial u_y}{\partial r_z}dr_z)\, dr_y \\ &+ (\tfrac{\partial u_z}{\partial r_x}dr_x + \tfrac{\partial u_z}{\partial r_y}dr_y + \tfrac{\partial u_z}{\partial r_z}dr_z)^2 + 2(\tfrac{\partial u_z}{\partial r_x}dr_x + \tfrac{\partial u_z}{\partial r_y}dr_y + \tfrac{\partial u_z}{\partial r_z}dr_z)\, dr_z. \end{aligned} \tag{2.6}$$

After expanding each expression and using the summation convention mentioned above, Eq (2.6) can be written as

$$d\boldsymbol{u}^2 = 2\frac{\partial u_i}{\partial r_k}dr_i dr_k + \frac{\partial u_i}{\partial r_k}\frac{\partial u_i}{\partial r_l}dr_k dr_l, \tag{2.7}$$

where $i, k, l = x, y, z$.

Expressing the first term of Eq. (2.7) in the symmetrical form $(\frac{\partial u_i}{\partial r_k} + \frac{\partial u_k}{\partial r_i})dr_i dr_k$ and interchanging the dummy indices i and l in the second term gives

$$\begin{aligned} d\boldsymbol{u}^2 &= \frac{\partial u_i}{\partial r_k} dr_i dr_k + \frac{\partial u_k}{\partial r_i} dr_i dr_k + \frac{\partial u_l}{\partial r_k}\frac{\partial u_l}{\partial r_i} dr_i dr_k \\ &= 2\mu_{ik} dr_i dr_k, \end{aligned} \tag{2.8}$$

where

$$\mu_{ik} = \frac{1}{2}\left(\frac{\partial u_i}{\partial r_k} + \frac{\partial u_k}{\partial r_i} + \frac{\partial u_l}{\partial r_k}\frac{\partial u_l}{\partial r_i}\right). \tag{2.9}$$

The matrix elements μ_{ik} are components of the strain tensor $\boldsymbol{\mu}$. This tensor is symmetrical, its components describe a deformation in terms of particle displacement and it reduces to zero for all rigid motions. Also, except for special cases like deformations of thin rods, thin plates and cylindrical surfaces [99] or for materials like rubber, the displacement gradient has to be kept below the range of 10^{-3} to avoid permanent deformation or fracture of the material [101]. In such a case the non-linear terms in Eq. (2.8) are negligible and the strain-displacement relation takes the form

$$\mu_{ik} = \frac{1}{2}\left(\frac{\partial u_i}{\partial r_k} + \frac{\partial u_k}{\partial r_i}\right). \tag{2.10}$$

The strain tensor $\boldsymbol{\mu}$ obtained according to (2.10) can be presented in a simplified form using a system of abbreviated subscripts so that $ik \mapsto I$, following the cyclic pattern through the diagonal ($xx \mapsto 1$, $yy \mapsto 2$, $zz \mapsto 3$) and then back along the off-diagonal elements ($yz \mapsto 4$, $xz \mapsto 5$, $xy \mapsto 6$). This abbreviated notation allows the strain tensor to be written as a 6×1 vector. The transformation occurs according

to the following

$$\boldsymbol{\mu} = \begin{bmatrix} \mu_{xx} & \mu_{xy} & \mu_{xz} \\ \mu_{xy} & \mu_{yy} & \mu_{yz} \\ \mu_{xz} & \mu_{yz} & \mu_{zz} \end{bmatrix} \longmapsto \begin{bmatrix} \mu_1 \\ \mu_2 \\ \mu_3 \\ \mu_4 \\ \mu_5 \\ \mu_6 \end{bmatrix}. \tag{2.11}$$

In this notation the components μ_I of $\boldsymbol{\mu}$ can be written as

$$\mu_I = \nabla_{Ij} u_j \tag{2.12}$$

where ∇_{Ij} is a symmetric gradient operator defined as

$$\nabla_{Ij} = \begin{bmatrix} \frac{\partial}{\partial r_x} & 0 & 0 \\ 0 & \frac{\partial}{\partial r_y} & 0 \\ 0 & 0 & \frac{\partial}{\partial r_z} \\ 0 & \frac{\partial}{\partial r_z} & \frac{\partial}{\partial r_y} \\ \frac{\partial}{\partial r_z} & 0 & \frac{\partial}{\partial r_x} \\ \frac{\partial}{\partial r_y} & \frac{\partial}{\partial r_x} & 0 \end{bmatrix}, \tag{2.13}$$

with $I = 1, 2, 3, 4, 5, 6$ and $j = x, y, z$.

A continuous medium can be defined in a coordinate system as a group of infinitesimal volume elements dV with surface dS. When a body is deformed and its deformation is characterized by displacement $\boldsymbol{u}(\boldsymbol{r}, t)$ and the strain $\boldsymbol{\mu}(\boldsymbol{r}, t)$, internal elastic forces that tend to return it to the original state of equilibrium arise. If

the source of deformation is external, one must also consider two additional types of forces, body forces and surface forces. Body forces $\boldsymbol{F}(\boldsymbol{r},t)$ are long-range forces acting directly upon the elements of volume $dV = dxdydz$ in the body. They can be produced by gravitational or, in some cases, by electric and magnetic fields [101] and are proportional to the volume dV. Body forces are sometimes accompanied by body torques, $\boldsymbol{G}(\boldsymbol{r},t)$, however these are neglected in linearized vibration theory. The surface dS of the volume element dV can be subjected to surface (traction) forces $\boldsymbol{T}(\boldsymbol{r},t)$. These surface forces applied on the boundary of the material do not act directly on the volume elements dV but the perturbation caused by them is transmitted by elastic forces (stresses) between volume elements [102]. In a vibrating element of arbitrary shape, with volume dV and an arbitrarily oriented surface dS with normal $\hat{\boldsymbol{n}}$, the components of the traction force per unit area acting on this surface $T_{i\boldsymbol{n}}$ can be written in the form

$$T_{i\boldsymbol{n}} = \sigma_{ij}\, n_j. \tag{2.14}$$

where σ_{ij} are the stress components.

The component of integrated surface force acting on the particle is then $\int_{\delta S} \sigma_{ij} n_j dS$ and the body force is $\int_{\delta V} F_i dV$. According to Newton's second law [103] the equation of motion of the particle in the i^{th} direction is

$$\int_{\delta S} \sigma_{ij}\, n_j\, dS + \int_{\delta V} F_i\, dV = \int_{\delta V} \rho\, \frac{\partial^2 u_i}{\partial t^2}\, dV. \tag{2.15}$$

Using the Gauss divergence theorem [104] one can transform Eq. (2.15) into

$$\int_{\delta V} \frac{\partial \sigma_{ij}}{\partial r_j}\, dV + \int_{\delta V} F_i\, dV = \int_{\delta V} \rho\, \frac{\partial^2 u_i}{\partial t^2}\, dV. \tag{2.16}$$

With sufficiently small δV the values of the volume integrals are constant and Eq. (2.16) can be transformed into

$$\frac{\partial \sigma_{ij}}{\partial r_j} + F_i = \rho\, \frac{\partial^2 u_i}{\partial t^2}, \tag{2.17}$$

which is the translational equation of motion for a vibrating medium. The solutions to this equation are elastic waves propagating in the material [105]:

$$\boldsymbol{u}(\boldsymbol{r}, t) = \boldsymbol{u}_{ij} exp[\mathrm{i}(\boldsymbol{r} \cdot \boldsymbol{q} - \nu t)]. \tag{2.18}$$

As the stress matrix $\boldsymbol{\sigma}$ is symmetric it can be expressed using an abbreviated notation. The mapping procedure is identical to the one described for the strain tensor and therefore the 3×3 stress tensor can be expressed as a six element column matrix

$$\boldsymbol{\sigma} = \begin{bmatrix} \sigma_{xx} & \sigma_{xy} & \sigma_{xz} \\ \sigma_{xy} & \sigma_{yy} & \sigma_{yz} \\ \sigma_{xz} & \sigma_{yz} & \sigma_{zz} \end{bmatrix} \longmapsto \begin{bmatrix} \sigma_1 \\ \sigma_2 \\ \sigma_3 \\ \sigma_4 \\ \sigma_5 \\ \sigma_6 \end{bmatrix}. \tag{2.19}$$

The translational equation of motion can be written in abbreviated subscript notation as

$$\nabla_{iJ} \sigma_J + F_i = \rho\, \frac{\partial^2 u_i}{\partial t^2}, \tag{2.20}$$

where $i = x, y, z$, $J = 1, 2, 3, 4, 5, 6$, and ∇_{iJ} is called the divergence of the stress tensor and its matrix representation is:

$$\nabla_{iJ} = \begin{bmatrix} \frac{\partial}{\partial r_x} & 0 & 0 & 0 & \frac{\partial}{\partial r_z} & \frac{\partial}{\partial r_y} \\ 0 & \frac{\partial}{\partial r_y} & 0 & \frac{\partial}{\partial r_z} & 0 & \frac{\partial}{\partial r_x} \\ 0 & 0 & \frac{\partial}{\partial r_z} & \frac{\partial}{\partial r_y} & \frac{\partial}{\partial r_x} & 0 \end{bmatrix}. \tag{2.21}$$

According to Hooke's law, for sufficiently small deformations, the displacement is proportional to the strain and therefore the components of the stresses are linear functions of the strains and vice versa [106]. In the general case of a lossless medium the ideal Hooke's law relation is

$$\sigma_{ij} = c_{ijkl}\, \mu_{kl}, \tag{2.22}$$

where σ_{ij} are the components of stress tensor, μ_{kl} are the components of the strain tensor, $i, j, k, l = x, y, z$ and the c_{ijkl} are called elastic stiffness constants.

In general there are 81 elastic constants (as (2.22) contains nine equations for σ_{ij} and each equation has nine strain variables μ_{kl}) but they are not all independent. Since the stress and strain tensors are symmetric ($\sigma_{ij} = \sigma_{ji}$ and $\mu_{kl} = \mu_{lk}$), $c_{ijkl} = c_{jikl} = c_{ijlk} = c_{jilk}$. This reduces the number of elastic constants to 36. Additionally, the elastic energy U_S (strain energy) is a function of strain [107] according to the equation

$$\frac{\partial U_S}{\partial \mu_{ij}} = c_{ijkl}\mu_{kl}. \tag{2.23}$$

Because U_S is dependent only on the strain, the second partial derivative of the energy will be independent of the order of differentiation

$$\frac{\partial^2 U_S}{\partial \mu_{ij} \partial \mu_{kl}} = \frac{\partial^2 U_S}{\partial \mu_{kl} \partial \mu_{ij}}, \tag{2.24}$$

and therefore $c_{ijkl} = c_{klij}$, reducing the maximum number of independent elastic constants to 21 for a general medium. Hooke's law (2.22) can then be written using the abbreviated notation as

$$\sigma_I = c_{IJ}\, \mu_J, \tag{2.25}$$

where $I, J = 1, 2, 3, 4, 5, 6$ and c_{IJ} are components of a 6×6 symmetric tensor that given by

$$\boldsymbol{c} = \begin{bmatrix} c_{11} & c_{12} & c_{13} & c_{14} & c_{15} & c_{16} \\ c_{12} & c_{22} & c_{23} & c_{24} & c_{25} & c_{26} \\ c_{13} & c_{23} & c_{33} & c_{34} & c_{35} & c_{36} \\ c_{14} & c_{24} & c_{34} & c_{44} & c_{45} & c_{46} \\ c_{15} & c_{25} & c_{35} & c_{45} & c_{55} & c_{56} \\ c_{16} & c_{26} & c_{36} & c_{46} & c_{56} & c_{66} \end{bmatrix}. \tag{2.26}$$

The symmetry of the material can further reduce the number of elastic constants [108]. The p-Si single layer films analyzed in this work are of cubic symmetry with three equivalent directions $x = y = z$. Materials of such symmetry can be elastically characterized by three independent elastic constants (c_{11}, c_{12}, c_{44}) and an elastic

tensor of the form [101]

$$\boldsymbol{c} = \begin{bmatrix} c_{11} & c_{12} & c_{12} & 0 & 0 & 0 \\ c_{12} & c_{11} & c_{12} & 0 & 0 & 0 \\ c_{12} & c_{12} & c_{11} & 0 & 0 & 0 \\ 0 & 0 & 0 & c_{44} & 0 & 0 \\ 0 & 0 & 0 & 0 & c_{44} & 0 \\ 0 & 0 & 0 & 0 & 0 & c_{44} \end{bmatrix}. \tag{2.27}$$

The investigated p-Si superlattices are characterized by tetragonal symmetry ($x = y \neq z$) with five independent elastic constants (c_{11}, c_{12}, c_{13}, c_{33}, c_{44}) and an elastic constants tensor of the form [101]

$$\boldsymbol{c} = \begin{bmatrix} c_{11} & c_{12} & c_{13} & 0 & 0 & 0 \\ c_{12} & c_{11} & c_{13} & 0 & 0 & 0 \\ c_{13} & c_{13} & c_{33} & 0 & 0 & 0 \\ 0 & 0 & 0 & c_{44} & 0 & 0 \\ 0 & 0 & 0 & 0 & c_{44} & 0 \\ 0 & 0 & 0 & 0 & 0 & c_{66} \end{bmatrix}. \tag{2.28}$$

When all three crystal axes are equivalent the pairs c_{12} and c_{13}, c_{11} and c_{33} and c_{44} and c_{66} become indistinguishable and the tensor given by Eq. (2.28) reduces to that of a cubic system given by Eq. (2.27). The most symmetric (isotropic) media

need only two independent elastic constants to be fully characterized elastically.

Differentiating the lossless version of Hooke's law, (2.22) or (2.25), with respect to time leads to (equations in the square brackets show the abbreviated subscript notation)

$$\frac{\partial \sigma_{ij}}{\partial t} = c_{ijkl} \frac{\partial \mu_{kl}}{\partial t} \qquad \left[\frac{\partial \sigma_K}{\partial t} = c_{KL} \frac{\partial \mu_L}{\partial t} \right]. \tag{2.29}$$

For the above and all of the following expressions, subscripts $i, j, k, l = x, y, z$ and $I, J, K, L = 1, 2, 3, 4, 5, 6$. Substituting μ_{kl} from (2.10) (or μ_L from Eq. (2.12)) transforms Eq. (2.29) to

$$\frac{\partial \sigma_{ij}}{\partial t} = c_{ijkl} \frac{1}{2} \frac{\partial}{\partial t} \left(\frac{\partial u_k}{\partial r_l} + \frac{\partial u_l}{\partial r_k} \right) \qquad \left[\frac{\partial \sigma_K}{\partial t} = c_{KL} \frac{\partial}{\partial t} \nabla_{Lk} u_k \right]. \tag{2.30}$$

As the time and spatial derivatives are independent, one can interchange the order of differentiation and obtain

$$\frac{\partial \sigma_{ij}}{\partial t} = c_{ijkl} \frac{1}{2} \left(\frac{\partial v_k}{\partial r_l} + \frac{\partial v_l}{\partial r_k} \right) \qquad \left[\frac{\partial \sigma_K}{\partial t} = c_{KL} \nabla_{Lk} v_k \right], \tag{2.31}$$

where

$$v_i = \frac{\partial u_i}{\partial t} \tag{2.32}$$

is a component of the velocity of the particle. Differentiating the translational equation of motion (2.17) with respect to time t, using the relationship between particle velocity v_i and its displacement u_i, and taking advantage of the independence of time and spatial derivatives, one obtains

$$\frac{\partial}{\partial r_j} \left(\frac{\partial \sigma_{ij}}{\partial t} \right) + \frac{\partial F_i}{\partial t} = \rho \frac{\partial^2 v_i}{\partial t^2} \qquad \left[\nabla_{jK} \left(\frac{\partial \sigma_K}{\partial t} \right) + \frac{\partial F_i}{\partial t} = \rho \frac{\partial^2 v_i}{\partial t^2} \right]. \tag{2.33}$$

Eliminating $\frac{\partial \sigma_{ij}}{\partial t}$ from Eq. (2.33) by substituting Eq. (2.31) transforms the former equation into a wave equation

$$\frac{\partial}{\partial r_j}\left(c_{ijkl}\,\frac{1}{2}\left(\frac{\partial v_k}{\partial r_l}+\frac{\partial v_l}{\partial r_k}\right)\right)+\frac{\partial F_i}{\partial t}=\rho\,\frac{\partial^2 v_i}{\partial t^2} \tag{2.34}$$

or, in the abbreviated subscript notation

$$\nabla_{iK}c_{KL}\nabla_{Kj}v_j=\rho\frac{\partial^2 v_i}{\partial t^2}-\frac{\partial F_i}{\partial t}. \tag{2.35}$$

If the considered region does not include sources (F_i=0) a uniform plane wave propagating along an arbitrary direction $\hat{\boldsymbol{l}}=\hat{\boldsymbol{i}}l_i$, where l_i are direction cosines as shown in Fig. 2.2 and $i=x,y,z$, has field proportional to $\exp[\mathrm{i}(\omega t-k\hat{\boldsymbol{l}}\cdot\boldsymbol{r})]$, where ω is the angular frequency of the wave and k is the magnitude of its wavevector. The operators ∇_{iK} and ∇_{Kj} acting on the velocity v_j can be replaced by matrices $-\mathrm{i}kl_{iK}$ and $-\mathrm{i}kl_{Kj}$ respectively, where

$$-\mathrm{i}kl_{iK}=-\mathrm{i}k\begin{bmatrix} l_x & 0 & 0 & 0 & l_z & l_y \\ 0 & l_y & 0 & l_z & 0 & l_x \\ 0 & 0 & l_z & l_y & l_x & 0 \end{bmatrix} \tag{2.36}$$

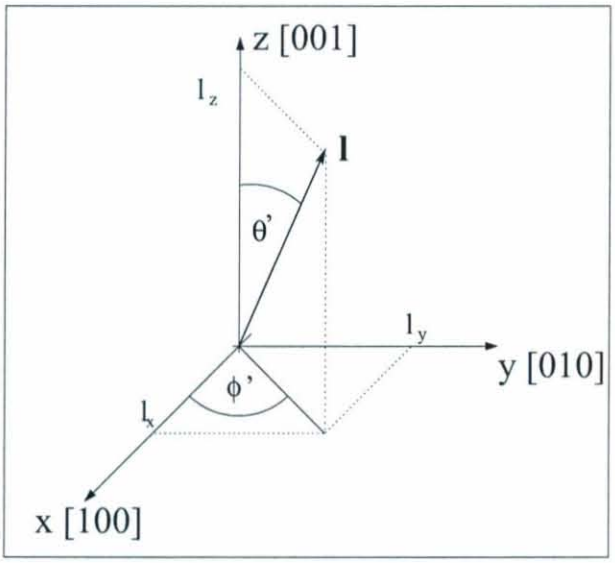

Figure 2.2: Directional cosines of an arbitrary direction $\hat{l}$.

and

$$-\mathrm{i}kl_{Kj} = -\mathrm{i}k \begin{bmatrix} l_x & 0 & 0 \\ 0 & l_y & 0 \\ 0 & 0 & l_z \\ 0 & l_z & l_y \\ l_z & 0 & l_x \\ l_y & l_x & 0 \end{bmatrix}. \tag{2.37}$$

The wave equation (2.35) with $F_i = 0$ then reduces to

$$k^2 \left(l_{iK} c_{KL} l_{Lj}\right) v_j = \rho\omega^2 v_i. \tag{2.38}$$

Equation (2.38) is called the Christoffel equation. It applies to plane waves propagating in media of any symmetry. The expression $l_{iK} c_{KL} l_{Lj}$ is the 3×3 symmetric

Kelvin-Christoffel matrix [109] and is denoted by Γ_{ij}. The elements of Γ_{ij} are functions only of the direction of wave propagation $\hat{l}$ and the elastic stiffness constants of the medium c_{IJ}. Since $\omega = kv$ where v is the phase velocity of the wave, the Christoffel equation can be rewritten as

$$\Gamma_{ij} v_j = \rho v^2 v_i. \tag{2.39}$$

The values ρv^2 are the eigenvalues of this equation and they satisfy the secular equation [104]

$$|\Gamma_{ij} - \rho v^2 \delta_{ij}| = 0 \tag{2.40}$$

where δ_{ij} is Kronecker's delta.

In the case of a cubic material with elastic constants tensor given by Eq. (2.27), Eq. (2.40) for a phonon propagating in an arbitrary direction $\hat{l}$ has the form

$$\begin{vmatrix} c_{11}l_x^2+c_{44}(l_y^2+l_z^2)-\rho v^2 & (c_{12}+c_{44})l_x l_y & (c_{12}+c_{44})l_x l_z \\ (c_{12}+c_{44})l_x l_y & c_{11}l_y^2+c_{44}(l_x^2+l_z^2)-\rho v^2 & (c_{12}+c_{44})l_y l_z \\ (c_{12}+c_{44})l_x l_z & (c_{12}+c_{44})l_y l_z & c_{44}(l_x^2+l_y^2)+c_{11}l_z^2-\rho v^2 \end{vmatrix} = 0. \tag{2.41}$$

In a cubic system, where x, y and z axes are equivalent, Eq. (2.41) factors identically for a phonon propagating in any of the planes including a cube face into one linear term and one quadratic term. In the case where the phonon is propagating in

a (010) plane with l_y=0, the two uncoupled dispersion relations are

$$c_{44}(l_x^2+l_z^2)-\rho v^2=0 \tag{2.42a}$$

$$(c_{11}l_x^2+c_{44}l_z^2-\rho v^2)(c_{44}l_x^2+c_{11}l_z^2-\rho v^2)-(c_{12}+c_{44})^2l_x^2l_z^2=0. \tag{2.42b}$$

With the angle between the propagation direction $\hat{\boldsymbol{l}}$ measured from the z axis in the way shown in Fig. 2.2 so that $l_x = \sin\theta'$ and $l_z = \cos\theta'$ and using the trigonometric identities $2\cos\phi\sin\phi = \sin(2\phi)$ and $\cos^2\phi+\sin^2\phi = 1$, the expressions for the velocities of elastic waves propagating along the $\hat{\boldsymbol{l}}$ direction may be calculated. From (2.42a), the velocity of the pure shear wave is [101]

$$v_T = \sqrt{\frac{c_{44}}{\rho}}. \tag{2.43}$$

Similarly from Eq. (2.42b), the velocity of the quasi-shear (the direction of the displacement of the particles is mostly perpendicular to the direction of propagation) wave for a phonon propagating in the (010) plane is

$$v_- = \frac{1}{\sqrt{2\rho}}\left(c_{11}+c_{44}-\sqrt{(c_{11}-c_{44})^2\cos^2(2\theta')+(c_{12}+c_{44})^2\sin^2(2\theta')}\right)^{1/2} \tag{2.44}$$

and the quasi-longitudinal (the direction of the displacement of the particles is mostly parellel to the direction of propagation) wave velocity is given by

$$v_+ = \frac{1}{\sqrt{2\rho}}\left(c_{11}+c_{44}+\sqrt{(c_{11}-c_{44})^2\cos^2(2\theta')+(c_{12}+c_{44})^2\sin^2(2\theta')}\right)^{1/2}. \tag{2.45}$$

The anisotropy ratio α, a measure of the magnitude of the elastic anisotropy of a cubic material, is calculated using

$$\alpha = \frac{2c_{44}}{c_{11}-c_{12}} \tag{2.46}$$

For an isotropic material the characteristic equation (Eq. (2.40)) and the dispersion relations are described with the same equations as for cubic symmetry, (Eq. (2.41) and (2.42)). In this case the elastic constants are, however, related through the relation [110]

$$c_{11} = c_{12} + 2\, c_{44} \tag{2.47}$$

and hence the anisotropy ratio given by Eq. (2.46) is equal to unity and the velocities given by Eqs (2.43)-(2.45) simplify to

$$v_T = \sqrt{\frac{c_{44}}{\rho}} \tag{2.48}$$

and

$$v_L = \sqrt{\frac{c_{11}}{\rho}}. \tag{2.49}$$

In the case of the tetragonal symmetry with an elastic constants tensor as shown in Eq. (2.28), Eq. (2.40) for a phonon propagating along an arbitrary direction $\hat{l}$ is of the form

$$\begin{vmatrix} c_{11}l_x^2+c_{66}l_y^2+c_{44}l_z^2-\rho v^2 & (c_{12}+c_{66})l_xl_y & (c_{13}+c_{44})l_xl_z \\ (c_{12}+c_{66})l_xl_y & c_{66}l_x^2+c_{22}l_y^2+c_{44}l_z^2-\rho v^2 & (c_{13}+c_{44})l_yl_z \\ (c_{13}+c_{44})l_xl_z & (c_{13}+c_{44})l_yl_z & c_{44}l_x^2+c_{44}l_y^2+c_{33}l_z^2-\rho v^2 \end{vmatrix} = 0. \tag{2.50}$$

For a phonon propagating in the (010) plane Eq. (2.50) results in the following two

uncoupled relations

$$c_{66}l_x^2+c_{44}l_z^2-\rho v^2=0 \tag{2.51a}$$

$$(c_{11}l_x^2+c_{44}l_z^2-\rho v^2)(c_{44}l_x^2+c_{33}l_z^2-\rho v^2)-((c_{13}+c_{44})l_xl_z)^2=0. \tag{2.51b}$$

With the direction of propagation defined as above, Eqs. (2.51) have three solutions. There is a pure shear wave with velocity obtained from Eq. (2.51a)

$$v_T=\sqrt{\frac{c_{66}\sin^2\theta'+c_{44}\cos^2\theta'}{\rho}} \tag{2.52}$$

and quasi-shear and quasi-longitudinal waves with velocities obtained from Eq. (2.51b) and given by

$$\begin{aligned} v_-=&\frac{1}{\sqrt{2\rho}}\Bigg(c_{11}\sin^2\theta'+c_{33}\cos^2\theta'+c_{44} \\ &-\sqrt{((c_{11}-c_{44})\sin^2\theta'+(c_{44}-c_{33})\cos^2\theta')^2+(c_{13}+c_{44})^2\sin^2(2\theta')}\Bigg)^{1/2} \end{aligned} \tag{2.53}$$

and

$$\begin{aligned} v_+=&\frac{1}{\sqrt{2\rho}}\Bigg(c_{11}\sin^2\theta'+c_{33}\cos^2\theta'+c_{44} \\ &+\sqrt{((c_{11}-c_{44})\sin^2\theta'+(c_{44}-c_{33})\cos^2\theta')^2+(c_{13}+c_{44})^2\sin^2(2\theta')}\Bigg)^{1/2} \end{aligned} \tag{2.54}$$

respectively.

2.2 Effective Elastic Constants of Multilayered Media

The most general formalism that enables numerical evaluation of the effective elastic constants of a superlattice made of two layers of arbitrary symmetry was

presented by Grimsditch and Nizzoli [84] and it is this model that is applied in this work. This model builds upon earlier work on the electromagnetic properties of layered media by Rytov [111] as well as the elastic properties of materials made of alternating two isotropic layers done by Backus [112] and Behrens [113], [114]. In what follows, the components of stress, strain and the elastic constants tensor of constituent layer ζ are labeled $\sigma_{ij}^{[\zeta]}$, $\mu_{ij}^{[\zeta]}$ and $c_{ij}^{[\zeta]}$, respectively, whereas σ_{ij}, μ_{ij} and c_{ij} refer to the stress, strain and effective elastic constant of the superlattice [115]. The thicknesses of the constituent layers are $d^{[\zeta]}$ and the thickness fraction of each material, $f^{[\zeta]}$ is defined as

$$f^{[\zeta]} = \frac{d^{[\zeta]}}{d^{[1]} + d^{[2]}}. \tag{2.55}$$

Each effective elastic constant c_{ij} can be expressed as a function of the elastic constants of the constituent layers $c_{ij}^{[\zeta]}$ and the thickness fractions $f^{[\zeta]}$.

The stress and strain of the superlattice can be expressed as a function of the stress and strain of the individual layers:

$$\boldsymbol{\sigma} = f^{[1]}\boldsymbol{\sigma}^{[1]} + f^{[2]}\boldsymbol{\sigma}^{[2]}, \tag{2.56a}$$

$$\boldsymbol{\mu} = f^{[1]}\boldsymbol{\mu}^{[1]} + f^{[2]}\boldsymbol{\mu}^{[2]}, \tag{2.56b}$$

where $\boldsymbol{\sigma}$, $\boldsymbol{\sigma}^{[\zeta]}$, $\boldsymbol{\mu}$ and $\boldsymbol{\mu}^{[\zeta]}$ are 6×1 matrices as the two index notation is being used. The stress-strain relations are defined by Eq. (2.25) which for each of the constituent

layers and for the superlattice take the form

$$\boldsymbol{\sigma}^{[\zeta]} = \boldsymbol{c}^{[\zeta]}\boldsymbol{\mu}^{[\zeta]}, \quad \zeta = 1, 2 \tag{2.57a}$$

$$\boldsymbol{\sigma} = \boldsymbol{c}\boldsymbol{\mu}, \tag{2.57b}$$

with $\boldsymbol{c}$ and $\boldsymbol{c}^{[\zeta]}$ are 6×6 matrices. Substituting Eqs. (2.56a) and (2.56b) into Eq. (2.57b) one gets

$$f^{[1]}\boldsymbol{\sigma}^{[1]} + f^{[2]}\boldsymbol{\sigma}^{[2]} = \boldsymbol{c}(f^{[1]}\boldsymbol{\mu}^{[1]} + f^{[2]}\boldsymbol{\mu}^{[2]}). \tag{2.58}$$

Substituting Eq. (2.57a) into Eq. (2.58) leads to:

$$f^{[1]}(\boldsymbol{c}^{[1]} - \boldsymbol{c})\boldsymbol{\mu}^{[1]} + f^{[2]}(\boldsymbol{c}^{[2]} - \boldsymbol{c})\boldsymbol{\mu}^{[2]} = 0 \tag{2.59}$$

To solve Eq. (2.59) the relationship between the strain tensors $\boldsymbol{\mu}^{[1]}$ and $\boldsymbol{\mu}^{[2]}$ must be known. In order to obtain this relationship the boundary conditions for strains and stresses on the layer interfaces are taken into consideration. In an orthogonal coordinate system the superlattice is assumed to have the z axis normal to the layers and x and y axes lying in plane of the layers (see Fig. 2.3). At the interfaces between layers the components of stress acting on the plane perpendicular to z axis have to fulfill the continuity condition:

$$\sigma_{iz}^{[1]} = \sigma_{iz}^{[2]} \quad i = x, y, z \tag{2.60}$$

and the components of the strain in the same plane have to obey:

$$\mu_{ij}^{[1]} = \mu_{ij}^{[2]} \quad i, j \neq z. \tag{2.61}$$

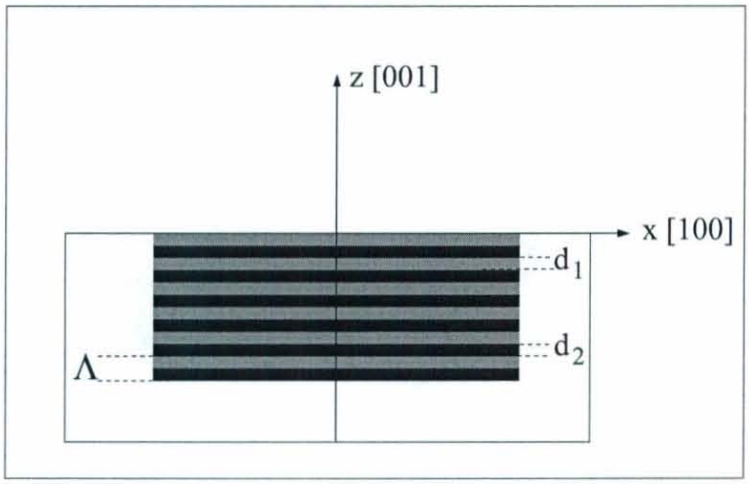

Figure 2.3: Cross section of a porous silicon multilayered film through the XZ plane. Λ - modulation wavelength (period) of the superlattice, $d^{[1]}$, $d^{[2]}$ - thicknesses of the constituent layers.

The latter equation, Eq. (2.61), can be written as

$$\boldsymbol{\mu}^{[1]} = \boldsymbol{M}\boldsymbol{\mu}^{[2]} \tag{2.62}$$

where $\boldsymbol{M}$ is a transformation matrix between the strain tensors of two layers. $\boldsymbol{M}$ can be evaluated numerically if the components of the elastic tensor of the constituent layers $c_{IJ}^{[\zeta]}$ are known. Combining Eqs. (2.59) and (2.62) results in

$$[f^{[1]}(\boldsymbol{c}^{[1]} - \boldsymbol{c})\boldsymbol{M} + f^{[2]}(\boldsymbol{c}^{[2]} - \boldsymbol{c})]\boldsymbol{\mu}^{[2]} = 0. \tag{2.63}$$

Eq. (2.63) must hold true for an arbitrary strain $\boldsymbol{\mu}^{[2]}$, therefore it is true that

$$f^{[1]}\boldsymbol{c}^{[1]}\boldsymbol{M} + f^{[2]}\boldsymbol{c}^{[2]} = f^{[1]}\boldsymbol{c}\boldsymbol{M} + f^{[2]}\boldsymbol{c}. \tag{2.64}$$

Solving Eq. (2.64) for elastic constants tensor $\boldsymbol{c}$ leads to

$$\boldsymbol{c} = (f^{[1]}\boldsymbol{c}^{[1]}\boldsymbol{M} + f^{[2]}\boldsymbol{c}^{[2]})(f^{[1]}\boldsymbol{M} + f^{[2]}\boldsymbol{I})^{-1}, \tag{2.65}$$

where $\boldsymbol{I}$ is the 6×6 identity matrix. Eq. (2.65) allows calculation of the components of the elastic tensor at least numerically. It is noted that for the case of isotropic constituent layers the expressions for the effective elastic constants given by the presented model are identical with those derived by Behrens [113].

In the case of p-Si multilayered films the constituent layers keep the cubic symmetry of the c-Si parent wafer [116]. As can be seen in Sec. 2.1, crystals of cubic symmetry have three independent elastic constants, c_{11}, c_{12} and c_{44}, and the elastic tensor of the each individual layer is presented by matrix (2.27) [101]. Fitting the velocities of the quasi-longitudinal and quasi-transverse phonons of single p-Si layers as a function of the angle from the z-axis to Eqs. (2.44) and (2.45) allows the values of c_{IJ} to be determined. Using the procedure described by Grimsditch and Nizzoli one can obtain the effective elastic constants for a system consisting of two alternating thin layers of cubic symmetry and different elastic properties repeating through a thickness of a few microns [82]. The elastic tensor of this multilayered film, $\boldsymbol{c}$, turns out to have six independent elastic constants c_{11}, c_{12}, c_{13}, c_{33}, c_{44} and c_{66} and is of the form [101]:

$$\boldsymbol{c} = \begin{bmatrix} c_{11} & c_{12} & c_{13} & 0 & 0 & 0 \\ c_{12} & c_{11} & c_{13} & 0 & 0 & 0 \\ c_{13} & c_{13} & c_{33} & 0 & 0 & 0 \\ 0 & 0 & 0 & c_{44} & 0 & 0 \\ 0 & 0 & 0 & 0 & c_{44} & 0 \\ 0 & 0 & 0 & 0 & 0 & c_{66} \end{bmatrix}, \tag{2.66}$$

which means that in this case the superlattice is elastically equivalent to a tetragonal crystal (see Eq. (2.28)) with elastic constants of the following forms (see Appendix B)

$$c_{11} = -\frac{f^{[1]}\frac{c_{12}^{[2]}-c_{12}^{[1]}}{c_{11}^{[1]}}(c_{11}^{[2]}f^{[1]}+c_{11}^{[2]}f^{[2]})}{(f^{[1]}+f^{[2]})(\frac{c_{11}^{[2]}f^{[1]}}{c_{11}^{[1]}}+f^{[2]})} + \frac{f^{[1]}(c_{12}^{[1]}+c_{11}^{[1]}(-\frac{c_{12}^{[1]}}{c_{11}^{[1]}}+\frac{c_{12}^{[2]}}{c_{11}^{[1]}})+c_{11}^{[2]}f^{[2]}}{f^{[1]}+f^{[2]}}, \tag{2.67a}$$

$$c_{12} = -\frac{f^{[1]}\frac{c_{12}^{[2]}-c_{12}^{[1]}}{c_{11}^{[1]}}(c_{11}^{[2]}f^{[1]}+c_{11}^{[2]}f^{[2]})}{(f^{[1]}+f^{[2]})(\frac{c_{11}^{[2]}f^{[1]}}{c_{11}^{[1]}}+f^{[2]})} + \frac{f^{[1]}(c_{12}^{[1]}+c_{12}^{[1]}(-\frac{c_{12}^{[1]}}{c_{11}^{[1]}}+\frac{c_{12}^{[2]}}{c_{11}^{[1]}})+c_{12}^{[2]}f^{[2]}}{f^{[1]}+f^{[2]}}, \tag{2.67b}$$

$$c_{13} = \frac{\frac{c_{12}^{[1]}c_{11}^{[2]}f^{[1]}}{c_{11}^{[1]}}+c_{12}^{[2]}f^{[2]}}{\frac{c_{11}^{[2]}f^{[1]}}{c_{11}^{[1]}}+f^{[2]}} \tag{2.67c}$$

$$c_{33} = \frac{c_{11}^{[2]}f^{[1]}+c_{11}^{[2]}f^{[2]}}{\frac{c_{11}^{[2]}f^{[1]}}{c_{11}^{[1]}}+f^{[2]}}, \tag{2.67d}$$

$$c_{44} = \frac{c_{44}^{[2]} f^{[1]} + c_{44}^{[2]} f^{[2]}}{\frac{c_{44}^{[2]} f^{[1]}}{c_{44}^{[1]}} + f^{[2]}}, \tag{2.67e}$$

$$c_{66} = \frac{c_{44}^{[1]} f^{[1]} + c_{44}^{[2]} f^{[2]}}{f^{[1]} + f^{[2]}}. \tag{2.67f}$$

2.3 Brillouin Light Scattering

The scattering of light can occur only by an inhomogeneous medium [117]. From the classical point of view, in a homogenous material the thermodynamic fluctuations either of thermal or strain character create local inhomogeneous regions which cause scattering. At finite temperatures atoms in solids are in constant motion described by the normal modes of the lattice. There are always three acoustic modes and a number of optic modes [15]. The three acoustic modes are equivalent to elastic (or sound) waves. In comparison to fluids the propagation of elastic waves in solids is practically undamped [118] and causes fluctuations in the strain of the material, which leads, through the photoelastic effect, to fluctuations in local dielectric constant [119]. The interaction between light and thermally excited acoustic excitations in solids was first investigated and described in by Brillouin [120]. Although historically confined to transparent media, since the introduction of the high-contrast spectrometer this technique has also been used to investigate opaque materials [121]. Brillouin light scattering is complementary to ultrasonic techniques for the study of elastic and photo-elastic properties of materials however, unlike ultrasonic techniques, in this case no external forces are applied to the material. The frequency regime probed lies

in the so-called hypersonic frequency regime (1 MHz to 100 GHz) and fills the region between ultrasonic and neutron scattering techniques [122].

Light waves can undergo inelastic scattering in a material due to interactions with acoustic waves conserving energy and momentum and giving rise to Brillouin scattering [123]. Because of the interference of the scattered waves only the elastic waves with a certain wave number, fulfilling the Bragg's law of reflection

$$2\lambda \sin\theta = m\lambda_i \tag{2.68}$$

where $m = 1, 2, .. ,$ λ is the wavelength of the acoustic wave, θ is the angle between the direction of incident and scattered light, and λ_i is a wavevector of incident light, contribute to the scattered light. What is more, the incident light upon reflection by the elastic waves of particular frequency ν experiences a $\pm\nu$ shift in frequency as a result of the Doppler effect [124].

From the quantum-mechanical point of view the process can be visualized as first-order scattering by acoustic phonons. The kinematics of the first order scattering process is shown in Fig. 2.4. In this case the conservation of energy and momentum during the scattering process are expressed according to

$$h\nu_i \pm h\nu = h\nu_s, \tag{2.69a}$$

$$h\boldsymbol{k}_i \pm h\boldsymbol{q} = h\boldsymbol{k}_s, \tag{2.69b}$$

where ν_i and ν_s are frequencies of incident and scattered light, respectively, ν is frequency of the acoustic phonon, $\boldsymbol{k}_i$ and $\boldsymbol{k}_s$ are the wavevectors of incident and

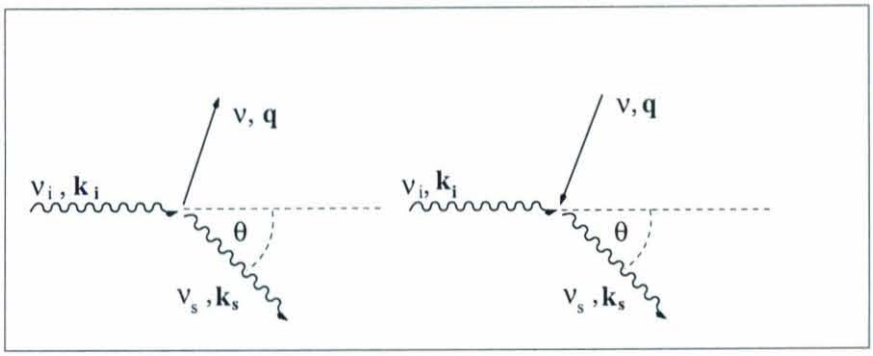

Figure 2.4: Quantum picture of kinematics of first-order scattering process. The Stokes process (creation) is shown on the left hand side while the anti-Stokes process (annihilation) is on the right. After [125].

scattered photon, respectively, and $\boldsymbol{q}$ is the wavevector of the acoustic phonon. The "+" sign indicates annihilation of a phonon and the "–" sign indicates a phonon creation.

From Eqs. (2.69) one can see that

$$\Delta\nu = \pm\nu = \nu_s - \nu_i, \tag{2.70}$$

and

$$\pm\boldsymbol{q} = \boldsymbol{k}_s - \boldsymbol{k}_i. \tag{2.71}$$

For each phonon wavevector $\boldsymbol{q}$, three possible phonon polarization vectors can be identified. For an arbitrary direction of propagation the polarization vectors depend on the components of elastic tensor $\boldsymbol{c}$ characteristic of the symmetry of the medium [126].

The schematics of Brillouin light scattering from a semi-infinite material is presented in Fig. 2.5. The vector Eq. (2.71) can be broken into components along the

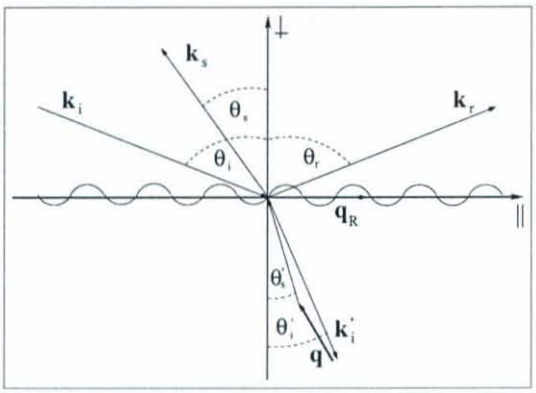

Figure 2.5: Schematic of the scattering geometry showing incident, reflected and scattered light wavevectors $\boldsymbol{k_i}$, $\boldsymbol{k_r}$ and $\boldsymbol{k_s}$, and the bulk and surface phonon vectors $\boldsymbol{q}$ and $\boldsymbol{q_R}$. After [127].

direction perpendicular to the surface of the material and along the direction parallel to the surface. The magnitudes of the perpendicular and parallel components of the phonon wavevector are

$$q_\perp = k_s' \cos\theta_i' + k_i' \cos\theta_s' \tag{2.72a}$$

$$q_\parallel = k_s' \sin\theta_i' + k_i' \sin\theta_s' \tag{2.72b}$$

where θ_i' and θ_s' are angles the incident and scattered light make inside the material with the normal to the surface. Squaring Eqs. (2.72a) and (2.72b) and adding the equations gives the expression for the square of the magnitude of the phonon wavevector:

$$\begin{aligned} q^2 = {} & k_i'^2 \sin^2\theta_i' + k_s'^2 \sin^2\theta_s' + k_i'^2 \cos^2\theta_i' + k_s'^2 \cos^2\theta_s' \\ & + 2k_i'k_s' \sin\theta_i' \sin\theta_s' + 2k_i'k_s' \cos\theta_i' \cos\theta_s', \end{aligned} \tag{2.73}$$

which can be simplified, using $\sin^2\phi + \cos^2\phi = 1$ and the expression for the cosine

of the difference of two angles [104], into

$$q^2 = k_i'^2 + k_s'^2 + 2k_i'k_s' \cos(\theta_s' - \theta_i'). \tag{2.74}$$

The angle between scattered and incident light wavevectors inside the material, $\theta = \theta_s' - \theta_i' + \pi$. Using this relation together with the identity $\cos(\pi+\phi) = -\cos\phi$, Eq. (2.74) can be transformed into

$$q = \sqrt{k_i'^2 + k_s'^2 - 2k_i'k_s' \cos(\theta)}. \tag{2.75}$$

Using the general relationship between the magnitude of the wavevector $k_{i,s}$, frequency $\nu_{i,s}$ and velocity c for the incident and scattered light [128]

$$k_{i,s} = \frac{2\pi\nu_{i,s}}{c}, \tag{2.76}$$

and for the phonon

$$q = \frac{2\pi\nu}{v}, \tag{2.77}$$

Eq. (2.75) becomes

$$q = \frac{2\pi\nu}{v} = \frac{2\pi}{c}\sqrt{\nu_i^2 n_i^2 + \nu_s^2 n_s^2 - 2\nu_i\nu_s n_i n_s \cos\theta}. \tag{2.78}$$

From Eq. (2.69a), as the frequency of the phonon ν is several orders of magnitude smaller than ν_i and ν_s, in the first approximation $\nu_i \approx \nu_s$ and in the case of a singly refracting medium, where $n_i = n_s = n$ Eq. (2.79) simplifies into

$$\frac{\nu}{v} = \frac{\nu_i n}{c}\sqrt{2 - 2\cos\theta}. \tag{2.79}$$

Using the trigonometric identity for sine of the half angle, $\sin\frac{\theta}{2} = \sqrt{\frac{1-\cos\theta}{2}}$ [104], Eq. (2.79) is transformed into

$$\frac{\nu}{v} = 2\frac{\nu_i n}{c}\sin\frac{\theta}{2}, \tag{2.80}$$

which, with substitution of $\lambda_i = \frac{c}{\nu_i}$ for the wavelength of the incident light, yields the velocity of an acoustic phonon propagating in the bulk material

$$v = \frac{\nu\lambda_i}{2n\sin\frac{\theta}{2}}, \tag{2.81}$$

with the phonon wavevector

$$q = 2nk_i\sin\frac{\theta}{2}. \tag{2.82}$$

In the case of BLS the magnitude and direction of the wavevector of the probed phonon depend on the scattering angle. The magnitude of q and hence the scattering angle are important since the energy of the phonons with $q \lesssim 1\ cm^{-1}$ depends almost linearly on the wavevector [129]. In these experiments a backscattering geometry with $\theta = 180^o$ was used. Eq. (2.81) then becomes

$$v_B = \frac{\nu_B\lambda_i}{2n}, \tag{2.83}$$

where v_B and ν_B are the velocity and frequency of a bulk phonon with particular polarization. In general, in crystalline materials three acoustic bulk phonons can be observed - one of longitudinal character (QL) and two of transverse character (QT) [130]. A simplified diagram of a typical Brillouin spectrum of intensity versus frequency shift is shown in Fig. 2.6. The tall central line due to elastically scattered

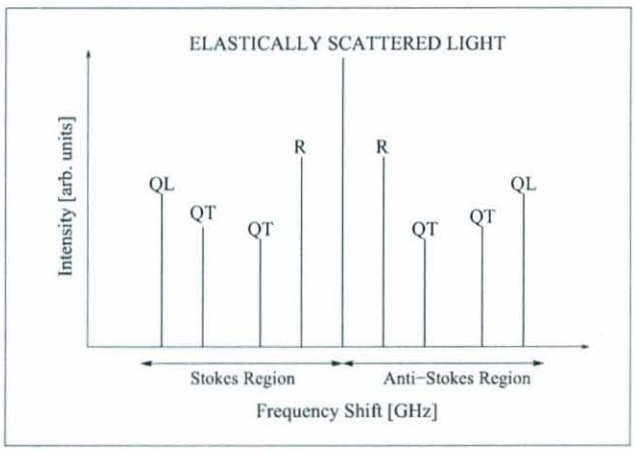

Figure 2.6: Schematic of a typical Brillouin light scattering spectrum. R - Rayleigh surface mode, QT - quasi-transverse modes, QL - quasi-longitudinal mode.

light is assigned zero frequency shift. The peaks due to surface Rayleigh (R), two quasi-transverse (QT) and quasi-longitudinal (QL) acoustic phonons are located symmetrically on both sides, depending on whether they were created (Stokes process) or annihilated (anti-Stokes process) during the scattering.

The coupling between incident light and thermally-excited acoustic excitations within the material is called the elasto-optic mechanism and is described by the Pöckels tensor [131]. Close to the surface the phonon vibrations cause the surface to a appear as moving grating, capable of changing the frequency of the incident light without any modulation of the dielectric constant in the bulk of the crystal (ripple mechanism). As the opacity and the refractive index of the medium increase the depth that light penetrates in the material becomes comparable to the light wavelength. The elasto-optic contribution to the scattering near surface decreases

and the contribution due to the ripple mechanism increases. The refractive index in opaque materials consists of both real and imaginary parts and can be written as $n = \eta + \imath\kappa$. The high optical absorption κ restricts the scattering volume in the direction perpendicular to the surface [121]. Those factors influence the Brillouin light scattering and require the theory derived above to be modified [124]. The momentum conservation Eq. (2.69b) is affected as the wavevector of the acoustic wave is no longer uniquely defined. All phonons with wavevectors within a range around the value q may contribute to scattering along the direction of $\boldsymbol{k}_s$ [132]. The expression for the frequency of the acoustic phonon remains the same as in case of transparent materials and, calculated from Eq. (2.80), is

$$\nu = \frac{2\eta v \sin\frac{\theta}{2}}{\lambda_i}. \tag{2.84}$$

with η being the real part of the refractive index. The width of the Brillouin peaks increases and has full width at half maximum (FWHM) of

$$\Delta\nu = \frac{4v\kappa}{\lambda_i}. \tag{2.85}$$

The line width of the Brillouin peak is a means to obtain the sound attenuation [133].

Apart from the surface deformation that appears due to impingement of bulk acoustic waves, the presence of the free boundary (surface) introduces new types of phonons called surface phonons that represent additional channels for scattering. The possibility of a wave traveling parallel to the surface of a semi-infinite medium such that the displacement of the atoms is confined to the boundary was considered by

Rayleigh [134]. The surface waves, also called Rayleigh waves, penetrate into the bulk over a distance comparable to the acoustic wavelength [122]. The amplitude of these waves decreases exponentially with the distance below the free surface and their velocity is slightly smaller than the velocity of the transverse bulk mode [135]. In the case of scattering from phonons propagating on the surface of the material the momentum conservation in the direction perpendicular to the surface breaks down and only the component parallel to the surface is conserved. In the case of backscattering and with $\nu_{i,s} \gg \nu$ Eq. (2.72b) becomes [136]

$$q_{\parallel} = 2k_i \sin\theta_i, \tag{2.86}$$

where $q_{\parallel} = q_R$ - the magnitude of wavevector of the surface phonon. With the surface phonon wavevector expressed using (2.76) and the incident light wavevector given by $k_i = \dfrac{2\pi}{\lambda_i}$ [128] Eq. (2.86) becomes

$$\frac{2\pi\nu_R}{v_R} = \frac{4\pi}{\lambda_i}\sin\theta_i. \tag{2.87}$$

Solving (2.87) for the velocity of the surface phonon v_R leads to

$$v_R = \frac{\nu_R\lambda_i}{2\sin\theta_i}. \tag{2.88}$$

The surface of the opaque material is not only a boundary for the light but also serves as a mechanical boundary and affects the excitation spectrum of the solid [121]. The component of the wavevector that is perpendicular to the surface is undefined, but the existence of the parallel component of the wavevector permits new excitations. Depending on the thickness and symmetry of the material and polarization,

amplitude, frequency and velocity of the modes the new modes they are classified as Rayleigh, Lamb and Love waves. The surface Rayleigh waves are polarized in the sagittal plane. The amplitude of their displacement decreases exponentially with distance into crystals. They can be observed on the free surface of both isotropic and anisotropic media. All the elastic modes of a film are collectively referred to as Lamb modes [131]. Lamb modes are bulk transverse modes combined with evanescent longitudinal mode strongly localized at the surface. They are observed in free standing and supported films. Lamb modes propagate through reflections at the plate boundaries and their velocities lies between the velocities of transverse and longitudinal bulk phonons. The number of Lamb modes observed in supported films depends on the ratio of the velocity of the transverse (shear vertical) bulk phonon in the substrate and in the film [137]. Love modes are shear horizontal waves propagating in a supported films of finite thickness. They are characterized by one evanescent wave extending into the substrate. Their existence is possible only when the velocity of the shear horizontal transverse phonon in the substrate is greater than the velocity of the corresponding phonon in the film [131], [137].

Chapter 3

Experiment

3.1 Sample Preparation

The p-Si samples used in this study were prepared by electrochemical etching of crystalline silicon (c-Si) wafers in an electrolyte consisting of 49% hydrofluoric acid (HF) and anhydrous ethanol (C_2H_5OH) mixed in 1:1 proportions by volume. The parent material was boron doped p^+, 500-550 μm thick <100> oriented silicon substrates with resistivity between 0.005 and 0.02 Ωcm. All p-Si samples were made in the dark, at room temperature and at atmospheric pressure.

A home-built, teflon electrochemical cell [138] presented in Figure 3.1 was used for p-Si sample preparation. The seal between the teflon and the silicon wafer is provided by a rubber O-ring pressed against the sample so that only the front side of the sample is exposed to the HF - based electrolyte. The fabrication process requires forward bias of the wafer and current densities lower than the critical value at which electropositive occurs [7]. A copper sheet in intimate contact with the back side of

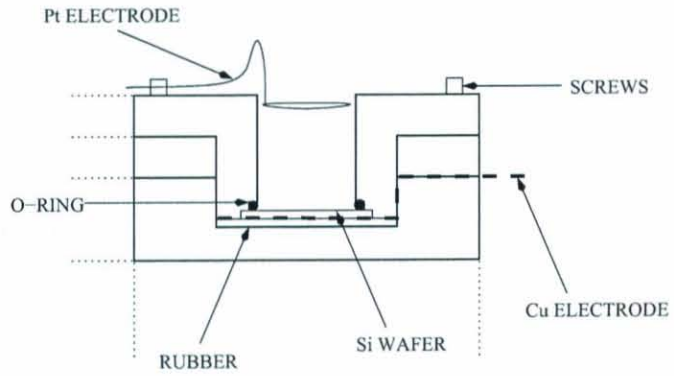

Figure 3.1: Cross section of the electrolytic cell.

the wafer and connected to the positive terminal of a power supply served as the working electrode. The counter electrode was a loop of platinum wire of a diameter comparable to that of the cell's opening (~13 mm). In this experiment the samples were produced using currents between 15 and 300 mA supplied by a programmable constant current source (Keithley 220). Prior to the etch each sample underwent a 60 s dip in 49 % HF to remove native oxide. After the etch, each sample was rinsed under running water and then immersed for 1 min in pentane. The samples were then dried in air at room temperature. The purpose of the pentane is to maintain the quality of the porous layer since it reduces the capillary tension and prevents cracking of the porous structure during drying. Moreover, it shows no chemical interaction with p-Si [139]. The etch times t_i were varied in order to obtain layers with a thickness h of a few μm.

The porosity of the samples was determined using a gravimetric method. It uses

the fact that an aqueous solution of potassium hydroxide (KOH) preferentially etches away the p-Si layer while leaving the surrounding c-Si untouched [140]. The KOH solution was prepared by dissolution of 9.97 g of KOH pellets in 990 ml of tap water. It is worth mentioning that tap water was used to prepare the KOH solution because it was found that use of nanopure water resulted in etching of the c-Si parts of the sample. In order to determine the porosity cleaved c-Si samples were weighed three times: before porosification (m_1), after the p-Si layer was formed (m_2) and again after the porous material was removed using the 4:1 solution of 1% KOH mentioned above and anhydrous ethanol (C_2H_5OH) (m_3). All masses were recorded using a Sartorius CP225D microbalance with resolution $\delta m_i = 10^{-8}$ kg. Such high precision is required as the mass loss, Δm observed during the etch of the samples can be of the order of 10^{-6} kg. The porosity was calculated using the following equation [7]:

$$\xi = \frac{m_1 - m_2}{m_1 - m_3}. \tag{3.1}$$

The uncertainty δm_i in each mass value m_i, was determined by taking three measurements and calculating the standard deviation. Due to the systematic uncertainty of the balance the minimum error in mass δm_{min} is equal to its resolution. If the standard deviation was larger than the systematic uncertainty of the balance, it served as the uncertainty in the mass measurement. If it was smaller, the systematic uncertainty in the balance was taken as δm_i. It is noted that a disadvantage of the gravimetric method is that it results in destruction of the porous layer and therefore the sample cannot be used for any other experiments. The porosity and density ρ_{p-Si}

of the p-Si layers are connected by the relationship $\rho_{p-Si} = (1-\xi)\rho_{Si}$, where ρ_{Si} is a density of c-Si (2330 km/m^3).

A plot of porosity versus the applied current and current density is presented in Figure 3.2. As can be seen, the porosity is a linear function of current i over the range explored (and current density j) and can be expressed as $\xi = a_\xi + b_\xi i$ with $a_\xi = 36 \pm 3\%$ and $b_\xi = 0.17 \pm 0.02\% \cdot mA^{-1}$. Although it appears that the etching occurred with zero current applied, it should be noted that the lowest current value that resulted in layers of consistent porosity was 15 mA. The slope of the plotted line for the volumetric concentration of HF (25% used here) is lower than those reported for lower concentrations and is therefore consistent with previous reports [7]. As can be seen in Fig 3.2, the chosen range of currents resulted in single layers with porosities ranging from ~30% to ~72%.

The gravimetric method can also be used to calculate the porous layer thickness h according to the following equation [7]:

$$h = \frac{m_1 - m_3}{A\rho_{Si}}, \tag{3.2}$$

where A=(1.47±0.02)·10^{-4} m^2 is the area of the etched layer. Knowledge of the layer thickness is necessary in order to determine etch rates for each current. Also as the layer thickness is chosen to be larger than the penetration depth of the light (the distance at which the power of the beam decreases to $1/e$ of its incident value). This assures that the influence of the crystalline substrate can be ignored and p-Si film

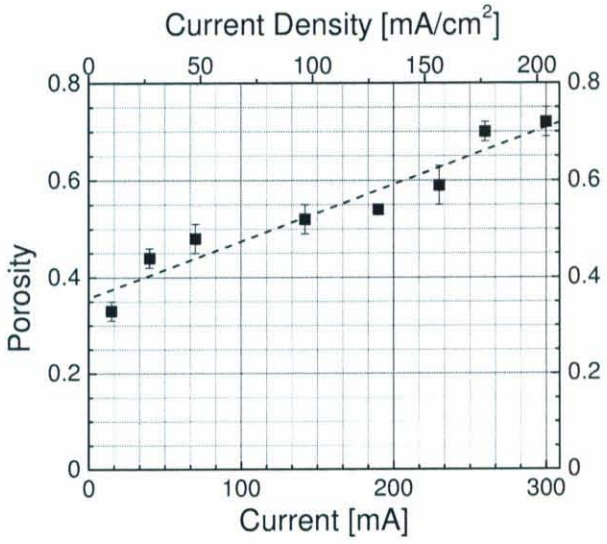

Figure 3.2: Plot of porosity versus the applied current (bottom axis) and current density (top axis) for ethanoic HF solution.

can be treated as a semi-infinite medium. It is noted that individual measurements of the area carry significant uncertainty that is then carried into the calculations of the thicknesses and etch rates. The precise values of etch rates are required for the formation of the SLs. Thicknesses of individual layers are used as input information for the determination of the values of effective elastic constants using Grimsditch-Nizzoli model. To avoid this problem another set of thickness measurements was obtained by performing scanning electron microscopy (SEM) measurements on cleaved cross-sections. Sample SEM images of single layer films are shown in Figs. 3.3, 3.4 3.5 and 3.6. In first two micrographs (Figs. 3.3, 3.4) and in the last one (Fig. 3.6) the difference between the porous layer and crystalline sample is clearly visible. The third

picture shows the c-Si left after the p-Si layer was removed using a mixture of KOH and ethanol. The sample was tilted so the difference between the top of the wafer and the bottom of the removed layer can be seen.

The values of etch rates obtained both gravimetrically (e_r^{KOH}) and using SEM (e_r^{SEM}) are compared in Figure 3.7, which presents the dependence of the etch rate on the applied current. The values obtained using SEM are used for all further experiments and calculations due to higher accuracy. The dependence of the etch rate e_r^{SEM} on the current is characterized by linear equation $e_r^{SEM} = a_{e_r^{SEM}} + b_{e_r^{SEM}} i$ with $a_{e_r^{SEM}} = 0.57 \pm 0.03\ nm \cdot s^{-1} mA^{-1}$ and $b_{e_r^{SEM}} = 13 \pm 6\ mA \cdot s^{-1}$. The etch rates obtained from the SEM measurements of layer thicknesses were used to calculate the etching times $t^{[1]}$ and $t^{[2]}$ needed to create a superlattice with the desired modulation wavelength Λ and thickness fractions $f^{[\zeta]}$ as defined by Eq. (2.55).

Refractive indices, n_B, of the p-Si layers were calculated using Bruggeman's model [141] for effective media [70]

$$1 - \xi = \frac{(1 - n_B^2)(N^2 + 2n_B^2)}{3n_B^2(1 - N^2)}, \tag{3.3}$$

where N=4.22 is the refractive index of c-Si at $\lambda_i = 532$ nm. The uncertainty in the porosity determines the possible range of variation of the refractive index. The uncertainty in the latter is calculated by adding the value half of the difference between the refractive index calculated for $\xi + \delta\xi$ and $\xi - \delta\xi$ to n_B..

Table 3.1 presents fabrication conditions (etching current, time) and resulting

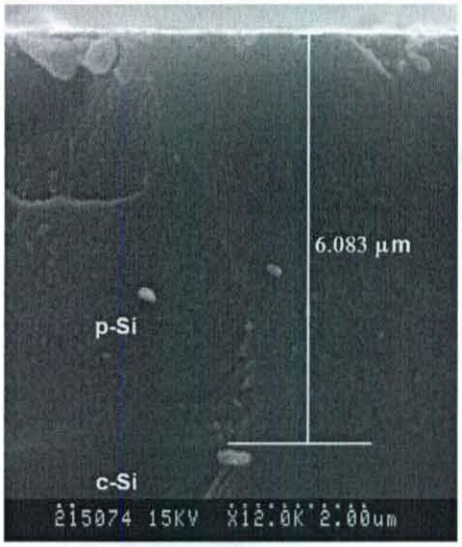

Figure 3.3: SEM image of 33% porous layer etched for 300 s.

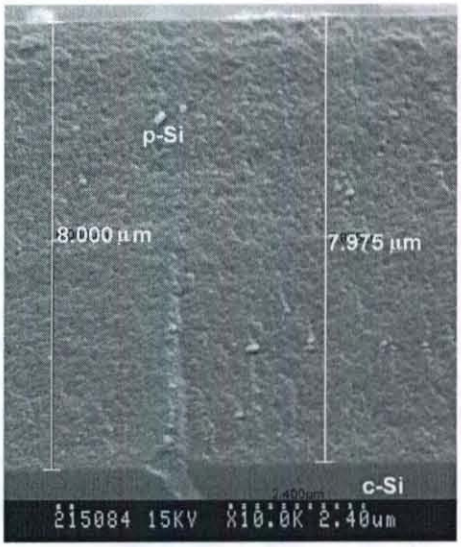

Figure 3.4: SEM image of 44% porous layer etched for 247.5 s.

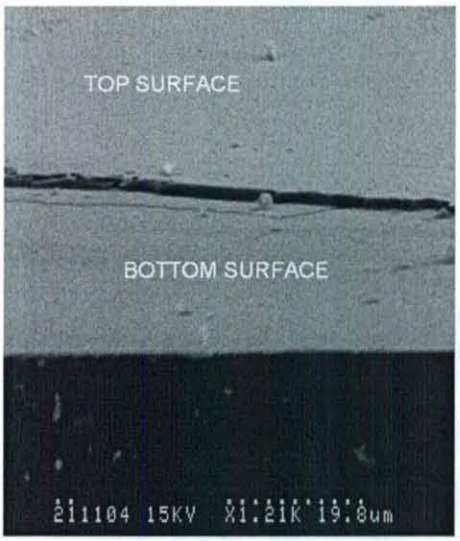

Figure 3.5: SEM image of the leftover c-Si after removal of 59 % layer etched for 52 s.

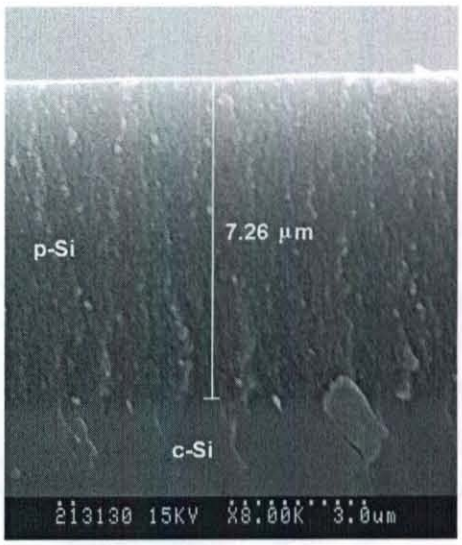

Figure 3.6: SEM image of 72% porous layer etched for 43 s.

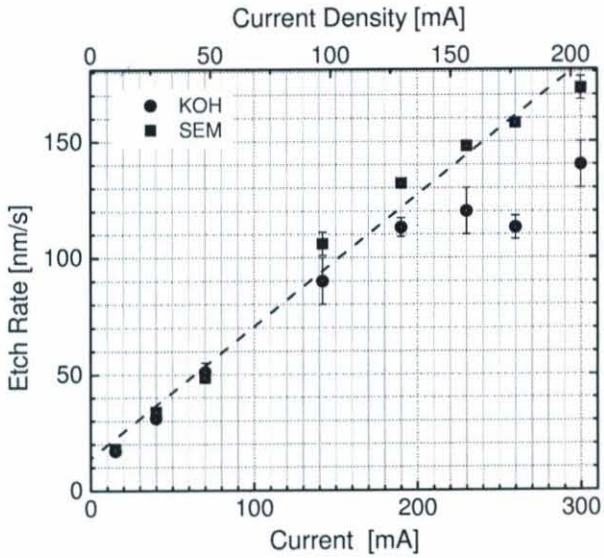

Figure 3.7: Plot of etch rates obtained via SEM measurement and gravimetrically versus the applied current (bottom axis) and current density (top axis).

porous film parameters (porosity, density, refractive index and etch rate) for each of the single layer films used in this study. The values are averages of data obtained for at least two samples prepared under the same conditions.

The creation of multilayered structures is possible as the etching process is self-limited as mentioned in Section 1.1.1. A schematic picture of a cross section along the XZ plane of a multilayered film is shown in Fig. 2.3. All investigated superlattices and multilayered structures were prepared by variation of the electric current between two values $I^{[1]}$ and $I^{[2]}$ for a predetermined number of cycles. The samples underwent the same pre- and post-etching treatment as the single layers did and the same teflon cell, electrolyte and power supply were used.

Table 3.1: Etching currents and times and resulting film porosity, density, refractive index, and etch rates of single layer porous silicon films.

Current I [mA]	Time t [s]	Porosity ξ [%]	Refractive Index n_B	Density ρ [kg/m^3]	Etch Rate e_r^{KOH} [nm/s]	Etch Rate e_r^{SEM} [nm/s]
15	300	33 ± 2	3.14 ± 0.07	1560 ± 90	17 ± 1	17.9 ± 0.1
40	250	44 ± 2	2.72 ± 0.08	1300 ± 60	31 ± 1	33.9 ± 0.8
70	160	48 ± 3	2.56 ± 0.08	1210 ± 80	51 ± 4	48.5 ± 0.6
142	75	52 ± 3	2.40 ± 0.10	1100 ± 60	90 ± 10	106 ± 5
190	60	54 ± 1	2.31 ± 0.04	1070 ± 20	113 ± 4	132 ± 1
230	52	59 ± 2	2.11 ± 0.09	960 ± 30	120 ± 10	148 ± 1
260	50	70 ± 2	1.68 ± 0.07	700 ± 20	113 ± 5	158 ± 1
300	43	72 ± 3	1.60 ± 0.10	650 ± 30	140 ± 10	173 ± 5

Sample SEM micrographs of the cross-section of multilayered structures are presented in Fig. 3.8 and 3.9. The layering is clearly seen in the multilayer with $\Lambda \sim$100 nm presented in Fig 3.8. Individual constituent layers with layer thickness less than 100 nm could not be seen with SEM due to the limitations on the instrument resolution. The overall thickness of the superlattice and the number of bilayers served as indirect confirmation that the value of the modulation wavelength is equal to that determined from the etch rate in Table 3.1.

In order to ensure that the etching process stopped after the planned number of cycles 10 μs etch stops were introduced after the formation of each bilayer. The fact that etch stops had to be introduced after formation of each bilayer instead of just at the end of SL formation is due to the factory settings. Thus the presence of the etch stops can influence the porosity of the layer, if the length of the stop is at least order of magnitude larger than the etching time [142]. In our case, depending on the

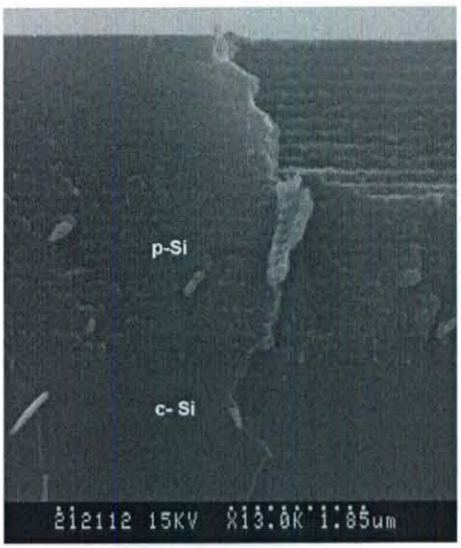

Figure 3.8: SEM images of a 59%-33% p-Si multilayered structure with $d \sim$100 nm.

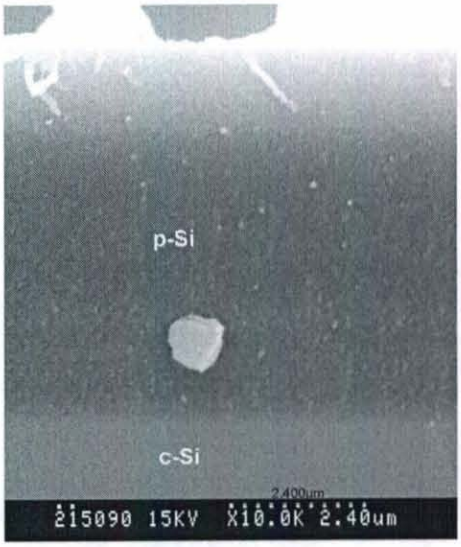

Figure 3.9: SEM images of a 59%-33% p-Si multilayered structure with $d \sim$10 nm.

etching current, etch times are 4 or 5 orders magnitude longer than the stop time. The presence of such short etch stops should not influence the porosity of the layers or the etch rate compared to the single layers, which were etched with no breaks.

The average porosity of each superlattice ξ_{SL} was calculated according to the formula

$$\xi_{SL} = f^{[1]}\xi^{[1]} + f^{[2]}\xi^{[2]}, \tag{3.4}$$

where the $\xi^{[\zeta]}$ are the porosities of constituent layers and $f^{[\zeta]}$ are the thickness fractions. This method was used rather than calculating porosity gravimetrically due to the fact that the p-Si single layers are well characterized. Furthermore the averaging of the results takes care of possible slight discrepancies in porosity and thickness

Table 3.2: Etching currents and times, structural information, porosities, densities and refractive indices of multilayered films

Currents		Times		Layer Thicknesses		Porosity	Density	Refractive Index	
$I^{[1]}$	$I^{[2]}$	$t^{[1]}$	$t^{[2]}$	$d^{[1]}$	$d^{[2]}$	ξ_{ave}	ρ_{ave}	n_B	n_R
[mA]		[ms]		[nm]		[%]	[kg/m^3]		
230	15	67.57	871.5	10	15.6	43±2	1330±60	2.8±0.2	2.7±0.2
230	40	67.57	495	10	20	49±2	1190±50	2.5±0.2	2.5±0.2
230	70	67.57	218	10	10	54±3	1080±60	2.3±0.2	2.3±0.2
230	142	67.57	99.0	10	10	56±3	1025±55	2.25±0.3	2.25±0.2
230	190	67.57	75.76	10	10	57±2	1000±35	2.2±0.1	2.2±0.2
230	260	67.57	63.29	10	10	65±3	820±40	1.9±0.2	1.9±0.2
230	300	67.57	59.5	10	10	66±3	800±40	1.8±0.1	1.8±0.2

between the samples. The densities of the superlattices were calculated in the same manner as for the single layers. The refractive indices were calculated using the Bruggeman method for effective media [141], n_B, according to equation Eq. (3.3), and the Rytov method for composite materials [111], [143], n_R. For non-magnetic media the Rytov equation takes the form:

$$n_R = \sqrt{\varepsilon_R} = \sqrt{f^{[1]}\varepsilon^{[1]} + f^{[2]}\varepsilon^{[2]}}, \tag{3.5}$$

where $\varepsilon^{[\zeta]}$ is the dielectric permittivity of the individual layer, ε_R is the dielectric permittivity of the superlattice. The values of refractive indices obtained using both methods agree within uncertainty for all superlattices. The refractive index values together with electric currents $I^{[\zeta]}$, etch times, $t^{[\zeta]}$, layer thicknesses, $d^{[\zeta]}$, average porosities ξ_{SL} and densities ρ_{SL} are tabulated in Table 3.2.

3.2 Brillouin Light Scattering Setup

The optical setup used for Brillouin light scattering is shown in Fig. 3.10 and consists of two major components - a source of light and a frequency analyzer. Vertically polarized incident light at 532 nm is generated by a Coherent $Verdi\ Nd:YVO_4$ single mode laser operating on second harmonic. As all experiments required horizontally polarized light, a half wave plate (HWP) was used to rotate the plane of polarization from vertical to horizontal. The 2 W output power of the laser is initially reduced by a set of variable neutral density filters $VNDF_1$. The beam is then incident on a beam splitter BSP, where a small fraction of its power is reflected and directed to the tandem Fabry-Pérot interferometer TFP-1 using mirror M_2. This part of the beam serves as a reference beam and is used to maintain the mirror alignment for both interferometers. It is also, together with the shutter system, used to prevent saturation of the detector during scanning over the high intensity region of elastically scattered light. The elastically scattered light is blocked from entering the interferometer and the much less intense reference beam is used instead. The intensity of the reference beam is controlled by the variable neutral density filter $VNDF_2$. The light that is transmitted through the BSP is incident on a mirror M_1 that changes its direction by 90^o. The power of the beam is reduced to the desired level (usually less than 100 mW) by another set of filters F and by a variable neutral density filter $VNDF_3$. The beam then undergoes total internal reflection on the prism P and is focused on the sample S by a lens f with a focal length of 5 cm and an f-number adjustable

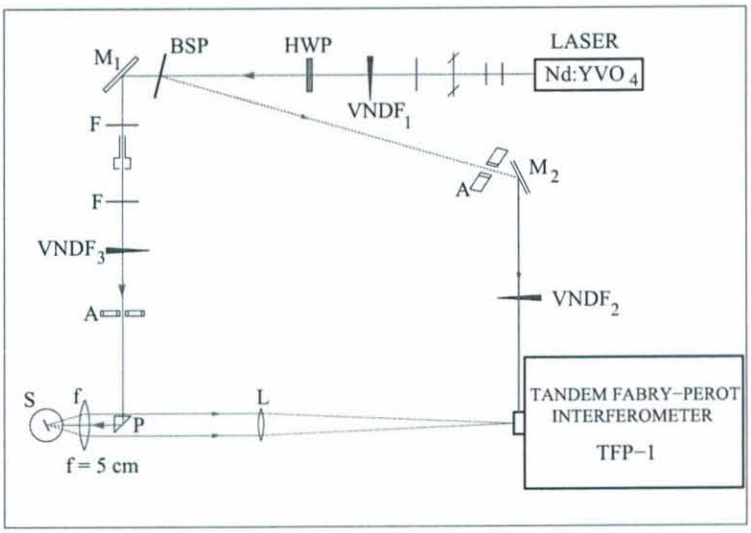

Figure 3.10: Experimental setup for Brillouin light scattering. $Nd : YVO_4$ – laser, HWP – half wave plate, BS – beam splitter, M – mirror, F – filter, VNDF – variable neutral density filter, A – aperture, BF – bandpass filter, L – lens, P – prism, f – focusing/collecting lens, TFP-1 – tandem Fabry-Pérot interferometer.

over the range 1.8 - 22. The two f-numbers used during collection of the spectra depended on the incident angle θ_i. For $\theta_i < 10^o$ an f-number of 4.0 was used while an f-number of 2.8 was chosen for the spectra collected with higher incident angle. The larger f-number was required in the case of small incidence angle in order to ensure no specularly reflected light from the sample was directed into the spectrometer by the collection optics. The same lens collects the scattered light which is then focused on the adjustable pinhole of the interferometer by a lens L of focal length 40 cm. The pinhole size for this set of experiments was set to 450 μm. Finally, the scattered light enters the tandem Fabry-Pérot interferometer TFP-1 where it gets frequency analyzed.

The TFP-1 (JRS Scientific Instruments) combines two almost identical Fabry-Pérot etalons. Each Fabry-Pérot interferometer is constructed of two parallel, highly reflective flat mirrors facing each other and separated by distance L_i [144].The only wavelengths that are transmitted by the individual etalon with the spacing L_i are those satisfying condition

$$L_i = \frac{m\lambda}{2} \tag{3.6}$$

where $m = 1, 2, 3...$. The resonance frequencies ν_m of an interferometer with distance L_i between the mirrors are therefore [128]

$$\nu_m = m\frac{c}{2L_i} = m\nu_F, \tag{3.7}$$

where c is speed of light and ν_F is the difference between two successive resonant frequencies, called the free spectral range (FSR). The FSR of the FP1 was always chosen to include the frequency shift range of interest. In the current work the Brillouin shifts are usually between 10 and 50 GHz and thus the FSR was typically set to ~100 GHz.

The Fabry-Pérot interferometer serves as a spectrometer by varying distance L_i to achieve transmission of different wavelengths and therefore frequencies. The instrument acts as a tunable filter with transmission close to one over a narrow interval and diminishing rapidly outside the interval [121]. The transmitted light has sharp peaks centered at frequencies described by Eq. (3.7). This strict condition is relaxed if the

interferometer has losses introduced by the imperfect reflection of the mirrors and absorption of the medium between them [145]. The spectrum then consists of peaks characterized by certain width at half maximum, $\delta\nu_m$. The width $\delta\nu_m$ is related to the separation between successive resonant frequencies through the finesse $\mathfrak{F}$

$$\mathfrak{F} = \frac{\nu_m}{\delta\nu_m}. \tag{3.8}$$

The finesse is mainly dependent on the reflectivity of the mirrors but it is also related to the mirror flatness and instrumental aperture as well. For small values of finesse the transmission of all frequencies is observed. With the increase in $\mathfrak{F}$ the transmission occurs only for a narrow band of frequencies centered at the value given by Eq. (3.7). For given FSR, the greater the finesse the smaller the width at half maximum, according to Eq. (3.8) [146]. For experiments performed in this work the value of $\mathfrak{F}$ is typically ~ 100. The finesse puts an upper limit on contrast C, the ratio of maximum to minimum transition given by [121]

$$C \simeq \frac{4\mathfrak{F}^2}{\pi} \lesssim 10^4. \tag{3.9}$$

As the function describing the behaviour of the set of etalons is given by a product of their transmission functions, the contrast of the set increases when two or more etalons are put in series, providing their scanning is synchronized or when multiple passes of light through the same interferometer, providing the mirrors remain parallel [145].

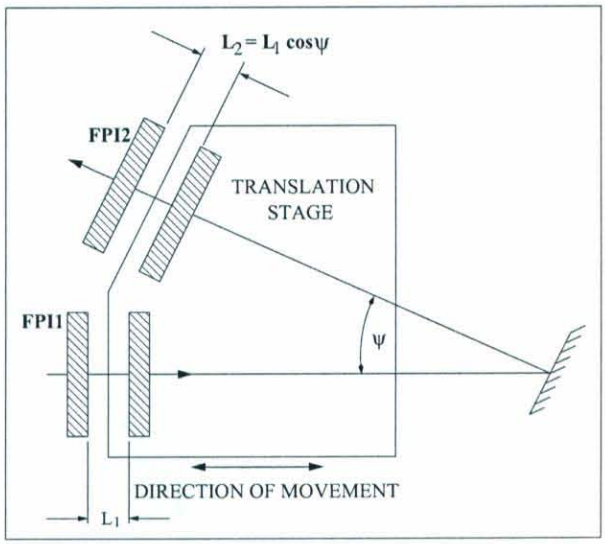

Figure 3.11: Tandem Fabry-Pérot Interferometer. After [147].

The design of the tandem Fabry-Pérot interferometer combines two interferometers with unequal distance L_i using a scanning stage as shown in Figure 3.11. In each of the interferometers in the tandem, one of the mirrors is mounted on a movable stage, the other on a device that allows slight adjustments in mirror tilt around the horizontal and vertical axis situated in plane of the mirror. The normal of the first interferometer, FP1, lies in the direction of stage movement, the normal of the second one, FP2 is at an angle Ψ. The spaces between mirrors are therefore L_1 and $L_1 \cos\Psi$, respectively, so for any value of $\Psi \neq 0$ the distance between etalons differ. The frequencies transmitted by the combination of interferometers must simultaneously satisfy Eq. (3.7) for FP1 and FP2. In order to scan a given increment in frequency, the distance changes between mirrors δL_1 and δL_2 must satisfy

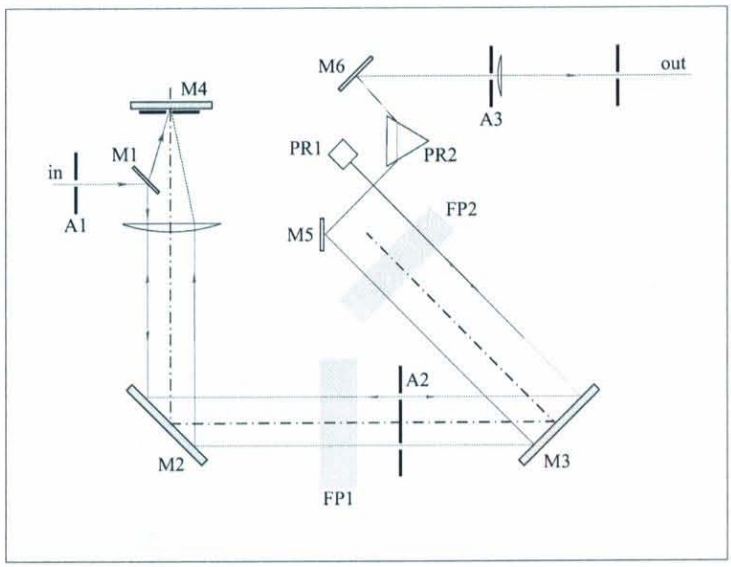

Figure 3.12: Tandem optics. FPI – Fabry-Pérot interferometer, PR - prism, M – mirror, A – aperture, in – input pinhole, out – output pinhole. After [147].

$$\frac{\delta L_1}{\delta L_2} = \frac{L_1}{L_2}. \tag{3.10}$$

A movement of the stage and change of spacing between mirrors in $FP1$ by scanning distance δL_1 creates a change of spacing $\delta L_1 \cos \Psi$ in $FP2$ thereby keeping the scanning condition given by Eq. (3.10) satisfied [147].

A simplified diagram of the TFP-1 optics is shown in Fig. 3.12. After entering the interferometer, the light passes through an aperture A1 which defines the accepted cone of light. The light is reflected towards the collimating lens L1 and directed by a mirror M2 to first Fabry-Pérot interferometer FPI1, where it passes through another aperture A2 and is directed by M3 towards the second Fabry-Pérot interferometer

FPI2. After transmission through the second interferometer, light is reflected back by prism PR1. It passes through both interferometers and is focused on the mirror M4 which is placed so that it reflects the light back for a final pass through the system. After that pass the light is directed by set of mirrors (M5 and M6) and a prism PR2 to the adjustable output pinhole set to size of 700 μm. Three passes through each plane parallel Fabry-Pérot interferometer improves the contrast enough for a measurement of Brillouin scattering for backscattering experiments from opaque materials, which are examined in this work. The tandem Fabry-Pérot interferometer is stabilized by external control unit. The scattered photons are counted by photodetector and displayed using *Ghost* software (University of Perugia).

Chapter 4

Single Porous Silicon Layers

A set of Brillouin spectra with incident angle varying from $\sim 5^o$ to $\sim 75^o$ was collected in air for each single layer sample. The angle of incidence was measured, from the normal to the surface of the sample, which is a direction equivalent to the z-axis [001] in the porous layer. The range of incident angles was chosen to be as wide as possible in order to allow investigation of the directional dependence of the frequency shifts and consequently that of the velocities v_R of the surface Rayleigh phonon (R) and v_T and v_L of the bulk quasi-transverse (QT) and quasi-longitudinal (QL) phonons, respectively.

4.1 Brillouin Spectra

The spectra collected from the single p-Si films are presented in Figs. 4.1(a)–(d) and 4.2(a)–(d). In each figure the vertical scale of the figures is kept the same to facilitate comparison between spectra for different incident angles and also between

samples. The numbers on the right hand side of the spectra indicate the value of the incident angle.

Although qualitatively the spectra collected from each sample are similar some characteristic features are observed. First of all, the change in the signal-to-noise ratio, the intensity of the peaks, and their full width at half maximum, with the porosity of the p-Si layers can be noticed. As the porosity of the layers increases the signal to noise ratio increases and, in all cases with exception of the 48% porous sample, the absolute intensities of the Brillouin peaks increase. This may be a consequence of the fact that as the opacity decreases so does the imaginary part of the refractive index, which is responsible for the attenuation of the light as it enters the film [148], and therefore the scattering volume increases. This is followed by the fact that as the opacity of the sample decreases both ripple and elasto-optic scattering contribute to the spectral peak intensities for Brillouin scattering [69]. The quality of the spectra collected from the samples characterized by lower porosities (less than 50%) prevents the resolution of all the peaks and results in an incomplete set of frequency shift values. In addition, the obtained peak parameters (especially intensity) carry significant uncertainty.

In general, the sharp and highly intense mode labeled R can be observed at high incident angle for all the samples. It can only be resolved at higher incident angles as its frequency shift changes with angle such that and for lower incident angles it is in the region of the spectrum cut off by a shutter. This peak is identified as originating due to the surface Rayleigh mode because its frequency shift is the smallest of all

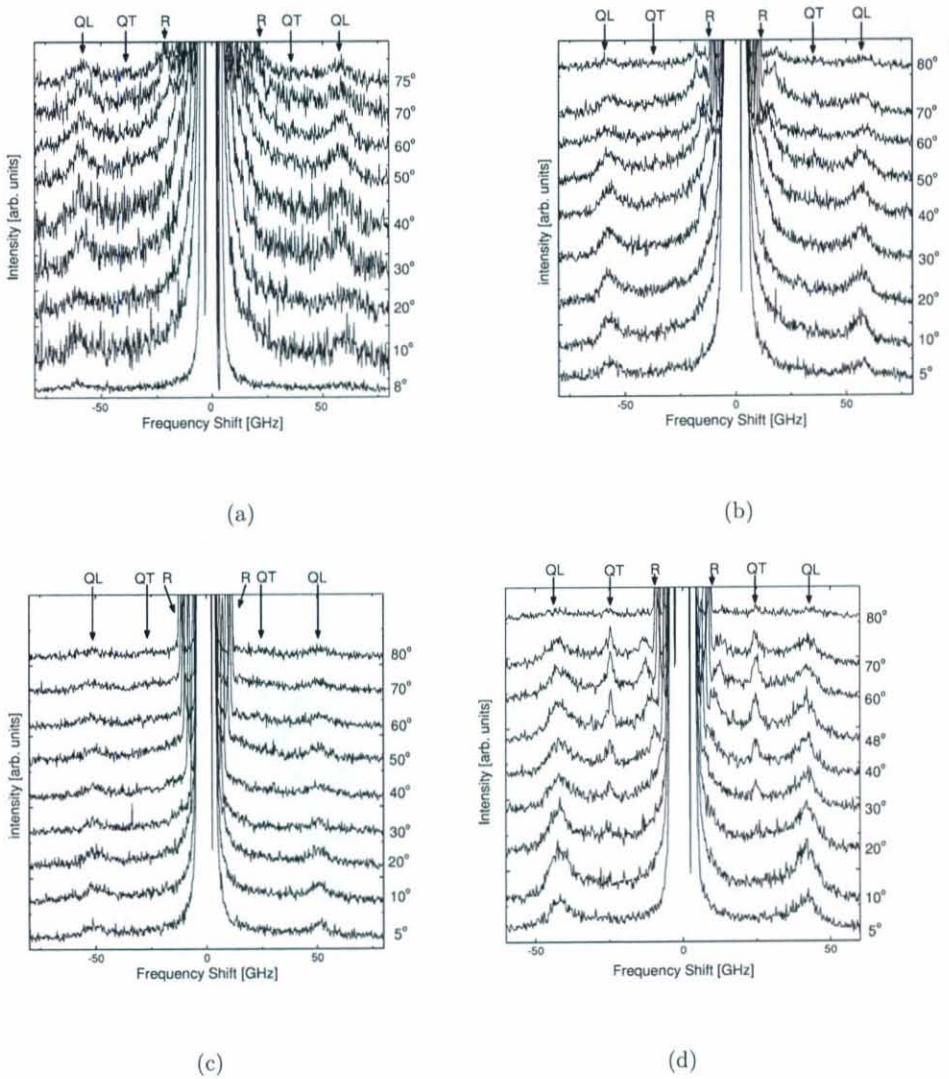

Figure 4.1: Spectra collected from the p-Si layers of 33% (a), 44% (b), 48% (c) and 52% (d) porosity. The symbols above (R, QT, QL) the diagrams indicate the phonons due to which peaks originate (surface Rayleigh, quasi-transverse and quasi longitudinal, respectively). The labels to the right indicate the incidence angle measured from the normal to the sample in the air.

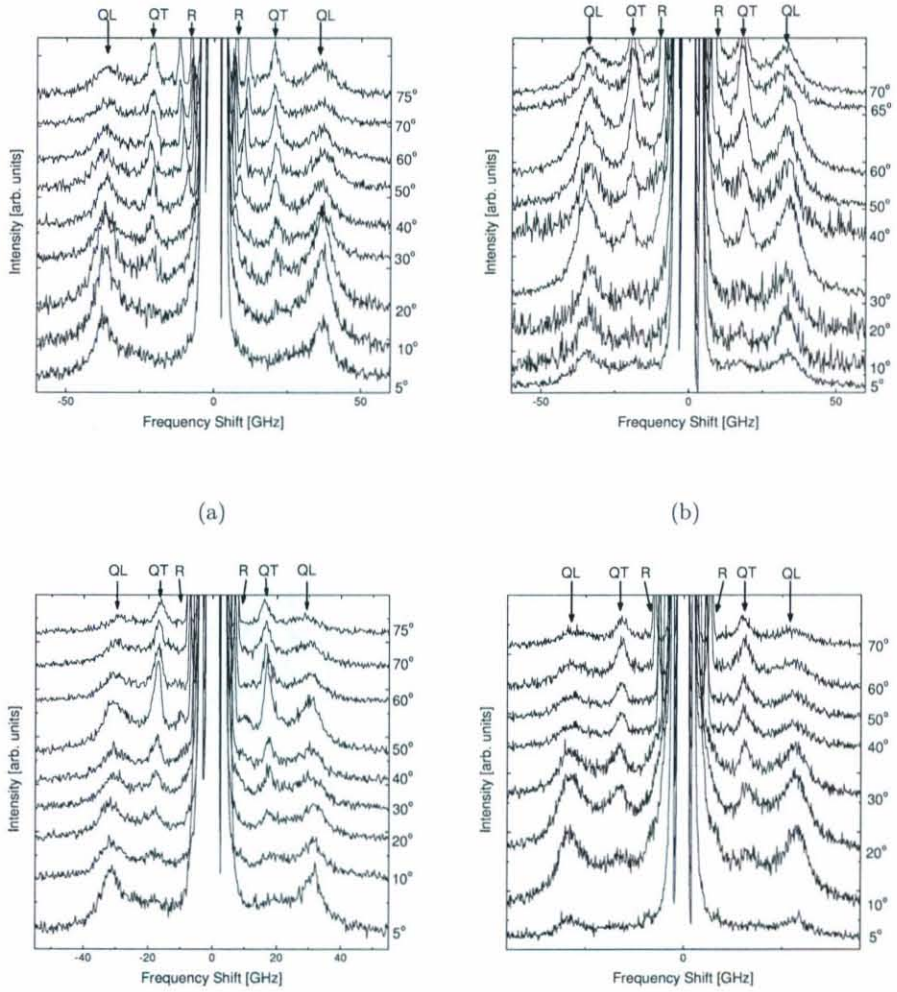

Figure 4.2: Spectra collected from the p-Si layers of 54% (a), 59% (b), 70% (c) and 72% (d) porosity. The symbols above (R, QT, QL) the diagrams indicate the phonons due to which peaks originate (surface Rayleigh, quasi-transverse and quasi longitudinal, respectively). The labels to the right indicate the incidence angle measured from the normal to the sample in the air.

observed peaks and it depends linearly on the sine of the incident angle.

In all of the spectra apart from those collected from the 33% porous film, a broad shoulder on the peak due to surface Rayleigh mode can be seen. It covers the frequency range from ~7 GHz to ~20 GHz for low porosity samples and ~5 GHz to ~15 GHz at p-Si samples of high porosity. This feature is similar to that observed by Sandercock [127] for opaque polycrystalline metals and crystalline GaAs and Cr. The intensity and width of the shoulder varies depends on the sample and the incident angle θ. Unlike in Sandercock's work, individual spectral peaks can be distinguished. Peaks identified in this region, although not labeled in the spectra shown in Figs. 4.1(a)–4.1(d) and 4.2(a)–4.2(d), are called S_i. In most cases they show some dependence on the incident angle, but there are also peaks identified within this region that are insensitive to changes in incident angle. It is highly unlikely that they are artifacts of the experimental setup as those appear as narrow peaks at low frequency shifts and are characterized by equal separation [149].

The peaks of main focus for this work, labeled QT and QL, are identified as originating due to quasi-transverse and quasi-longitudinal bulk phonons. The assignment is based on several observations. Firstly, the frequency shifts of the peaks show only weak dependence on the incidence angle, which is expected of bulk phonons as only region of up to 30^o from the z-axis inside the material is examined. Secondly, no additional peaks were observed in any of the spectra for frequency shifts larger than ~60 GHz, which is the frequency shift assigned to the QL mode for the sample

with the smallest porosity. Although phonons are always present in the material, the peaks originating due to them are not always apparent. The intensity of the QT peak increases with increasing θ whereas the intensity of the QL decreases. In fact, at $\theta < 40^o$ the QT peak is not observed for films with porosity lower than 50%.

A change in the overall quality of the spectra and intensity of the peaks with incident angle and porosity of the p-Si layer was noticed. As the raw integrated intensity of the Brillouin peaks is a function of many variables, including the number of scans and the power of the laser beam, the ratio of the absolute intensity of the quasi-transverse and quasi-longitudinal peaks was chosen to show this trend. Fig. 4.3 presents a plot of the ratio of absolute intensities, I_T/I_L as a function of incident angle. For the spectra collected from films of higher porosity the ratio lies between 0.5 and 1.75 for all the incident angles. For all samples an increase of I_T/I_L with increasing incident angle can be observed. As it is not possible to obtain the values of the intensities for the quasi-transverse phonon peak in the case of the lower porosity samples, the presented ratios appear to be scattered. The lack of data is because the peak due to the quasi-transverse phonon is very weak and the spectra are noisy. The low value of I_T for all these samples suggests a low I_T/I_L ratio for low porosity samples at low incident angles. What is also not seen in the plot in order to keep it more transparent are the uncertainties of the values, which, especially in case of lower porosity layers, are quite high.

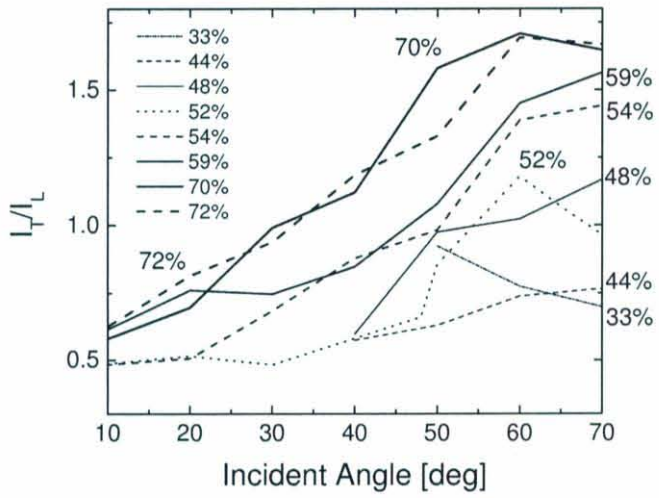

Figure 4.3: Angular dependence of the ratio of intensities of transverse and longitudinal phonons.

4.2 Frequency Shifts and Phonon Velocities

The positions of peaks originating due to the surface, quasi-transverse and quasi-longitudinal phonons are labeled in the topmost spectrum of each set. The frequency shifts of all peaks are presented in Tables 4.1 - 4.4. Unless indicated otherwise, the presented values are averages of the shifts determined for Stokes and anti-Stokes processes with uncertainty calculated by averaging the error in each frequency shift given by software while fitting the frequency shift of each peak. The fit of a sample spectrum collected from a single layer with porosity of 59±2 % at the incident angles of 5^o and 60^o are presented in Fig.4.4.

As certain features are characteristic to groups of samples, the samples can be

Table 4.1: Frequency shifts and phonon velocities of samples 2.9B#1, etched for 300 s with current of 15 mA, resulting in 33±2% porosity and 6.06 μm thickness and 2.14#2, etched for 250 s with current of 40 mA, resulting in 44±2% porosity and 8.50 μm thickness.

Sample	θ_i	θ_i'	Frequency Shift						Phonon Velocity	
			R	S_1	S_2	S_3	QT	QL	v_-	v_+
	[deg]	[deg]	[GHz]	[GHz]	[GHz]	[GHz]	[GHz]	[GHz]	[km/s]	[km/s]
2.9B#1	8	2.5	—	—	—	—	—	59.5±0.8	—	5.0±0.2
	10	3	—	—	—	—	—	59.6±0.6	—	5.1±0.2
	20	6	—	—	—	—	—	57.7±0.8	—	4.9±0.2
	30	9	—	—	—	—	—	54.8±0.6	—	4.6±0.2
	40	12	—	—	—	—	–	55.9±0.6	—	4.9±0.2
	50	14	8.616±0.005	—	—	—	28±3	58.1±0.8	2.3±0.3	4.9±0.2
	60	16	10.150±0.004	—	—	—	29±3	57.8±0.8	2.4±0.3	4.9±0.2
	70	18	10.660±0.002	—	—	—	33±2	57.7±0.9	2.9±0.2	4.9±0.2
	75	119	10.970±0.004	—	—	—	36±3	58±1	3.1±0.3	4.9±0.2
2.14#12	5	2	—	—	—	—	—	56.1±0.3	—	5.5±0.2
	10	4	—	—	—	—	—	55.5±0.2	—	5.4±0.2
	20	7	—	—	—	—	—	55.3±0.2	—	5.4±0.2
	30	10	—	—	—	—	—	56.9±0.2	–	5.6±0.2
	40	14	7.355±0.006	10.6±0.1	13.2±0.3	20±3	33±5	56.6±0.5	3.2±0.6	5.5±0.2
	50	17	8.649±0.006	11.9±0.1	14.5±0.2	23±2	36±3	56.8±0.5	3.5±0.4	5.6±0.2
	60	19	9.742±0.006	13.4±0.2	16.5±0.2	22±1	34±2	57.9±0.7	3.4±0.3	5.7±0.2
	70	20	10.350±0.004	14.3±0.1	17.5±0.5	22±1	34±2	56.4±0.8	3.3±0.3	5.5±0.2
	80	21	10.840±0.004	—	18.0±0.1	—	35±3	58.1±0.7	3.5±0.4	5.7±0.2

Table 4.2: Frequency shifts and phonon velocities of samples 2.13#8, etched for 160 s with current of 70 mA, resulting in 48±2% porosity and 7.8 μm thickness and 2.13#10 etched for 75 s with current of 142 mA, resulting in 52±3% porosity and 7.5 μm thickness.

Sample	θ_i	θ_i'	Frequency Shift				Phonon Velocity	
			R	S_1	QT	QL	v_-	v_+
	[deg]	[deg]	[GHz]	[GHz]	[GHz]	[GHz]	[km/s]	[km/s]
2.13#8	5	1.92	—	—	—	49.6±0.4		5.3±0.2
	10	4	—	—	—	50.6±0.3	—	5.3±0.2
	20	8	—	—	—	50.5±0.3	—	5.2±0.2
	30	11	—	—	—	50.3±0.4	—	5.2±0.2
	40	14	7.570±0.007	14.2±0.3	28±1	50.7±0.5	—	5.3±0.2
	50	17	9.119±0.006	14.8±0.3	23±1	50.5±0.6	2.5±0.2	5.2±0.2
	60	19	10.388±0.005	14.3±0.2	23±1	51.4±0.6	2.3±0.2	5.2±0.2
	70	21	11.142±0.005	—	24.1±0.9	51.1±0.6	2.4±0.2	5.3±0.2
	80	22	11.631±0.008	—	24.1±0.9	51.4±0.7	2.4±0.2	5.3±0.2
2.13#10	5	2.08	—	—	—	41.8±0.1	—	4.6±0.2
	10	4	—	—	25±1	41.8±0.1	—	4.6±0.2
	20	8	—	—	—	42.1±0.1	—	4.9±0.2
	30	12	—	—	24.9±0.1	41.4±0.1	2.8±0.1	4.6±0.2
	40	16	6.16±0.01	10.1±0.3	25.0±0.2	41.3±0.2	2.8±0.1	4.6±0.2
	48	18	7.208±0.008	11.5±0.1	24.6±0.1	41.1±0.2	2.7±0.1	4.6±0.2
	60	21	8.287±0.008	13.1±0.2	24.7±0.1	41.0±0.2	2.7±0.1	4.5±0.2
	65	22	8.55±0.010	13.3±0.2	24.6±0.2	41.2±0.2	2.7±0.1	4.6±0.2
	70	23	8.867±0.007	13.5±0.1	24.8±0.2	41.6±0.2	2.7±0.1	4.6±0.2
	80	24	9.27±0.02	14.1±0.4	25.0±0.4	43.1±0.6	2.8±0.2	4.8±0.3

Table 4.3: Frequency shifts and phonon velocities of samples 2.15#6,was etched for 60 s with current of 190 mA, resulting in 54±1% porosity and 7.9 μm thickness and 2.11#9,etched for 52 s with current of 230 mA, resulting in 59±2% porosity and 7.7 μm thickness.

Sample	θ_i	θ_i'	Frequency Shift			Phonon Velocity			
			R	S_1	S_2	QT	QL	v_-	v_+
	[deg]	[deg]	[GHz]	[GHz]	[GHz]	[GHz]	[GHz]	[km/s]	[km/s]
2.15#6	5	2	—	—	—	23±2	37.2±0.2	2.7±0.3	4.3±0.1
	10	4	—	—	—	24±1	36.82±0.08	2.8±0.2	4.24±0.08
	20	9	—	—	—	21.8±0.3	36.75±0.08	2.52±0.06	4.23±0.08
	30	13	—	—	—	21.2±0.2	36.5±0.1	2.44±0.06	4.20±0.09
	40	16	5.50±0.02	9.5±0.2	—	20.8±0.2	36.0±0.2	2.40±0.06	4.14±0.09
	50	19	6.47±0.01	10.12±0.05	—	21.3±0.1	36.9±0.2	2.45±0.06	4.25±0.09
	60	22	7.15±0.01	10.96±0.03	—	20.71±0.08	36.1±0.2	2.39±0.05	4.16±0.09
	70	24	7.54±0.02	11.46±0.03	—	20.64±0.08	35.9±0.2	2.28±0.05	4.14±0.09
	75	25	7.65±0.02	11.57±0.03	—	20.56±0.07	35.9±0.2	2.37±0.05	4.14±0.09
2.11#9	5	2	—	—	—	17.0±0.4	34.1±0.1	2.1±0.1	4.3±0.2
	10	5	—	—	—	17.6±0.5	33.5±0.2	2.2±0.2	4.2±0.2
	20	9	—	—	—	17±1	33.3±0.2	2.1±0.2	4.2±0.2
	30	14	—	12.9±0.2	13.3±0.1	19.6±0.1	34.10±0.07	2.5±0.1	4.3±0.2
	40	18	5.444±0.005	9.9±0.3	12.9±0.6	18.8±0.4	33.3±0.2	2.4±0.1	4.2±0.2
	50	21	6.944±0.003	10.4±0.1	13.5±0.3	18.7±0.1	33.2±0.1	2.4±0.1	4.2±0.2
	60	24	8.302±0.004	11.2±0.1	13.5±0.3	18.59±0.08	32.98±0.2	2.3±0.1	4.2±0.2
	65	25	8.557±0.006	12.4±0.3	—	18.4±0.1	32.8±0.2	2.3±0.1	4.1±0.2
	70	26	8.939±0.004	12.8±0.2	—	18.53±0.06	32.6±0.1	2.3±0.1	4.1±0.2

Table 4.4: Frequency shifts and phonon velocities of samples 2.15#12, etched for 50 s with current of 260 mA, resulting in 70±2% porosity and 7.9 μm thickness and 2.13#7, etched for 43 s with current of 300 mA, resulting in 72±3% porosity and 7.2μm thickness.

Sample	θ_i	θ_i'	Frequency Shift				Phonon Velocity	
			R	S_1	QT	QL	v_-	v_+
	[deg]	[deg]	[GHz]	[GHz]	[GHz]	[GHz]	[km/s]	[km/s]
2.15#12	5	3	—	—	19.6±0.7	31.57±0.09	3.1±0.2	5.0±0.2
	10	6	—	—	17.9±0.3	31.5±0.1	2.8±0.2	5.0±0.2
	20	12	—	—	18.0±0.2	31.6±0.1	2.9±0.01	5.0±0.2
	30	17	—	—	17.±0.1	30.2±0.2	2.8±0.1	4.8±0.3
	40	23	5.36±0.01	9.7±0.2	17.5±0.1	29.9±0.2	2.8±0.1	4.7±0.2
	50	27	6.30±0.01	10.3±0.2	17.18±0.05	29.8±0.2	2.7±0.1	4.7±0.2
	60	31	6.96±0.01	10.9±0.2	16.83±0.06	29.8±0.2	2.7±0.1	4.7±0.2
	70	34	7.342±0.006	—	16.45±0.08	29.4±0.2	2.6±0.1	4.7±0.2
	75	35	7.519±0.009	—	16.09±0.07	28.3±0.2	2.5±0.1	4.5±0.2
2.13#7	6	4	—	—	16±1	29.0±0.1	2.6±0.4	4.8±0.3
	10	6	—	—	16.5±0.4	28.89±0.08	2.7±0.2	4.8±0.3
	20	12	—	—	15.9±0.1	28.57±0.07	2.6±0.2	4.7±0.3
	30	18	3.97±0.02	—	15.9±0.1	28.3±0.1	2.6±0.2	4.7±0.3
	40	24	5.18±0.01	9.0±0.3	16.0±0.2	28.1±0.3	2.6±0.2	4.6±0.3
	50	29	5.953±0.005	9.8±0.2	15.7±0.08	27.7±0.2	2.5±0.2	4.7±0.3
	60	33	6.754±0.005	10.3±0.2	15.57±0.08	27.6±0.2	2.3±0.2	4.6±0.3
	70	36	7.219±0.005	10.0±0.2	15.35±0.08	27.4±0.2	2.5±0.2	4.6±0.3

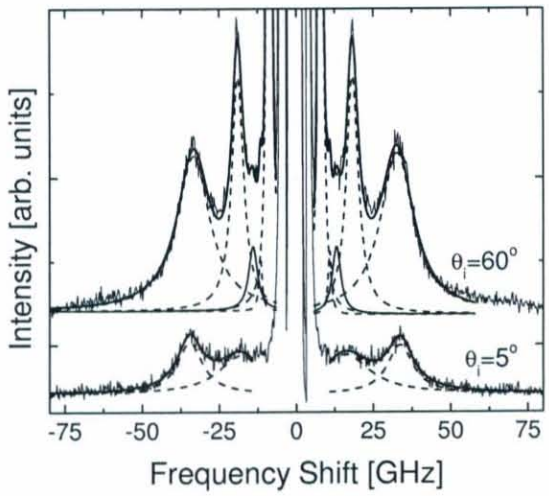

Figure 4.4: Sample spectrum of (59±2)% p-Si layer with fits of the Brillouin peaks. The individual peaks are shown using dashed line, the sum of the all peaks is indicated with thick solid line. The incident angles at which the spectra were collected are indicated next to the lines.

divided into two groups, based on porosity. The first group includes samples with porosity lower than 50%, (*i.e.* samples 2.9b#1, 2.14#2 and 2.13#8 with porosities of 33%, 44% and 48%, respectively). The second group includes samples with higher porosity, namely 2.13#10, 2.15#6, 2.11#9, 2.15#12 and 2.13#12, with porosities of 52%, 54%, 59%, 70% and 72%, respectively.

The spectra collected from samples with porosity below 50% are presented in Fig. 4.1(a), 4.1(b) and 4.1(c). It should be pointed out that the spectra collected from these samples were characterized by low signal-to-noise ratio and low intensity of the Brillouin peaks. Spectra collected from the 33% porous sample are of particularly

poor quality. Only three Brillouin peaks are seen in the spectra collected from this layer, R, QT and QL. The existence of other modes is not excluded, but it could not be confirmed either by the plot of intensity versus the frequency shift shown in Fig. 4.1(a). The frequency shifts of the three observed peaks are presented in the top part of Table 4.1. The values are plotted versus the sine of the incident angle, as shown in Fig. 4.5(a). They are identified as originating due to the Rayleigh surface phonon (R) and quasi-transverse (QT) and quasi-longitudinal (QL) phonons for reasons mentioned previously.

Although slight improvement in the quality of the spectra collected is noticed with increasing porosity within the samples belonging to the first set, no transverse mode can be distinguished below 40^o incidence angle for either of the samples. In addition to the peaks due to surface (R), quasi-transverse (QT) and quasi-longitudinal (QL) phonons, additional peaks are resolved. Two of the peaks of unknown origin, seen best in the top spectra (60^o-80^o in Fig. 4.1(b), at frequency shift between 10 and 25 GHz) show dependence on sine θ_i. The last peak in this region for the 44% porous sample, similarly to the only peak observed in spectra collected from 48% porous film, showed no dependence on the angle of incidence. The Brillouin frequency shifts for all the peaks are tabulated in the bottom part of Table 4.1 for the 44% porous layer and in top part of Table 4.2 for the 48% layer. The plots of the angular dependence of the frequency shifts are presented in Figs. 4.5(b) and 4.5(c), respectively.

The quality of the spectra improves significantly when the examined layers are

more than 50% porous. Although in a few cases the frequency shifts and intensities of some modes are uncertain and therefore not included in calculations, the quasi-transverse and quasi-longitudinal bulk phonons are observed in every spectrum. Modes of unknown origin showing linear dependence on the sine of the incidence angle are observed in spectra collected from each sample. Additionally, in the case of the 59% porous layer, a mode insensitive to the changes of the incidence angle is observed and its frequency shifts reported. The frequency shifts of the peaks are tabulated in the bottom part of Table 4.2 and in Tables 4.3 and 4.4 for 52%, 54%, 59%, 70% and 72% porous layers, respectively. The plots of phonon frequencies as function of sine of the incident angle are presented in Figs. 4.5(d)-4.6(d).

The dashed lines in Figs. 4.5(a)–(d) and 4.6(a)–(d) show the fit of frequency shift versus sine of the incident angle for all of the surface Rayleigh modes. The line represents a least-square fit with y-intercept taken to be 0. The velocities of the surface Rayleigh phonons can be calculated from the slope of the ν_R versus $\sin\theta_i$ plots (see Eq. (2.87)). As no assumption regarding the angular dependence of modes identified as S_i can be made, the dotted lines show the best fit for all the peaks identified in the region of frequency shifts higher than R and lower than QT. They could be related to the anisotropic character of the p-Si layer [150], however nothing more can be said about their character. As the origin of these modes is uncertain and they are not the main focus of this work they will not be discussed further.

As the p-Si film preserves the crystalline symmetry of the parent layer [116],

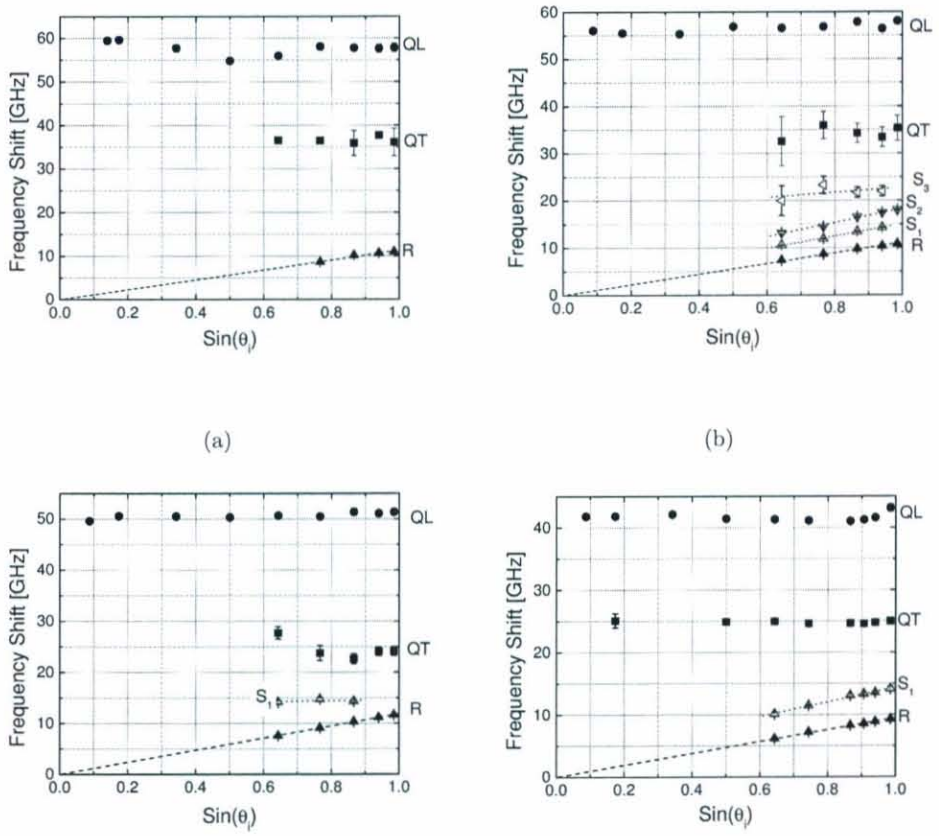

Figure 4.5: Frequency shift versus $\sin\theta_i$ for 33% (a), 44% (b), 48% (c) and 52% (d) single porous layer. The letters on the right hand side indicate the origin of the phonons. R – surface Rayleigh, S_i – unknown, QT – quasi-transverse, QL – quasi-longitudinal.

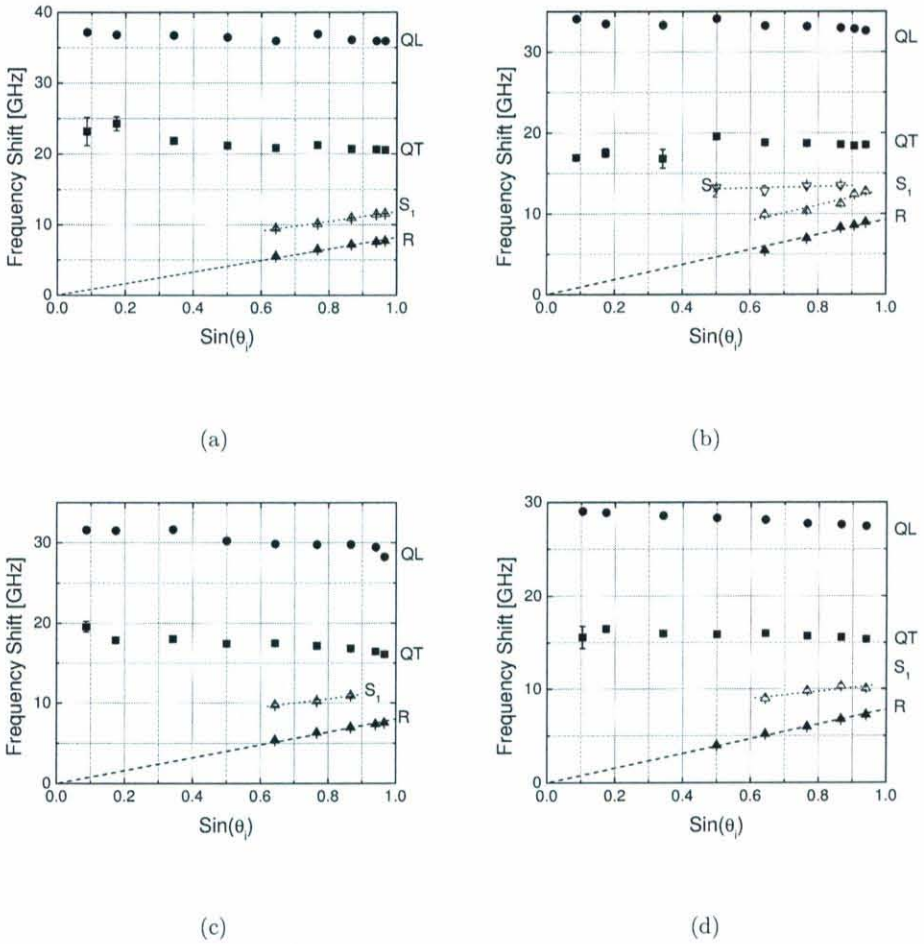

Figure 4.6: Frequency shift versus $\sin\theta_i$ for 54% (a), 59% (b), 70% (c) and 72% (d) single porous layer. The letters on the right hand side indicate the origin of the phonons. R – surface Rayleigh, S_i – unknown, QT – quasi-transverse, QL – quasi-longitudinal.

[14] cubic anisotropy of the layers is expected. The plots of angular dependencies of the bulk phonon velocities for each sample are shown in Figs. 4.7(a)–(d) and Figs. 4.8(a)–(d). Fitting Eqs. (2.44) and (2.45) to the data points for v_- and v_+, respectively, allows determination of the values of the elastic constants of the p-Si single layers. The weighting of the data points was inversely proportional to the square of the uncertainty associated with it. Taking into consideration reports on birefringence [151] showing evidence that p-Si structure is more anisotropic, data presented in Figs. 4.7(a)–(d) and Figs. 4.8(a)–(d) were fitted into Eqs (2.53) and (2.54). No improvement of the fit was observed. Additionally, the values of c_{11} and c_{33} agreed within uncertainty, suggesting cubic symmetry of the layers.

There is a weak dependence of the phonon frequency shift on the incident angle which should not be observed in the case of the pure transverse phonon (see Eq. (2.43)) [101]. In any event, the fitting procedure gave slightly more precise results for quasi-transverse phonon comparing to that of pure shear character. That could be related to the fact that fixing one of the elastic constants (c_{44}) limits the range within which the other two constants, c_{11} and c_{12} could vary. There is no obvious reason why the character of the phonon of smaller frequency shift was assumed to be quasi-transverse versus pure transverse other than the arguments presented above. It is worth mentioning, however, that the values of transverse phonon velocities are almost degenerate for propagation directions close to normal to the surface, especially within the uncertainty associated with the velocities and for the small angle of

incidence (see Eq. (2.43) and (2.44)).

4.3 Elastic Constants

The initial guesses of values of longitudinal and transverse elastic constants, c_{11} and c_{44} come from the calculation using velocity determined from the spectra collected at the smallest θ_i. The range within which the elastic constants were allowed to vary was at first determined by the uncertainties in the acoustic velocity. None of the constants reached either of the limits during initial fitting therefore the narrowing down of the possible values turned out to be unnecessary. During the fitting, the only constraints placed on the elastic constants were those of elastic stability for cubic materials: $c_{44} > 0$, $c_{11} > |c_{12}|$ and $c_{11} + 2c_{12} > 0$ [110]. The obtained values of elastic constants together with calculated Young's moduli and anisotropy ratios are tabulated in Table 4.5. Young's modulus along the [001] direction for a cubic material is calculated according to $Y = c_{11} - \frac{2c_{12}^2}{c_{11}+c_{12}}$ and the anisotropy ratios are calculated using Eq. (2.46).

In general, the anisotropy ratio $\alpha \approx 1$ for nearly all samples suggesting the anisotropy of the p-Si film is very small or even negligible. The relative uncertainties, however, are large, especially for the layers of lower porosity. In the case of the sample with 33% porosity, although the value of α seems reasonable, it has to be noted that the value of c_{11} is slightly smaller than that observed for the sample with the next lowest porosity. Additionally, the value of c_{12} carries an uncertainty that exceeds the

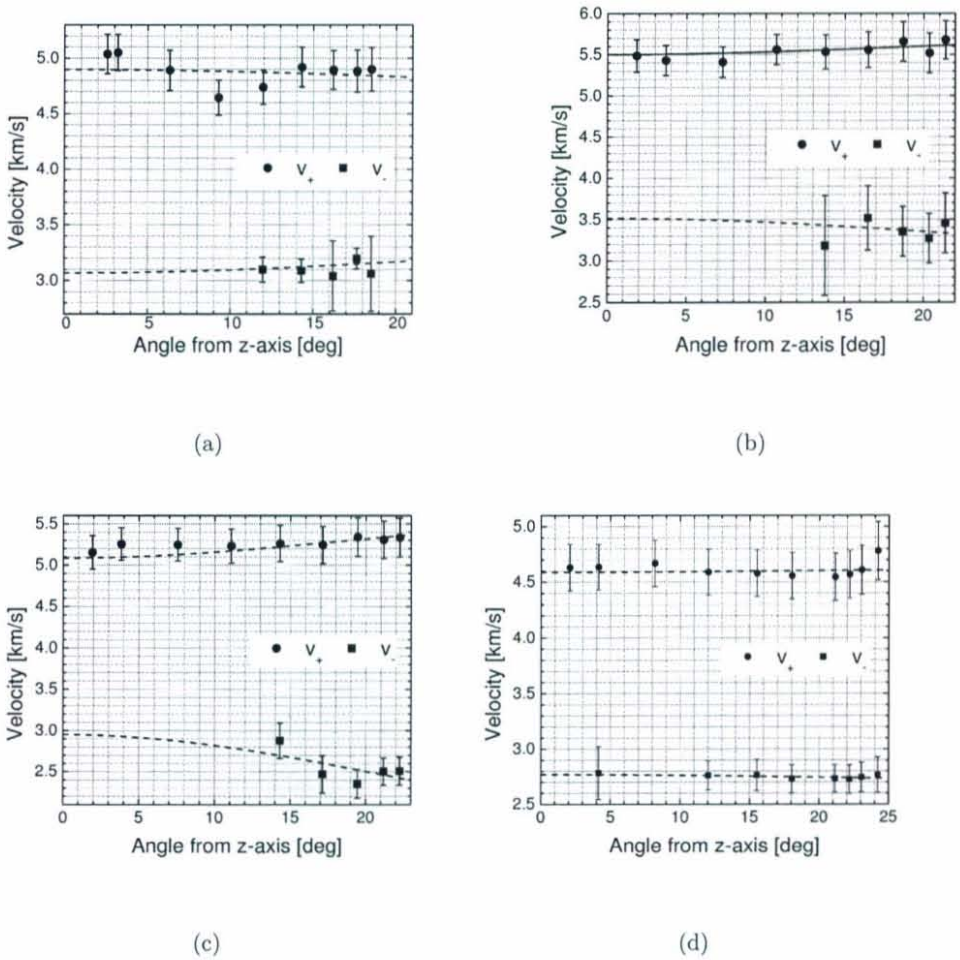

Figure 4.7: Bulk phonon velocities versus angle from z-axis for 33% (a), 44% (b), 48% (c) and 52% (d) single porous layer.

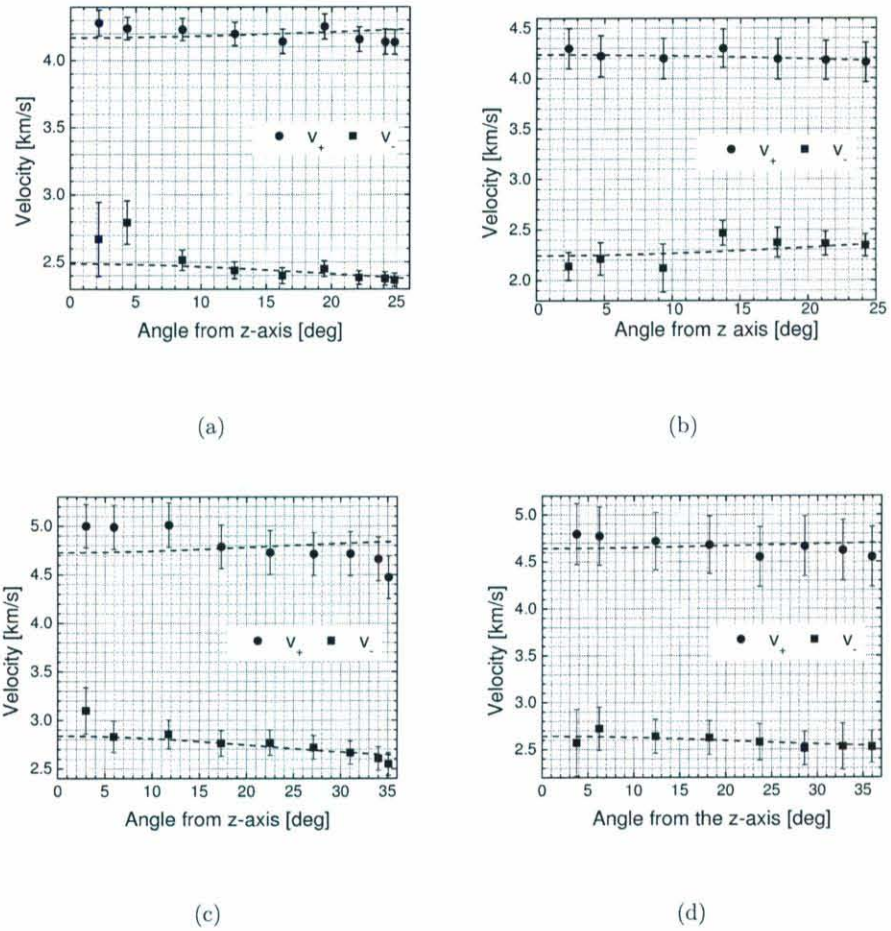

Figure 4.8: Bulk phonon velocities versus angle from z-axis for 54% (a), 59% (b), 70% (c) and 72% (d) single porous layer.

Table 4.5: Elastic constants, Young's moduli and anisotropy ratios of the single p-Si layers determined for cubic symmetry of the material.

Porosity	Elastic Constants			Young's Modulus	Anisotropy Ratio
ξ [%]	c_{11} [GPa]	c_{12} [GPa]	c_{44} [GPa]	Y [GPa]	α
33 ± 2	37 ± 1	3 ± 5	16.7 ± 0.9	37	1.0±0.3
44 ± 2	39 ± 2	14 ± 3	16 ± 2	32	1.3±0.6
48 ± 3	31 ± 2	23 ± 2	10 ± 2	5	3±1
52 ± 3	23 ± 1	7 ± 2	8.4 ± 0.8	20	1.1±0.2
54 ± 1	18.6 ± 0.3	7.2 ± 0.5	6.6 ± 0.3	14	1.2±0.2
59 ± 2	17.4 ± 0.3	7 ± 1	4.6 ± 0.3	13	0.9±0.3
70 ± 2	15.6 ± 0.6	6.0 ± 0.6	5.6 ± 0.4	14	1.2±0.3
72 ± 3	14.0 ± 0.2	5.7 ± 0.3	4.5 ± 0.1	11	1.1±0.1

value itself. This is attributed to the experimental error associated with determination of the frequency shifts of the peaks due to the bulk phonons propagating in the 33% porous films. It could also be related to the determination of the porosity of these samples as the small mass loss could cause additional inaccuracy.

Two samples that require additional commentary are those of 44% and 48% porosity. For the first one the relative uncertainty in α is almost half of the value of the anisotropy ratio. In the case of the 48% porous layer the anisotropy ratio appears to be three times greater than that calculated for any other p-Si film. This is an unexplained anomaly, as there is no reason to believe that there is anything special about this sample.

A plot of transverse and longitudinal elastic constants versus porosity of the film is shown in Fig. 4.9. It can be noted that values of c_{11} and c_{44} of the 33% porous layer do not lie on the best fit curve. This can be attributed to a systematic uncertainty

resulting from poor quality of the spectra collected from this sample. The relationship between the constants and the porosity can be characterized by the equation [65]

$$c_{ij} = c_{ij}^{c-Si}(1-\xi)^{\gamma_{ij}}, \tag{4.1}$$

where ij=11 and 44 and the values of the elastic constants for c-Si are 166 GPa for c_{11} and 79 GPa for c_{44} [152]. The corresponding equations for the data of the present study presented in the plot (dashed line) are

$$c_{11} = 166(1-\xi)^{2.8}, \tag{4.2a}$$

$$c_{44} = 79(1-\xi)^{3.2}. \tag{4.2b}$$

The porosity dependence of the values of elastic constant c_{12} (right-hand axis) is also shown in Fig. 4.9. For low porosity samples the values of c_{12} are scattered. For high porosity samples the decrease of the value with the increase of the porosity can be noticed.

All the elastic constants values obtained in this work are more than an order of magnitude lower than those reported by Matthai *et al.* [154] (c_{11} = 94 GPa and c_{12} = 34 GPa). The elastic constants were calculated for a cubic symmetry of the p-Si layer for modified diffusion limited model created to simulate the 75% porous structure. It is possible that the discrepancies in the values of the elastic constants are related to the differences in the morphology of the films modeled in the work of Matthai and those examined in this study. It could also be caused by the fact that

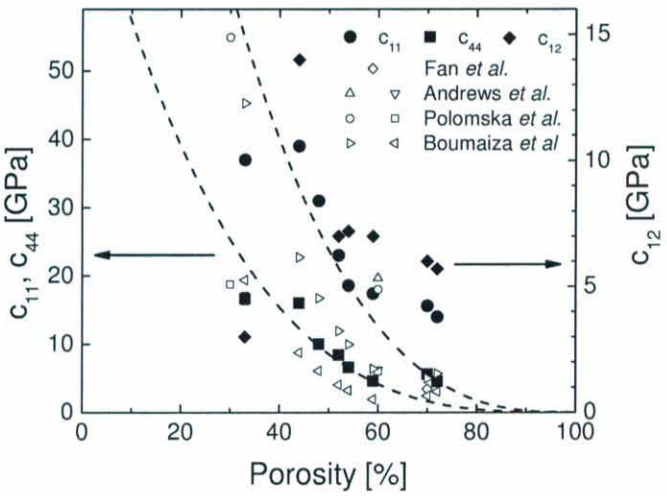

Figure 4.9: Elastic constants of the p-Si single layers as a function of porosity. Left-hand side scale shows values of c_{11} (• – present work, ◇ – [70], △ – [72], ○ – [95],▷ – [153]) and c_{44} (■ – present work, ◇ – [70], ▽ – [72], □ – [95], ◁ – [153]) for all data. Right-hand side scale shows the values of c_{12} obtained in the present study (♦). Dashed line shows the best fit curve to the values of c_{11} and c_{44} presented in this work.

it is not entirely clear whether the elastic constants referred to as c_{11} and c_{12} are the same as those determined in this work.

The work of Boumaiza *et al.* [153] suggest that the porosity dependence of velocities, impedances and elastic constants (X) of p-Si layers can be described using the expression $X = X_0(1 - \gamma_1\xi + \gamma_2\xi^2)$, where X_0 represents the appropriate value for c-Si, ξ is layer porosity and γ_i are parameters determined empirically. All the samples examined were of porosity lower than 50%. The values of c_{11} and c_{44} obtained using the suggested parameters ($\gamma_1 = 0.77$, $\gamma_2 = -0.73$ for c_{11} and $\gamma_1 = 1.1$, $\gamma_2 = -0.33$

for c_{44}) are shown in Fig. 4.9. The values of elastic constants decrease faster with increasing porosity than those obtained in this work.

Fan *et al.* [70] reported values of elastic constants c_{11} and c_{12} for isotropic, 70% porous Si film. These values (3.4 GPa and 1.3 GPa) are almost three times lower than those obtained from our samples. The direct comparison cannot be made as most of the work done by Fan is with the p^- type Si but the trend is in agreement with reports by Andrews *et al.* [73], that the elastic constants of p^- samples are significantly lower than those of p^+ at the same porosity. There is agreement, however, between the present work and that of Andrews *et al.* for p^+ samples [72].

The values of c_{11} and c_{44} reported by Polomska *et al.* [95] for 30% and 60% porous films made from identical parent wafers but using a solution of 1 49% HF, 1 C_2H_5OH and 1 nanopure H_2O, were calculated assuming isotropy of p-Si layers. The agreement with values reported in this work is good, especially for the higher porosity layer. This result is understandable considering the fact that the anisotropy ratios of samples examined in this work are close to unity. For the 30% porous samples, as expected, the reported values are larger. It is also mentioned that the quality of the spectra collected from the samples of lower porosity was poor.

The porosity dependence of Young's modulus calculated for the [001] direction in a cubic material is presented in Fig. 4.10. The value of Young's modulus for c-Si along the [001] direction is 130 GPa [155] and the equivalent of the Eq. (4.1) is fitted to the data, resulting in the value of γ_Y=2.8±0.2. With the exception of the

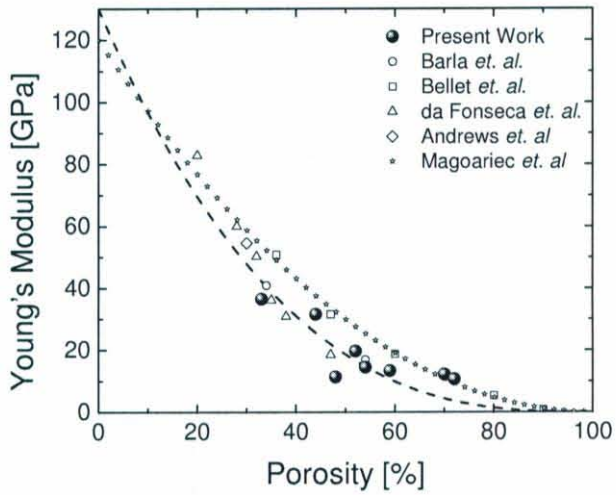

Figure 4.10: Young's modulus of the p-Si single layers as a function of porosity ($\circledast$ – present work, $\triangle$ – [65], $\diamond$ – [67], $\star$ – [116], $\circ$, $\square$ – [28]). The dashed line presents the best fit curve to the values of Y obtained in present work.

datum for the 48% porous sample, Young's modulus decreases monotonically with increasing porosity. The problem with the value of Y obtained for this particular layer is related to the high anisotropy that was obtained for the film. The unexpected lack of agreement with other values suggests that the anisotropy is not real but rather could be related to the frequency shifts of the wide Brillouin peaks observed for the spectra collected from this layer.

Magoariec [116] presented a model predicting the elastic properties of nano-p-Si, obtaining the theoretical value of the parameter γ_Y=2 with Y_{c-Si}=120 GPa. Adjusting the value of Young's modulus for c-Si to the value used by these authors brings γ_Y obtained in this work down to 2.6. The reason behind the lack of agreement is

most likely related to the limitations of the model (it takes only nearest and next nearest neighbours into consideration and representative volume elements are of fixed size. It could also be related to the morphology of the p-Si films as p^+ samples are characterized by larger pore size than p^- for which the model was developed. The authors also conclude that, according to the model, for porosities close to 30% p-Si can be approximated as an isotropic material.

Bellet *et al.* [28] reports values of Young's modulus obtained via nanoindentation for p^+ and p^- samples. The same report recalls results obtained by Barla *et. al* using X-ray diffraction technique. All the results regarding p^+ layers are included in Fig. 4.10 and are in agreement with those presented in this work, especially in the region of higher porosities.

Knowledge of elastic constants of the p-Si layer allows determination of the velocities of the transverse and longitudinal acoustic phonons propagating along the [001] direction. These velocities are calculated using the values of c_{44} and c_{11} elastic constants, respectively. The values of all the velocities, including previously calculated velocities of surface modes are tabulated in Table 4.6.

The experimental results of surface, transverse and longitudinal phonon velocities are shown as a function of porosity of the p-Si film in Fig. 4.11. This figure also includes the value of the transverse and longitudinal phonon velocities of c-Si (5.82 km/s and 8.44 km/s [152], respectively). From Table 4.6 and Fig. 4.11 it can be seen that the surface, transverse and longitudinal velocities show overall decrease

Table 4.6: Surface and bulk phonon velocities of the single p-Si layers. The values of bulk phonon velocities are calculated for the [001] direction of propagation using elastic constants obtained during the fit.

Porosity	Phonon Velocity		
ξ	v_R	v_T	v_L
[%]	[km/s]	[km/s]	[km/s]
33 ± 2	3.02±0.03	3.27±0.09	4.87±0.04
44 ± 2	2.97±0.02	3.51±0.06	5.48±0.09
48 ± 2	3.16±0.01	2.88±0.07	5.06±0.09
52 ± 3	2.53±0.01	2.8±0.1	4.6±0.1
54 ± 1	2.18±0.03	2.5±0.1	4.17 ±0.02
59 ± 2	2.47±0.05	2.2±0.1	4.26±0.04
70 ± 2	2.10±0.03	2.8±0.1	4.72±0.05
72 ± 3	2.08±0.02	2.63±0.03	4.64±0.02

with increasing porosity. The velocity of the phonons may be related to the porosity according to da Fonseca's equation [65]. It has the general form

$$v_{R,T,L} = v_{R,T,L}^{c-Si}(1-\xi)^{\gamma_{R,T,L}}, \tag{4.3}$$

where $v_{R,T,L}$ is the phonon velocity of the p-Si layer, $v_{R,T,L}^{c-Si}$ is the equivalent phonon velocity of the c-Si, ξ is the porosity and $\gamma_{R,T,L}$ is an empirical parameter evaluated by numerical analysis software. The values of γ_L and γ_T are 0.73 ± 0.07 and 0.9 ± 0.1, respectively. These values should be related to those of γ_{ij} via equations $\gamma_{11}=2\gamma_L+1$ and $\gamma_{44}=2\gamma_T+1$ [66]. In our case the empirical exponents, calculated from the values of $\gamma_{T,L}$ are equal to 2.8±0.2 and 2.5±0.1, respectively. Within uncertainties these values agree with those in Eq. (4.2).

Da Fonseca *at al.* [65], [66] presented values of surface and transverse phonon velocities as well as values of the empirical parameters $\gamma_{R,L}$. The experiments were carried out for p^+ p-Si layers ranging in porosity from 20% to 50% with the as-

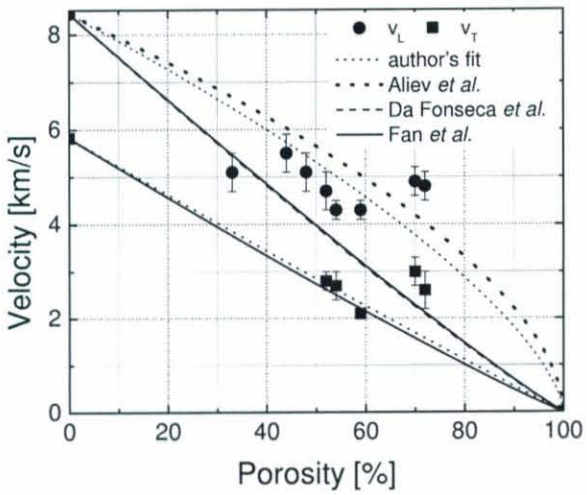

Figure 4.11: Transverse (■) and longitudinal (• – present work) phonon velocities of the p-Si single layers as a function of porosity. The thin dotted line is the best fit curve to data presented in this work, dashed line is the best fit curve proposed by Da Fonseca *et al.* [65,66], solid line is the best fit curve presented by Fan *et al.* [70] and thick dotted line is best fit curve proposed by Aliev *et al.* [74].

sumption of elastic isotropy. The longitudinal phonon velocities of the present study are higher than those obtained by da Fonseca. The empirical parameter γ_L=1.095 obtained by these authors does not agree with that presented in this work. It is, however, in agreement with that reported by Fan *et al.* [70] (γ_L=1.086). The values of surface Rayleigh and bulk longitudinal velocities are used by da Fonseca to obtain the velocities of the transverse acoustic phonon using Viktorov's relation [156]. As can be seen in Fig. 4.11 the values of transverse phonon velocities are very similar to those presented in this work. The similarity is confirmed by the value of γ_T=1.185, which is slightly higher. The value of γ_T obtained by Fan *et al.* (γ_T=1.083) shows even better

agreement with the value of this empirical parameter for transverse phonon velocities presented in this work.

The discrepancies in the values of the empirical parameter γ_L could be caused by the difference in resistivity of the silicon samples, especially in case of the data obtained from samples of a wide range of resistivities (between 5 and 184 mΩ·cm) reported by Fan. Particularly interesting is that the results of da Fonseca's work, done mostly on p^+ samples, roughly agree with those of the present work in the case of transverse velocities (1.185 versus 0.9, respectively) while lacking a correlation for longitudinal phonon velocities (1.095 versus 0.73, respectively). The difference could be associated with the order of the p-Si structure affecting phonon polarized along the direction of propagation. It could also be related to the fact, that although within uncertainty the anisotropy ratio is equal to unity (see Table 4.5), the actual value may differ from it, making Viktorov's relation used by da Fonseca invalid for samples examined in this work and agreement for the values of γ_T coincidental. No other explanation can be provided, especially taking into consideration the comparisons made between the elastic constants and Young's moduli calculated for the p-Si layers presented above.

The work done by Lockwood *et al.* [69] estimates the ranges of empirical parameters based on the Brillouin frequency shifts obtained from the high-porosity samples and the mode assignment to be $\gamma_T \leq 0.84$ and $\gamma_L \geq 0.72$. These values agree within uncertainty with the values of the empirical parameters presented in this work. The

correction of the mode assignment provided later [70] should not significantly affect the limits of the estimated ranges. The only correction regarded the peak initially assigned as originating due to the longitudinal guided mode (LGM) and later assigned as due to longitudinal acoustic mode. As $v_L < v_{LGM}$, regarding the Eq. 4.3, the value of γ_L would become equal to 0.72.

The value of γ_L is in reasonable agreement with the value of 0.58 determined by Aliev *et al.* [74] for samples of resistivity 10-15 mΩ·cm, which are comparable to those of the present work. According to these authors, the low value of the γ_L suggests well-ordered structure of the p-Si layer.

Discrepancies between the work done by the author and that presented in all the reports referenced above could also be related to the morphology and geometry of the pores characterizing the samples. These factors depend on the resistivity and therefore the doping level of the c-Si wafers. As shown by Andrews *et al.* [73] they influence the acoustic phonon velocities, changing them and, consequently, the elastic stiffness constants.

The results obtained for the single layer films contained in this chapter were used in further production and analysis of p-Si superlattices. Proper and thorough characterization of the single p-Si layers is crucial as the constituent layers of the superlattices will be fabricated under conditions identical to those used to fabricate the single layers. The elastic properties of the single layers are also used as input to obtain modeled values of the effective elastic constants.

Chapter 5

Porous Silicon Superlattices

The constituent layers of multilayered structures with period Λ at least an order of magnitude smaller than the wavelength of the acoustic phonon propagating through the structure ($\sim$100 nm) were fabricated under identical experimental conditions as p-Si single layer films characterized in Chapter 4. As mentioned in Section 3.1 and shown in Table 3.2, all porous silicon superlattices were obtained by alternating the electric current between two values as a function of time. The etch times for each current were chosen so that the constituent layers are approximately 10 nm thick and the number of cycles (250) was picked to obtain films with a thickness of a few μm. One of the layers was kept the same through the set of examined superlattices while the other was different for each sample. Each period of the superlattice consists therefore of one layer of 59% porosity (referred from here on as the "permanent" layer) and one layer of porosity characterized in Chapter 4 (referred to as the "variable" layer).

The reason behind keeping one layer identical in all samples was to observe the change in the elastic constants and make comparison with the Grimsditch-Nizzoli model for the largest possible range of porosities while having a common factor for all the samples. It was also of interest to observe the behaviour of surface modes when the top layer (permanent one) is respectively of higher and lower porosity than the average. The choice of 59% porous layer over any other is justified by the fact that during the preliminary experiments, when only two single layers with ~30% and ~60% porosity were investigated, the spectra collected from the latter one were of much better quality and hence provided frequency shifts and phonon velocities carrying much smaller experimental uncertainty.

5.1 Brillouin Spectra

As in the case of single layer p-Si films, a set of spectra with incident angles ranging from $\sim 5^o$ to $\sim 75^o$ was collected for each superlattice. All spectra were collected in air, with normal pressure and room temperature and are presented in Figs. 5.1(a)–(c) and 5.2(a)–(d).

Similar to the single layer films, the quality of the spectra increased with increasing average porosity of the superlattice. Based on the features observed in the spectra, the samples can be divided into two groups - one with the variable layer of porosity lower than 50% and one with variable layer with porosity higher than 50%. The sharp, well defined peak labeled R, located closest to the peak due to elastically scattered light

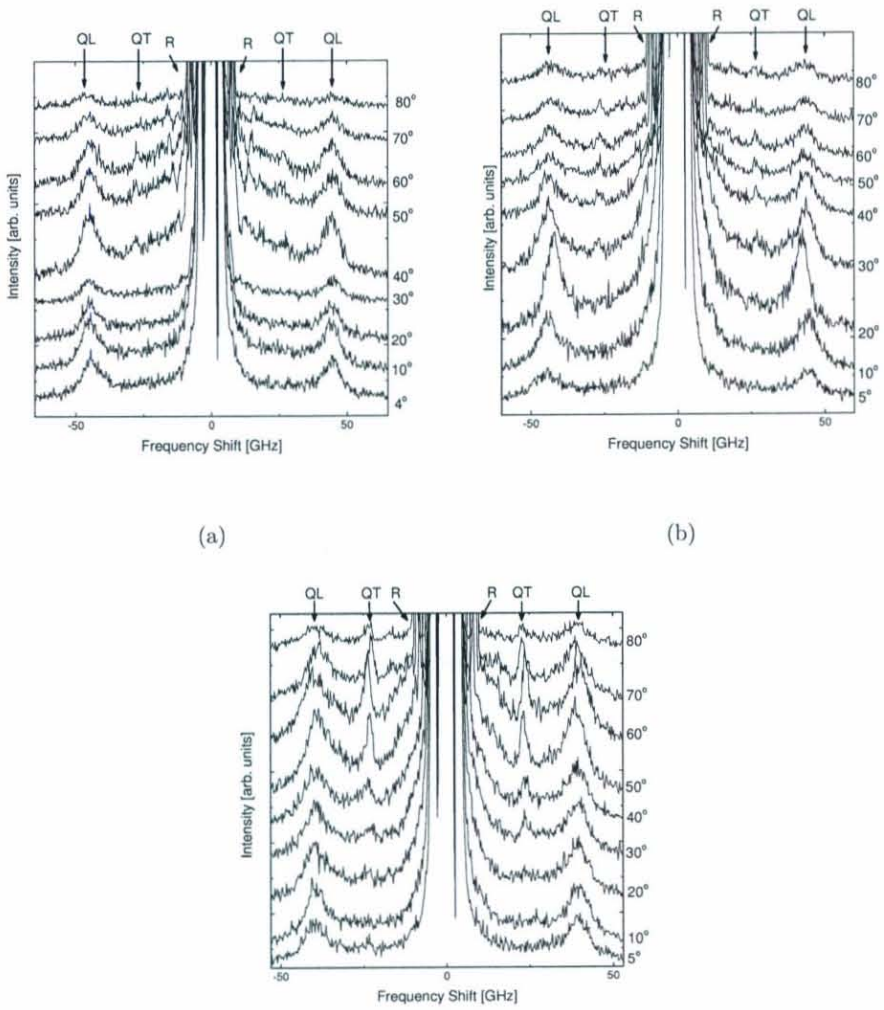

(a)

(b)

(c)

Figure 5.1: Brillouin spectra from p-Si superlattices with 59%-33% (a), 59-44% (b) and 59-48% (c) porous constituent layers. The symbols above (R, QT, QL) the diagrams indicate the phonons due to which peaks originate (surface Rayleigh, quasi-transverse and quasi longitudinal, respectively). The labels to the right indicate the incidence angle measured from the normal to the sample in the air.

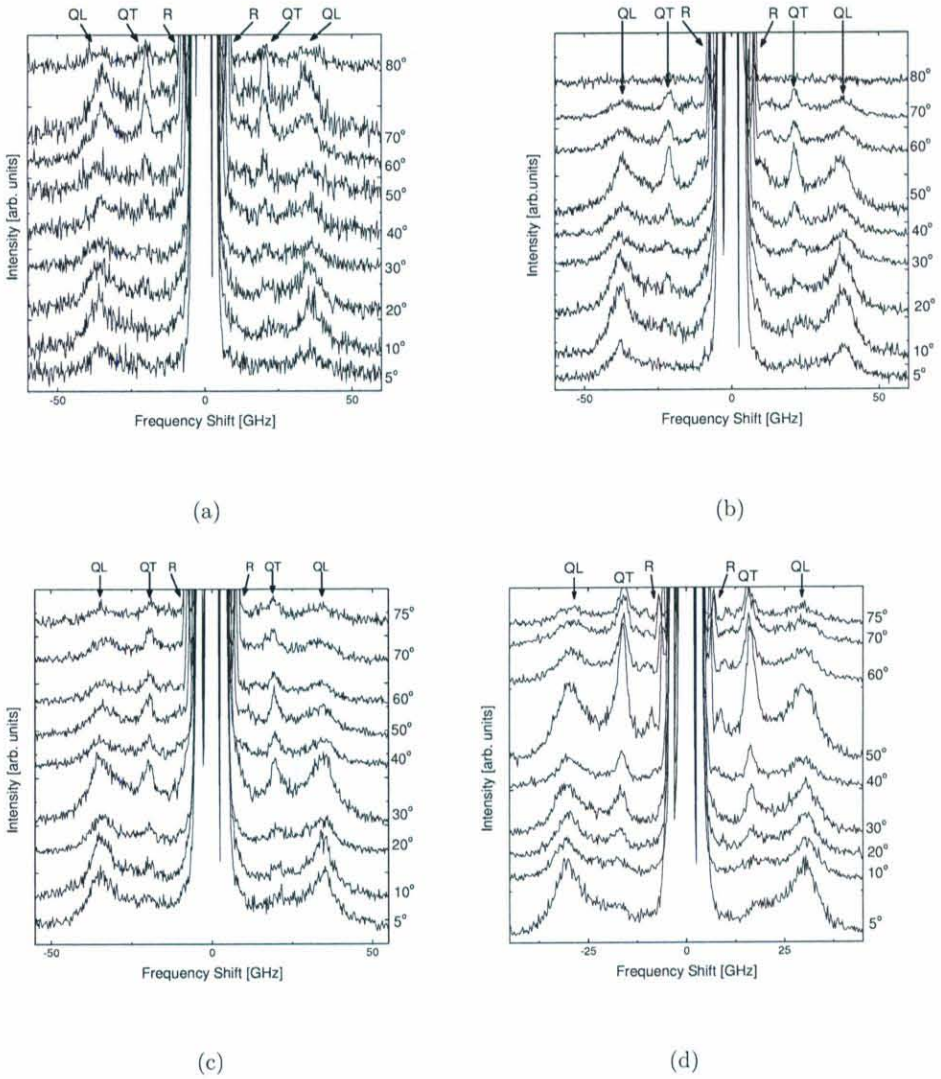

Figure 5.2: Brillouin spectra from p-Si superlattices with 59%-52% (a), 59-54% (b), 59-70% (c) and 59-72% (d) porous constituent layers. The symbols above (R, QT, QL) the diagrams indicate the phonons due to which peaks originate (surface Rayleigh, quasi-transverse and quasi longitudinal, respectively). The labels to the right indicate the incidence angle measured from the normal to the sample in the air.

(of a frequency shift of 0 GHz) of all the observed peaks, showed a linear dependence on the sine of the incident angle and therefore was assigned as originating due to the Rayleigh surface phonon propagating along the free surface. The assignment is additionally supported by the fact that the velocity of this phonon calculated later was the smallest of the velocities of all identified phonons. The other two modes were identified as due to quasi-transverse (QT) and quasi-longitudinal (QL) bulk phonons. The assignment is based on the same grounds as for the p-Si single layers (weak dependence of the frequency shift on the incidence angle and no peaks observed for frequencies larger than those attributed to the QL mode). The mode assignment is indicated by labels placed above the topmost spectrum in each of Fig. 5.1(a)–(c) and 5.2(a)–(d).

5.2 Frequency Shifts and Phonon Velocities

All peaks were fitted using a Lorentzian function and their frequency shifts and uncertainties, together with values of bulk phonon velocities along each direction are presented in Tables 5.1-5.3.

The quasi-transverse mode is not apparent in the spectra collected at incident angles lower than 40^o from samples with a variable layer of lower porosity. In addition, well defined, narrow peaks, situated at frequency shifts between R and QT modes were observed in spectra collected at higher incident angles. Two peaks were resolved in this frequency region in samples consisting of a permanent layer with those of

Table 5.1: Frequency shifts of p-Si superlattices 2.14#2 (59%–33%),2.14#1 (59%–44%) and 2.14#3 (59%–48%).

Sample	θ_i	θ_i'	Frequency Shift					Phonon Velocity	
			R	S_1	S_2	QT	QL	v_-	v_+
	[deg]	[deg]	[GHz]	[GHz]	[GHz]	[GHz]	[GHz]	[km/s]	[km/s]
2.14#2	4	1	—	—	—	—	—	44.3±0.1	4.3±0.1
	10	4	—	—	—	—	—	44.4±0.1	4.3±0.1
	20	7	—	—	—	28±2	44.4±0.1	2.1±0.3	4.3±0.1
	30	10	—	6.89±0.05	10.5± 0.1	26.6±0.8	44.39	2.6±0.2	4.3±0.1
	40	13	6.122	8.5	12.8±0.3	27±1	44.2±0.1	2.6±0.2	4.3±0.1
	50	16	7.11±0.01	9.32±0.05	14.07±0.05	25.9±0.8	44.5±0.1	2.5±0.2	4.0±0.1
	60	18	7.70± 0.01	—	—	25.6±0.8	44.2±0.2	2.5±0.2	4.3±0.1
	70	20	8.07±0.01	—	—	27±1	2.6±0.2	44.8± 0.2	4.3±0.1
	80	21	8.32±0.01	15.1±0.5	—	26±1	45.6±0.4	2.5±0.2	4.4±0.2
2.14#1	5	2	—	—	—	—	43.5±0.2	—	4.7±0.1
	10	4	—	—	—	—	43.2±0.2	—	4.6±0.2
	20	8	—	—	—	—	42.20±0.06	—	4.5±0.2
	30	12	—	—	—	27.4±0.4	43.1	2.9±0.1	4.6±0.2
	40	15	6.497	10.0±0.2	12.8±0.6	25±3	43.8±0.2	2.7±0.4	4.7±0.2
	50	18	7.850	10.8±0.1	14.4±0.3	26±1	43.3±0.3	2.8±0.21	4.6±0.2
	60	20	8.747	12.5±0.2	16.7±0.4	26.5±0.4	42.9±0.3	2.8±0.1	4.6±0.2
	70	22	9.284	12.4±0.1	16.1± 0.4	26.4±0.4	42.9±0.3	2.8±0.1	4.6±0.2
	80	23	9.586	13.7±0.2	18.6±0.3	26.1±0.4	42.8±0.3	2.8±0.1	4.6±0.2
2.14#3	5	2	—	—	—	—	39.8±0.1	—	4.6±0.2
	10	4	—	—	—	—	39.7± 0.1	—	4.6±0.2
	20	9	—	—	—	—	39.6±0.2	—	4.6±.2
	30	13	—	—	—	24.0± 0.4	39.3±0.1	2.8±0.2	4.5±0.2
	40	16	6.20±0.01	10.0±0.2	13±1	24.1±0.4	39.0±0.3	2.8±0.2	4.5±0.2
	50	19	7.29±0.01	10.3±0.1	13.7±0.4	23.3±0.1	38.2±0.2	2.7±0.1	4.4±0.2
	60	22	8.17±0.01	11.5±0.1	14.8±0.4	23.9±0.1	39.0±0.2	2.8±0.1	4.5±0.2
	70	24	8.75±0.01	11.9±0.3	15.6±0.3	22.9±0.1	38.0±0.2	2.7±0.1	4.4±0.2
	80	25	9.12±0.01	12.3±0.2	16.0±0.3	23.30±0.07	39.0±0.1	2.7±0.1	4.5±0.2

Table 5.2: Frequency shifts of sample 2.14#4 (59%–52%) and 2.18#2 (59%–54%).

Sample	θ_i	θ_i'	Frequency Shift				Phonon Velocity	
			R	S_1	QT	QL	v_-	v_+
	[deg]	[deg]	[GHz]	[GHz]	[GHz]	[GHz]	[km/s]	[km/s]
2.14#4	5	2	—	—	21±1	35.4±0.4	2.5±0.2	4.2±0.2
	10	4	—	—	23±1	36.2±0.2	2.8±0.2	4.3±0.2
	20	9	—	—	20.8±0.5	35.6±0.2	2.5±152.7	4.2±0.2
	30	13	—	—	20.4±0.4	35.3±0.3	2.4±140.7	4.2±0.2
	40	17	5.81±0.01	10.5±0.4	20.1±0.3	33.6±0.5	2.4±0.1	4.0±0.2
	50	20	6.77±0.01	12.3±0.5	20.1±0.2	34.9± 0.5	2.4±109.0	4.2±0.2
	60	23	7.51±0.01	12.6±0.2	20.2±0.1	33.9±0.2	2.4±100.2	4.0±0.2
	70	25	7.94±0.01	—	19.2±0.2	34.5±0.2	2.3±0.1	4.1±0.2
	80	26	8.16±0.02	—	19.9±0.3	35.7±0.4	2.4±0.1	4.3±0.2
2.18#2	5	2	—	—	24±1	38.0±0.1	2.9±0.2	4.5±0.2
	10	5	—	—	22.4±0.5	37.8±0.1	2.7±0.2	4.6±0.2
	20	9	—	—	21.9±0.4	37.5±0.1	2.7±0.1	4.6±0.2
	30	13	—	—	21.9±0.3	37.8±0.1	2.7±0.1	4.6±0.2
	40	17	5.70±0.01	9.8±0.2	21.5±0.2	36.6±0.2	2.6±0.1	4.4±0.2
	50	20	6.76±0.01	11.3±0.2	21.4±0.1	36.2±0.1	2.6±0.1	4.4±0.2
	60	23	7.52±0.01	12.4±0.2	21.5±0.1	36.7± 0.2	2.6±0.1	4.5±0.2
	70	25	8.06±0.01	13.3±0.2	21.4±0.1	36.5±0.2	2.6±0.1	4.4±0.2

Table 5.3: Frequency shifts of sample 2.18#4 (59%–70%) and 2.17A#10 (59%–72%).

Sample	θ_i	θ_i'	Frequency Shift				Phonon Velocity	
			R	S_1	QT	QL	v_-	v_+
	[deg]	[deg]	[GHz]	[GHz]	[GHz]	[GHz]	[km/s]	[km/s]
2.18#4	5	3	—	—	20.7±0.7	34.8±0.1	2.9±0.2	4.9±0.2
	10	5	—	—	19.9±0.7	34.47±0.08	2.8±0.2	4.9±0.2
	20	11	—	—	19.9±0.3	34.2±0.1	2.8±0.2	4.9±0.2
	30	16	—	—	19.4±0.3	34.2±0.1	2.8±0.1	4.9±0.2
	40	20	5.66±0.01	9.8±0.3	19.7±0.2	33.9±0.2	2.8±0.1	4.8±0.2
	50	24	6.52±0.01	11.1±0.2	19.68±0.08	33.3±0.2	2.8±0.1	4.7±0.2
	60	28	7.35±0.01	13.1±0.2	19.5±0.1	33.0±0.2	2.7±0.1	4.7±0.2
	70	30	7.94±0.01	12.8±0.3	18.9±0.2	32.9±0.3	2.7±0.1	4.7±0.2
2.17A#10	5	3	—	—	—	30.41± 0.08	—	4.5±0.3
	10	6	—	—	—	30.71± 0.09	—	4.5±0.3
	20	11	—	—	17.4±0.2	30.05± 0.08	2.6±0.2	4.4±0.3
	30	16	—	—	16.80±0.09	30.00± 0.09	2.5±0.2	4.4±0.3
	40	21	—	—	16.45±0.05	29.3± 0.1	2.4±0.1	4.3±0.3
	50	25	5.80±0.02	9.1±0.1	16.±0.04	29.14± 0.1	2.4±0.1	4.3±0.3
	60	29	6.42±0.02	—	16.06±0.03	29.7± 0.1	2.40.1	4.4±0.3
	70	31	6.93±0.01	—	16.02±0.04	29.08± 0.2	2.40.1	4.3±0.3
	75	32	7.04±0.03	10.4±0.1	15.84±0.06	28.7± 0.2	2.3±0.1	4.2±0.3

porosity lower than 50% and one in samples with variable layer of porosity higher than 50%. These peaks showed linear dependence on the sine of the incident angle (see Figs. 5.3(a)–(c) and 5.4(a)–(d)). The origin of these peaks is not clear. The first order modes could originate due to Lamb modes, connected the existence of stress-free surface [131] as their velocities fall within the range between v_T and v_L. For the semi-infinite medium, which the SL is suppose to represent, those modes coincide with surface Rayleigh phonon [137]. The origin due to the Love waves is also excluded as additionally to the fact that the p-Si layer is semi-infinite, the velocity of the transverse bulk phonon propagating in the SL of any average porosity is smaller than that of c-Si substrates [131], [137]. They cannot be classified as due to Stoneley waves that appear on the interfaces between different elastic media. In the case of SL the layer thickness is larger than the penetration depth of the incident light. The only reasonable guess is that the peaks could originate due to pseudo-surface modes observed when the surface of the medium is anisotropic [157]. As the symmetry of the SLs combines those of constituent layers, it is possible that the observed modes are related to the existence of anisotropic surface. For simplicity these modes are labeled S_i and, from now on, are referred to in this chapter as "pseudo-surface" modes although their actual origin is not certain.

In some respects, however, these peaks resemble features observed by Dutcher *et al.* [158] for thin metallic superlattice films with a total thickness of $\sim$0.5 μm which is about an order of magnitude lower than the SLs studied in this work. Thin, sharp

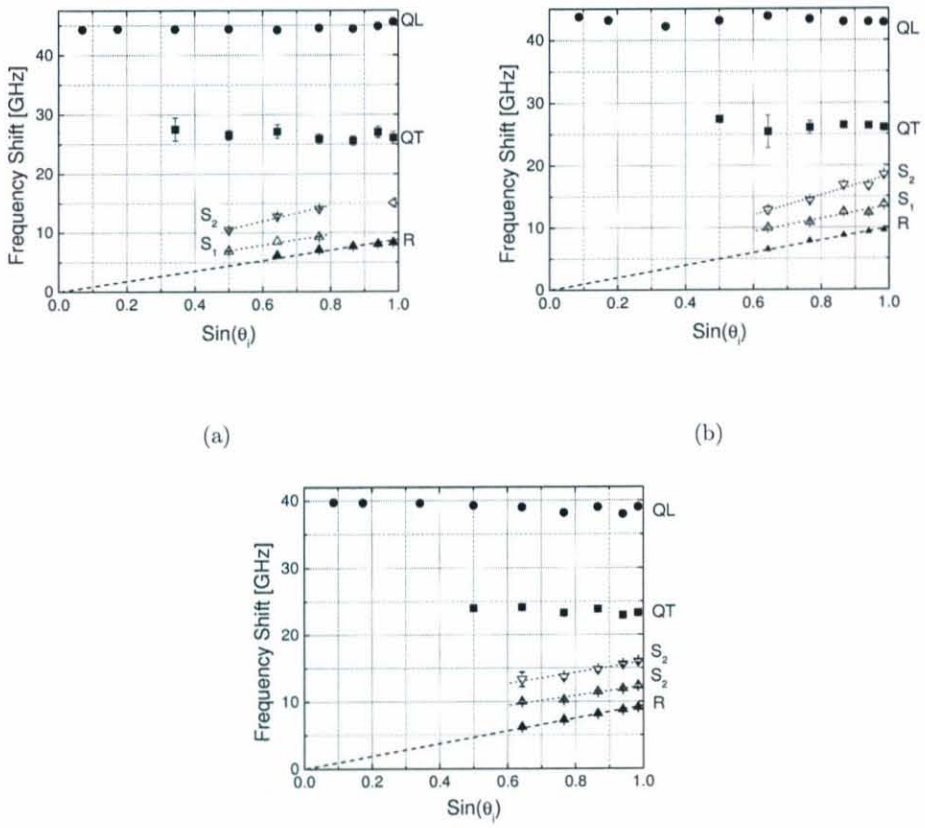

Figure 5.3: Frequency shift versus $\sin\theta_i$ for p-Si superlattices with 59%-33% (a), 59-44% (b) and 59-48% (c) porous constituent layers. The letters on the right hand side denote the origin of the phonons. R – surface Rayleigh, S_i – pseudo-surface, QT – quasi-transverse, QL – quasi-longitudinal.

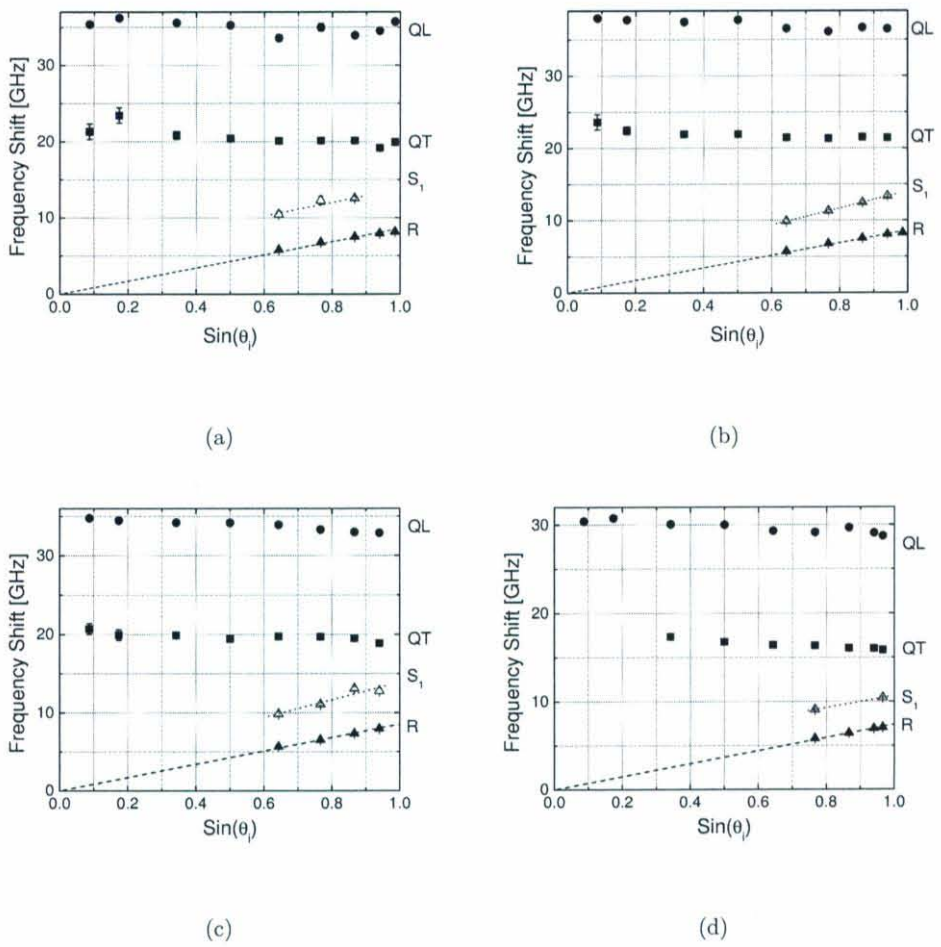

Figure 5.4: Frequency shift versus $\sin\theta_i$ for p-Si superlattices with 59%-52% (a), 59-54% (b), 59-70% (c) and 59-72% (d) porous constituent layers. The letters on the right hand side denote the origin of the phonons. R – surface Rayleigh, S_i – pseudo-surface, QT – quasi-transverse, QL – quasi-longitudinal.

and well defined peaks were also observed by Carlotti *et al.* [159] for transparent ZnO film of hexagonal symmetry. Both authors associate this peak with the "leaky" longitudinal mode (in Dutcher's work they are identified as originating due to longitudinal guided modes) with velocities that depend on the angle of incidence and strongly on elastic constant c_{11}. The problem with direct comparison is that, despite similarities in the lineshape, the spectra described in [158] and [159] were obtained from SL that are an order of magnitude thinner that those presented here. The referenced samples are as a whole are examples of "slow on fast" systems [160], which support the existence of longitudinal guided modes. The samples studied and presented here are supposedly examples of semi-infinite medium, in which individual guided modes should not be observed [160].

The angular dependence of all of the frequency shifts of the SL Brillouin peaks are shown in Figs. 5.3(a)–(c) and 5.4(a)–(d). The modes are indicated by appropriate letters (R, S_i, QT and QL) in the plots. The frequency shifts of all the S_i phonons show linear dependence on the sine of the incident angle. The line of the best fit is shown as dotted line in Figs. 5.3(a)–(c) and 5.4(a)–(d).

The velocity of the surface Rayleigh mode is determined from the slope of the line of the best fit when Eq. (2.87) is fitted to the data shown in Figs. 5.3(a)-(c) and 5.4(a)-(d). The velocities of the QT and QL phonons were calculated using Eq. (2.81) for each angle. The obtained values are plotted as a function of the angle of phonon propagation inside the superlattice and are shown in Fig. 5.5(a)-5.6(d).

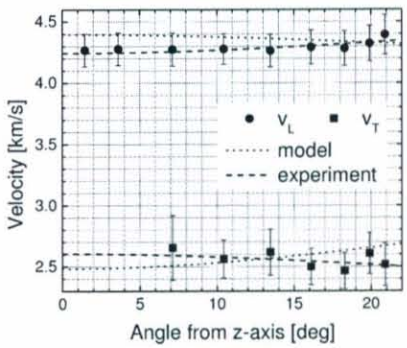

(a)

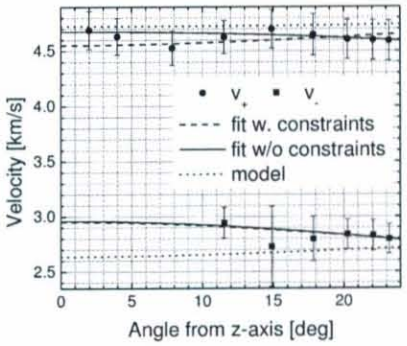

(b)

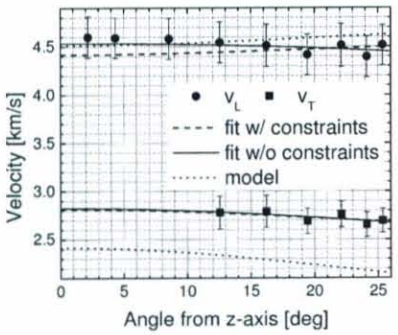

(c)

Figure 5.5: Bulk phonon velocities versus angle from z-axis for p-Si superlattices with 59%-33% (a), 59-44% (b) and 59-48% (c) porous constituent layers.

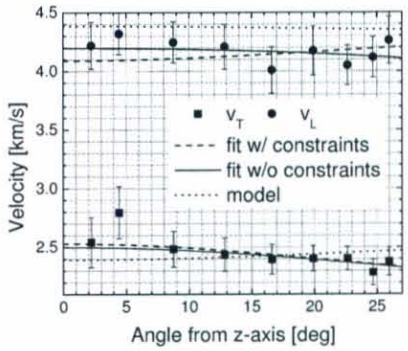

(a)

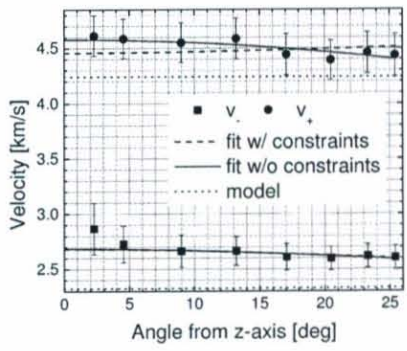

(b)

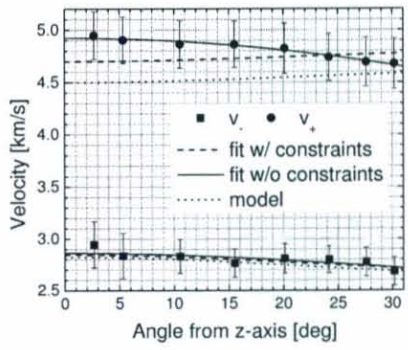

(c)

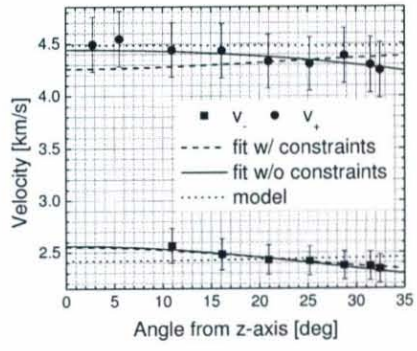

(d)

Figure 5.6: Bulk phonon velocities versus angle from z-axis for p-Si superlattices with 59%-52% (a), 59-54% (b), 59-70% (c) and 59-72% (d) porous constituent layers.

5.3 Elastic Constants

As the constituent layers were of cubic symmetry, the superlattices are concluded to be of at least tetragonal symmetry. The length in the direction perpendicular to the plane of layers is now defined by the modulation wavelength of the SL and is distinguished from any characteristic dimensions that could be observed in the planes of the layers. This conclusion in consistent with the Grimsditch-Nizzoli model [84], which predicts a tetragonal elastic constants tensor for a superlattice consisting of two layers of cubic symmetry. In order to obtain the elastic constants of the superlattices, Eqs. (2.53) and (2.54) were fitted the phonon velocity versus angle from z-axis data. To make sure that the most general case is taken into consideration, an attempt was made to fit expressions for the quasi-transverse and the quasi-longitudinal phonon propagating in a material of orthorhombic symmetry [101]. No reasonable fit was achieved due to limitations related to the number of data points and the size of their domain (small range of angles inside the material covered by the data points). As in the case of single layer films, the quasi-transverse mode was plotted as opposed to the pure transverse one. At low angles from the z-axis the mode velocities are nearly the same (QT and T are degenerate for $\theta_i' = 0$). The fitting of the directional dependence of the quasi-transverse phonon velocity also gives more precise results of elastic constants. This, however, may be related to the fact that v_- and v_+ are functions of the same four constants, c_{11}, c_{13}, c_{33} and c_{44}, in contrast to v_T, which depends only on c_{44} and c_{66}. The values of the former four constants are determined

during the fitting procedure.

The values of two of the elastic constants related directly to longitudinal and transverse velocities along [001] direction, c_{33} and c_{44}, can be directly calculated from the velocity of QL and QT at nearly normal incidence ($\theta_i = 5^o$ corresponding to $\theta_i' \sim 2^o$). In SLs with variable layer porosity less than 50% and also when it was 72%, the peak originating due to the QT phonon is not apparent at low incident angles. The transverse elastic constant, c_{44}, could not be therefore determined in this way for these superlattices. The elastic constants obtained from direct calculations were used as initial guesses during the fitting procedure. Additionally, the values of c_{11} were calculated assuming the first order S_i modes are longitudinal guided modes dependent on the elastic constant according to the $c_{11} \approx v_{S_1}^2 \rho$ [158].

The fitting process was performed twice resulting in two sets of elastic constants for the p-Si superlattices. In the first case the values of c_{ij} included in Eq. (2.53) and (2.54) were allowed to vary freely, with the only limits being those imposed by the stability conditions for a tetragonal system ($c_{11} > 0$ and $c_{44} > 0$ [99]). The values obtained from this process are referred to as fitted "without constraints" and are denoted "w/o constraints". The second set was fitted imposing an additional constraint, that is $c_{11} \geq c_{33}$. The rationale for this constraint comes only from the fact that for the model values such a relationship always applies. There is otherwise no physical reason why such a relationship should hold. In both cases fixing c_{33} and c_{44} on values determined directly from the Brillouin spectra resulted in slight decrease

of uncertainty associated with c_{11} and c_{13} but did not influence their values.

A complete set of effective elastic constants was determined using Grimsditch-Nizzoli model [84] for various combinations of cubic constituent layers with elastic constants as presented in Table 4.5. The values were calculated using Eqs. 2.67. These effective elastic constants along with those determined from SL Brillouin spectra are tabulated in Table 5.4.

A plot of all of the values of c_{33} and c_{44} versus average porosity of the p-Si superlattice is shown in Fig. 5.7. The values decrease with increasing average porosity of the superlattice. Excellent agreement is observed between c_{33} and c_{44} for the Grimsditch-Nizzoli model, both fits and values obtained directly from the spectra.

Although the fitting method did not much affect the values of c_{33} and c_{44}, the presence of constraints had a significant influence on the other two elastic constants for all samples with the exception of the superlattice made of 59%-33% constituent layers ("59-33"). In this case, the best fit both with and without constraints gave the same values of the elastic constants. For all of the other samples fitted with constraints, the value of c_{11} reached during iterations the lower limit imposed on it (i.e. the value of c_{33}). The obtained value of c_{11} does, however, agree within uncertainty with that calculated using Grimsditch-Nizzoli model, especially for samples with a high porosity variable layer. This result suggests lack of anisotropy and equivalence of all crystallographic axis, as for cubic material $c_{11} = c_{33}$ ([101]). Unfortunately, the fact that the value of c_{11} reaches the imposed limit decreases the credibility of the

Table 5.4: Effective elastic constants for p-Si superlattices obtained during four different procedures: directly from the velocities of bulk phonons at nearly normal incidence, from the fit of Eq. (2.53) and (2.54) to the experimental data w/o and with constraints placed on the value of c_{11} and using the Grimsditch-Nizzoli [84] model. The asterisk by the value of c_{11} indicates the elastic constant calculated using the velocity of the first order pseudo-surface phonon.

SAMPLE:		59%-33%	59%-44%	59%-48%	59%-52%	59%-54%	59%-70%	59%-72%
ξ_{ave} [%]:		43±2	50±2	54±3	56±2	57±2	65±2	67±2
DIRECT	c_{11}^*	15±1	16.4±0.6	13±1	17±1	15.1±0.4	12.1±0.7	6.8±0.6
	c_{33}	—	25.0±0.5	22.0±0.7	18.1±0.5	21.0±0.3	19.8±0.2	14.0±0.5
	c_{44}	—	—	—	—	7.2±0.1	6.8±0.1	5.06±0.08
w/o CONSTRAINTS	c_{11}	—	13±5	13±5	10±4	10±3	9±2	8±1
	c_{13}	—	3±3	3±3	4±2	1±2	1±1	3.3±0.6
	c_{33}	—	25.0±0.5	22.0±0.7	18.1±0.5	21.0±0.3	19.8±0.2	14.0±0.5
	c_{44}	—	10.2±0.3	8.6±0.3	6.4±0.2	7.2±0.1	6.8±0.1	5.06±0.08
w/ CONSTRAINTS	c_{11}	30±20	24±7	21±6	17±5	20±6	18±3	14±2
	c_{13}	10±6	8±2	6±2	7±2	7±2	6±1	5.7±0.7
	c_{33}	24±1	24.1±0.7	21.1±0.8	17.2±0.6	19.7±0.5	18.4±0.2	14.0±0.5
	c_{44}	9±1	10.2±0.5	8.6±0.4	6.6±0.3	7.2±0.3	6.6±0.2	5.0±0.2
MODEL	c_{11}	29±1	30±1	21±1	20.2±0.8	18.0±0.3	15.6±0.6	15.7±0.4
	c_{12}	4±4	11±2	12±1	7±1	7.1±0.8	6.5±0.8	6.3±0.3
	c_{13}	5±3	10±2	13±1	7±1	7.1±0.8	6.5±0.8	6.3±0.3
	c_{33}	25.7±0.8	26±1	22±1	19.8±0.8	18.0±0.5	16.5±0.6	15.5±0.4
	c_{44}	8.2±0.5	8.1±0.7	6.3±0.7	5.9±0.5	5.4±0.3	5.1±0.3	4.5±0.2
	c_{66}	12.0±0.7	12±1	7±1	6.4±0.6	5.6±0.3	5.1±0.4	4.5±0.2

result. Without the constraint that $c_{11} > c_{33}$ imposed on the elastic constants during the fit, the results for all samples other than "59-33" suggest significant anisotropy in the tetragonal superlattice, with values of c_{11} smaller than those of c_{33}. The ratio c_{11}/c_{33}, that can serve as one of anisotropy ratios for the tetragonal lattice, is plotted as a function of porosity in Fig. 5.9 for three methods for which both values were determined. Agreement between the model and the fit with constraint, especially for samples with variable layer of porosity higher than 50%, is observed, while the ratios for two fits differ substantially.

The unknown origin of the S_i modes inspired checking the relationship between the velocity of the first order pseudo-surface mode S_1 and the elastic constant c_{11}, $c_{11} = v_{S_1}^2 \rho$ [159]. The results of the calculations, presented in Table 5.4 (as $c_{11}^{\star}$) show reasonable agreement with values of c_{11} determined for the fit without constraints. The values turn out to be approximately 10% higher that those of c_{11} obtained from the fit without constraint, which is similar to Dutcher's observations [158]. The data points are plotted versus SL average porosity in Fig. 5.8.

The values of c_{13} obtained with constraints show better agreement with the modeled values for superlattices with higher average porosity. The lack of agreement between experimental values and model in superlattices with variable layer of lower porosity is, at least partially, a consequence of the difficulties in obtaining the elastic constants for those layers. The elastic constant c_{13} is strongly dependent on $c_{12}^{[\zeta]}$, which was the one determined with the lowest accuracy and in the case of low porosity layers

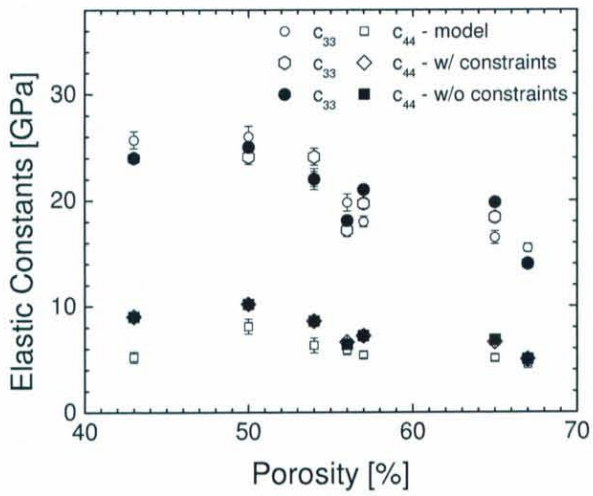

Figure 5.7: Porosity dependence of the longitudinal (c_{33}) and transverse (c_{44}) elastic constants for p-Si superlattices. The values obtained via Grimsditch-Nizzoli model (○ and □ for c_{33} and c_{44}, respectively) and using two different fitting procedures (○ and ◇ for c_{33} and c_{44} fitted with constraints, • and ■ for c_{33} and c_{44} fitted without constraints).

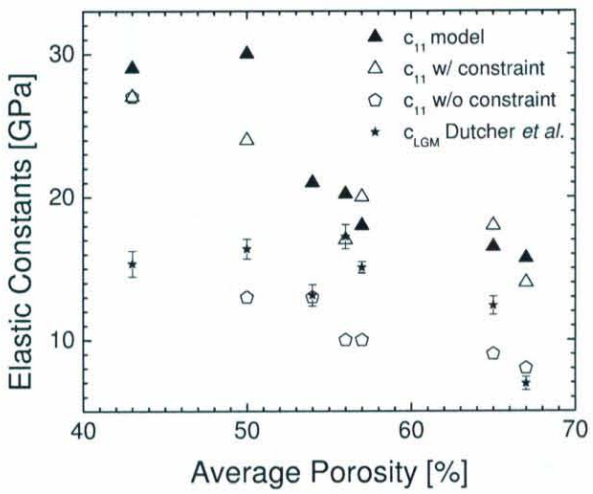

Figure 5.8: Porosity dependence of the c_{11} elastic constant for p-Si superlattices. The values shown as ⋆ are elastic constants calculated using velocity of a first order pseudo-transverse mode S_1 using relationship provided by Dutcher [158]

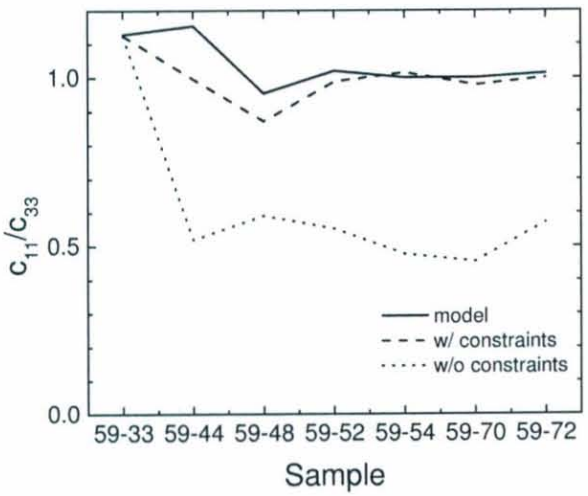

Figure 5.9: c_{11}/c_{33} versus average superlattice porosity.

carry significant uncertainties. The values of c_{13} obtained in fit without constraints for the most part (with the exception of value obtained for SL with 72% porous variable layer) agree within uncertainties. Their absolute uncertainties, however, are approximately equal to their values.

Out of the four experimentally determined elastic constants only the ratio of two longitudinal elastic constants (c_{11} and c_{33}) could serve as an anisotropy measurement. The anisotropy ratio shown in Fig. 5.9 serves as an indication of the applicability of the Grimsditch-Nizzoli model. The dependence confirms the agreement between the model and the constrained fit and lack thereof in the fit without constraints.

With the increase of the porosity of the constituent layers, the effective elastic

constant tensor obtained using the Grimsditch-Nizzoli model for the SLs changed from that of tetragonal symmetry to that of cubic with $c_{11} \approx c_{33}$, $c_{12} \approx c_{13}$ and $c_{44} \approx c_{66}$. This is likely related to the decrease of the difference between the elastic constants of the constituent layers. As shown in Fig 5.10, the difference between model values of appropriate pairs of elastic constants (c_{11} and c_{33}, c_{12} and c_{13}, and c_{44} and c_{66}, respectively) goes to zero as the difference between values of the longitudinal elastic constant of the constituent layers $c_{11}^{[\zeta]}$ decreases. At the same limit ($\Delta c_{ij}^{[\zeta]} \rightarrow 0$) the anisotropy ratio c_{11}/c_{33}, approaches unity. This result could be explained by the fact that for more elastically similar constituent layers the less stress and strain exists on the boundaries between them. Should the experimentally determined elastic constants follow the same trend, it would open a possibility to create materials of the same density, porosity and characterized by identical optical properties, however differing elastically, depending on the constituent layers. For example, a SL with constituent layers of equal thickness and of 30% and 60% porosity form the same effective medium of the same average porosity, density and refractive index as SL composed of 40% and 50% porous layers. However, because the elastic constants of the constituent layers vary, the effective media would be characterized by different sets of effective elastic constants.

The values of c_{33} and c_{44} obtained for the fit without constraints are used to calculate the velocities of bulk phonons propagating along [001] direction using Eqs (2.53) and (2.54) for $\theta_i' = 0^o$. The velocities of all of the phonons are presented together in

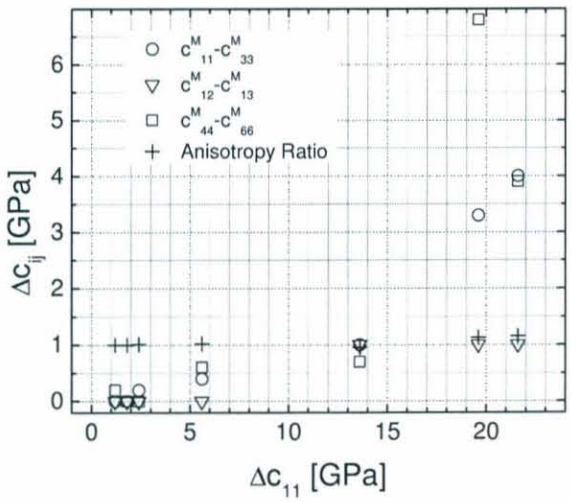

Figure 5.10: Relationship between the pairs of effective elastic constants and the differences in the elastic constants of the constituent layers of the superlattice as obtained using Grimsditch-Nizzoli model [84].

Table 5.5. As one can see, the values of surface phonon velocities, in general, decrease with increasing average porosity of the superlattice. The only two values that appear not to follow the trend are those for superlattices with either 33% porous variable layer or 44% porous layer. In the former case, the value is lower than expected, in the latter, higher. This is consistent with observations of phonon velocities in single layers (see Table 4.6). The reason for this could be related to the uncertainty in mass loss and therefore porosity of the layers of low porosity that carries through all the velocity calculations or to the morphology of the constituent layers, causing such anomaly. The velocities of S_i phonons presented in the Table 5.5 are calculated using

Table 5.5: Surface, pseudo-surface and bulk phonon velocities of p-Si superlattices. The values of bulk phonon velocities are calculated for the [001] direction of propagation using elastic constants obtained during the fit without constraints.

Superlattice	Phonon Velocity				
	v_R [km/s]	v_{S_1} [km/s]	v_{S_2} [km/s]	v_T [km/s]	v_L [km/s]
59-33	2.35±0.05	3.4±0.1	5.2±0.2	2.6±0.1	4.25±0.09
59-44	2.65±0.02	3.75±0.08	5.0±0.1	2.96±0.04	4.63±0.05
59-48	2.50±0.02	3.5±0.1	4.6±0.2	2.83±0.05	4.53±0.07
59-52	2.29±0.03	4.1±0.1	—	2.50±0.04	4.20±0.06
59-54	2.29±0.02	3.88±0.05	—	2.68±0.02	4.58±0.03
59-70	2.27±0.02	3.9±0.1	—	2.89±0.02	4.93±0.03
59-72	1.97±0.02	3.0±0.1	—	2.55±0.05	4.27±0.08

the same procedure as for surface Rayleigh phonons with intercept on frequency shift axis forced to be zero, *i.e* assuming the peaks originate due to longitudinal guided phonons. The velocities of the transverse and longitudinal bulk acoustic phonons are calculated for phonons propagating along the [001] direction (i.e., normal to the plane of the SL constituent layers).

Very good agreement is observed between these values and those calculated for small incident angles (see Table 5.6). The velocity of the transverse mode is lower than that of the first order pseudo-surface mode which agrees with the idea that the latter could originate from a "leaky" longitudinal mode propagating nearly parallel to the surface. It should be noted that all pseudo-surface modes labeled S_2 are of higher velocity that the bulk longitudinal phonon propagating in the superlattice. Fig 5.3 shows a plot of longitudinal and transverse velocity data points for superlattices and single layers of comparable porosity. Although it is not apparent from the Fig 5.3, the velocities of bulk phonons in SL are dependent on the average porosity of the film.

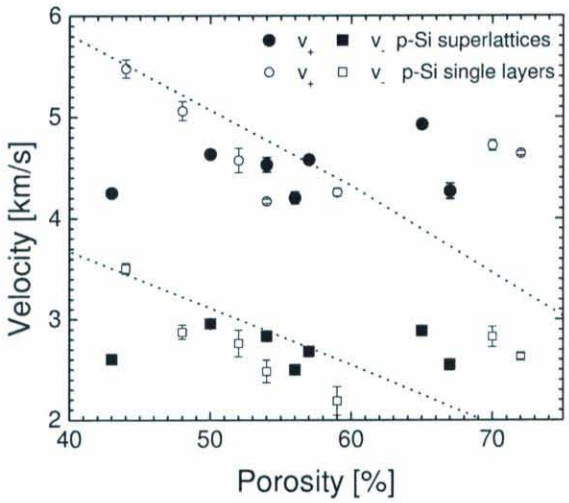

Figure 5.11: Porosity dependence of the longitudinal and transverse phonon velocities for p-Si superlattices and single layers. The dotted line presents the porosity dependence of the p-Si single layers according to Eq. (4.3).

The reason for lack of obvious trend is connected to the range of average porosities and the fact that any data point that originates from the 33% porous layer creates an anomaly.

The values of the effective elastic constants depend on the elastic constants of the constituent layers and on the constituent layer thickness ratio. As all of these values carry uncertainty one way of checking whether the lack of agreement between the values of c_{11} and c_{13} obtained for a fit without constraints and the model is associated with those uncertainties was to work out the elastic constants of the variable layer from the Eqs. (2.67). The elastic constants c_{11}, c_{13}, c_{33} and c_{44} obtained from the fit without constraints and the elastic constants $c_{11}^{[1]}$, $c_{12}^{[1]}$ and $c_{44}^{[1]}$ of the permanent constituent

Table 5.6: Comparison of T and L bulk phonon velocities propagating along [001] direction and QT and QL phonons calculated for small incident angles.

Superlattice [km/s]	v_- [km/s]	v_T [km/s]	v_+ [km/s]	v_L [km/s]
59-33	—	2.6±0.1	4.3±0.1	4.25±0.09
59-44	—	2.96±0.04	4.7±0.1	4.63±0.05
59-48	—	2.83±0.05	4.6±0.2	4.53±0.07
59-52	2.5±0.2	2.50±0.04	4.2±0.2	4.20±0.06
59-54	2.9±0.2	2.68±0.02	4.5±0.2	4.58±0.03
59-70	2.9±0.2	2.89±0.02	4.9±0.2	4.93±0.03
59-72	—	2.55±0.05	4.5±0.3	4.27±0.08

layer (as they are the same for each sample) were then substituted into the expressions for c_{11}, c_{13}, c_{33}, and c_{44} according to Eqs. (2.67a), (2.67c), (2.67d) and (2.67e) in the model calculations. The elastic constants and the thickness ratio for the variable layer were obtained and the results disagreed with the stability conditions that have to be imposed on the cubic layer [110]. The values of c_{44} were negative, what for cubic material would make the strain energy of the lattice negative. Additionally, for most superlattices, the obtained values of thickness ratios were unreasonable (either significantly larger than unity or very close to 0).

Elastic properties of p-Si superlattices consisting of 60% and 30% constituent layers with modulation wavelength of 17 nm are discussed by Polomska *et al.* [95]. The p-Si layers were assumed to be isotropic, therefore the superlattices were modeled as hexagonal, with the same constraint as used here for one of the fits imposed on the values of effective elastic constants. The experimental and model elastic constants are fairly different and only qualitative agreement is obtained. Rough agreement

between the experimental values reported by the author (c_{11}=16.9 GPa, c_{13}=4.7 GPa, c_{33}=15.4 GPa and c_{44}=5.2 GPa) and those presented in this work for the superlattice with comparable average porosity is obtained. This could be related to the choice of symmetry of the p-Si single layers and consequently the superlattices, the difference in fabrication (electrolyte composition) or the thickness ratios.

Based on the results presented in this work the applicability of the Grimsditch-Nizzoli model for p-Si multilayered structures is not certain. The excellent agreement obtained for two elastic constants (c_{33} and c_{44}) which values can be calculated directly from the spectra may either mean that the other two cannot be determined due to uncertainties involved in the experiments (contributed by porosity, etched area, etch rates, frequency shifts, etc.) or that the at the present form the model is not a good representation of the elastic properties of p-Si structures. The experimental results obtained for polymers [88,90] and some quasi-periodic structures [93,94] showed agreement with the Grimsditch-Nizzoli model, suggesting that it could be used to describe elastic properties of unconventional multilayered systems. In the case of p-Si superlattices the problem may be related to the boundary conditions in the interfaces between the constituent layers, as the system was created by etching a stable, solid crystalline wafer as oppose to the deposition of the individual layers on the free surface, creating strains and stresses as the structure is created. Additionally, the presence of the pores could influence the applicability of the model. The size of the pores is smaller than that of acoustic phonons propagating in the films therefore, on

macroscopic level, the p-Si layer can be treated as an effective medium. The size of the pores and microstructure of the film, however, was shown to affect the value of elastic constants of single p-Si films. The other possible explanation could be related to the problem of boundary conditions at the interfaces between constituent porous layers. The lateral roughness of the interfaces is not included in the assumption of the Grimsditch-Nizzoli model. The interfaces are sharp on a nm scale [7], which could be of a significance for layers of thickness of $\sim$10 nm. It is also uncertain whether the fact that the pore size and the layer thickness in SL are of comparable dimension is of any importance for the determination of the boundary conditions and therefore the effective elastic constants of the porous multilayered film.

Chapter 6

Conclusions

The elastic properties of single p-Si layers were determined for layers with porosity ranging from 30% to 72% using Brillouin light scattering technique. The peaks observed in the spectra were identified as originating due to surface Rayleigh R, pseudo-surface S_i, quasi-transverse QT and quasi-longitudinal QL bulk acoustic modes.

The quality of the Brillouin spectra collected from p-Si single layers increases with layer porosity. This could be attributed to the decrease of the attenuation of the light penetrating the film which results in an increase in the scattering volume. The intensities of the QT and QL bulk acoustic modes change with the porosity of the single layer and with the incident angle. The ratio of absolute intensities, I_T/I_L, increases with incident angle.

The velocities of the QT and QL were plotted as a function of incident angle inside the sample, θ_i'. A set of elastic constants was determined for each p-Si layer. The values of the longitudinal and transverse elastic constants depended on the porosity

according to equations

$$c_{11} = 166(1-\xi)^{2.8}, \tag{6.1a}$$

$$c_{44} = 79(1-\xi)^{3.2}. \tag{6.1b}$$

The porosity dependence of Young's modulus ($Y = c_{11} - \frac{2c_{12}^2}{c_{11}+c_{12}}$) was also determined. The relationship between Y and porosity is described by

$$Y = 130(1-\xi)^{2.8}. \tag{6.2}$$

The values of c_{11} and c_{44} were used to obtain the longitudinal and transverse velocities of acoustic phonons propagating along [001] direction in the p-Si layer. The dependence of the velocities on porosity was found to follow equations

$$v_L = 8.44(1-\xi)^{0.73}, \tag{6.2a}$$

$$v_T = 5.82(1-\xi)^{0.9}. \tag{6.2b}$$

The relation between the empirical parameters describing porosity dependence (γ_i in Eqs. 4.1 and 4.3) determined for longitudinal and transverse elastic constants and respective velocities follow the relationship $\gamma_{11,44} = 2\gamma_{L,T} + 1$ (2.5 ± 0.1 and 2.8 ± 0.2 calculated from values of $\gamma_{L,T}$ in comparison with 2.8 ± 0.2 and 3.2 ± 0.2, respectively obtained from the c_{ij} vs porosity data). The size of the empirical parameters γ_T, L suggests that the p-Si structure is rather well-ordered.

The elastic constants of p-Si superlattices were determined through examination of superlattices with one identical constituent layer (59% porous) and one varying from superlattice to superlattice, covering the range from 33% porous to 72% porous.

Four out of the six elastic constants of the tetragonal SLs were determined using two different fitting approaches (with and without constraints on the value of c_{11}) and compared to those determined using the Grimsditch-Nizzoli model [84]. The first one, a fit with the imposed constraint $c_{11} > c_{33}$ resulted in values that agree with the model. However, problems that occurred during fitting make the credibility of the values obtained questionable. The second fit, allowing all the elastic constants to vary freely with exception of stability conditions, resulted in partial agreement (c_{33} and c_{44}) and completely different values of c_{11} and c_{13} from those determined by the model.

The elastic constants c_{11}, c_{33} and c_{44} were also determined directly from the spectra, using velocities of longitudinal, transverse and first order pseudo-surface mode, respectively. Those values show agreement with fits obtained without constraints.

The velocities of the longitudinal and transverse modes propagating along [001] direction in superlattices are comparable to those obtained for single p-Si layers with the same average porosity. Additionally, the difference between the velocities of the transverse and longitudinal phonons propagating along [001] direction and those of QT and QL calculated from Brillouin spectra collected at incident angle of a few degrees was negligible.

The presence of pseudo-surface modes, which yield values of c_{11} that support the validity of the fit without constraints (i.e., c_{11} calculated from pseudo-surface mode are comparable to the values of c_{11} obtained from fit without constraints), and the fact that an attempt to work "backward" to the values of elastic constants of the constituent layers failed to yield physically reasonable values suggests that adjustments to the model may have to be made before it can accurately predict the elastic constants of the p-Si and other similarly formed superlattices.

Based on the results no definite statement on the applicability of the Grimsditch-Nizzoli model to the p-Si superlattices can be made. The excellent agreement obtained for two elastic constants (c_{33} and c_{44}) may either mean that the other two cannot be determined due to uncertainties involved in the experiments (contributed by porosity, etched area, etch rates, frequency shifts, etc.) or that the model needs some adjustment in order to work for superlattices created by electrochemical etching of a bulk crystalline parent material. The comparable dimensions of the pore size and the layer thickness in SL could carry significance in determination of the applicability of the model. Additionally, the presence of the pores could be a factor as well. The size of the pores is smaller than that of acoustic phonons propagating in the films and macroscopically the p-Si layer can be treated as an effective medium. The size of the pores and morphology of the film affect the value of elastic constants of single layers therefore the influence of the microstructure on the elastic properties can be important. The other possible explanation of the discrepancies between the values of

the elastic constants could be related to the problem of boundary conditions at the interfaces between constituent porous layers. The interfaces between layers of different porosities are sharp on a nm scale [7] and the lateral roughness is not anyhow included in the assumptions of the model.

The difference in the anisotropy ratios, c_{11}/c_{33}, determined for the model and the fit without constrains shows that the elastic constants of superlattices could differ from those of single layered film with the same porosity. This gives more space for tailoring of the elastic properties of p-Si, making them more adjustable for applications in different fields.

The Brillouin light scattering was shown to be an effective tool for characterization of p-Si multilayered structure. Additional experiments, using different scattering geometries, light polarization and sample orientation would provide information regarding the phonons which velocities are related to other elastic constants (especially c_{66}). These data would help in determination the validity of the Grimsditch-Nizzoli model and verify the need of its adjustments. Finally, the characterization of porous multilayered structures and superlattices formed by other means than deposition could both benefit from the findings of this work and possible modifications of the model as well as help its development.

Appendix A

Additional Data

Frequency shifts and phonon velocities of the second set of superlattices are shown in Tables A.1 and A.2. The elastic constants, determined with stability conditions as constraints (i.e. using the method described as "without constraints" in the thesis) are presented in Table A.3. All samples were made and characterized the way described in Chapter 3.1. The samples numbered 2.21#1, 2.21#3 and 2.21#7 were made using HF from a different supply.

Table A.1: Frequency shifts and phonon velocities of p-Si superlattices 2.21#1 (59%–48%) and 2.21#3 (59%–52%).

Sample	θ_i	θ_i'	Frequency Shift					Phonon Velocity	
			R	S_1	S_2	QT	QL	v_-	v_+
	[deg]	[deg]	[GHz]	[GHz]	[GHz]	[GHz]	[GHz]	[km/s]	[km/s]
2.21#1	5	2	—	—	—	—	39.8±0.1	—	4.6±0.4
	10	4	—	—	—	—	42.7± 0.2	—	4.9±0.4
	20	9	—	—	—	—	41.7±0.3	—	4.8±0.5
	30	13	—	—	—	22±	42.1±0.1	2.5±0.7	4.9±0.4
	40	16	6.36±0.01	10.1±0.2	—	24.6±0.4	42.4±0.2	2.8±0.3	4.9±0.5
	50	19	7.41±0.01	11.3±0.2	16±1	26.0±0.5	42.9±0.2	3.0±0.3	5.0±0.5
	60	22	8.28±0.01	—	—	25.4±0.4	42.3±0.3	2.9±0.3	4.9±0.5
	70	24	8.83±0.01	—	—	25.3±0.2	41.6±0.4	2.9±0.3	4.8±0.5
	74	25	9.19±0.01	—	—	25.7±0.4	42.6±0.6	3.0±0.3	4.9±0.5
2.21#3	5	2	—	—	—	27.0±2	37.2±0.2	3.2±0.4	4.6±0.2
	10	4	—	—	—	25±2	39.4±0.2	3.0±0.4	4.7±0.2
	20	9	—	—	—	24±1	39.4±0.1	2.9±0.2	4.7±0.2
	30	13	—	—	—	22.7±0.3	38.5±0.1	2.7±0.2	4.6±0.2
	40	17	5.75±0.01	9.6±0.1	—	22.3±0.3	38.3±0.2	2.6±0.1	4.5±0.2
	50	20	6.82±0.01	11.11±0.08	—	22.0±0.1	37.7±0.1	2.6±0.1	4.5±0.2
	60	23	7.48±0.01	12.0±0.1	—	22.0±0.1	38.1±0.2	2.6±0.1	4.5±0.2
	70	25	8.03±0.01	12.63±0.07	—	22.0±0.1	38.4±0.2	2.6±0.1	4.5±0.2
	75	26	8.27±0.02	13.0±0.1	—	22.2±0.2	38.6±0.3	2.6±0.1	4.6±0.2

Table A.2: Frequency shifts and phonon velocities of p-Si superlattices 2.18#6 (59%–70%) and 2.21#7 (59%–72%).

Sample	θ_i	θ_i'	Frequency Shift				Phonon Velocity	
			R	S_1	QT	QL	v_-	v_+
	[deg]	[deg]	[GHz]	[GHz]	[GHz]	[GHz]	[km/s]	[km/s]
2.18#6	5	3	—	—	21.4±0.7	34.3±0.1	3.0±0.2	4.8±0.3
	10	5	—	—	19.7±0.6	34.6±0.1	2.8±0.2	4.8±0.3
	20	11	—	—	19.8±0.4	34.4±0.2	2.7±0.2	4.8±0.3
	30	16	—	—	19.3±0.2	32.8±0.1	2.7±0.2	4.7±0.3
	40	20	—	—	18.98±0.07	32.9±0.1	2.7±0.1	4.6±0.3
	50	24	6.46±0.01	10.7±0.2	18.85±0.07	32.5±0.1	2.6±0.1	4.5±0.3
	60	28	7.24±0.01	—	18.4±0.1	32.7±0.2	2.6±0.2	4.6±0.3
	70	30	7.71±0.01	13.1±0.1	18.67±0.06	32.4±0.0	2.6±0.1	4.5±0.3
	80	31	8.02±0.01	13.4±0.4	18.74±0.09	32.0±0.3	2.6±0.2	4.5±0.3
2.21#7	5	3	—	—	—	32.1±0.1	—	4.7±0.3
	10	6	—	—	20.0±0.6	32.23±0.07	3.0±0.3	4.8±0.3
	20	11	—	—	18.9±0.3	31.94±0.07	2.8±0.2	4.7±0.3
	30	16	—	—	17.6±0.1	31.2±0.1	2.6±0.2	4.6±0.3
	40	21	—	—	17.54±0.04	30.97±0.09	2.6±0.2	4.6±0.3
	50	25	6.16±0.01	9.7±0.1	17.55±0.05	31.2±0.2	2.6±0.2	4.6±0.3
	60	29	6.90±0.01	10.67±0.07	17.39±0.03	30.9±0.1	2.6±0.1	4.6±0.3
	70	31	7.40±0.01	11.41±0.07	17.52±0.03	31.0±0.1	2.6±0.1	4.6±0.3
	75	32	7.66±0.02	11.9±0.1	17.78±0.07	21.8±0.2	2.6±0.2	4.7±0.3

Table A.3: Elastic constants for the second set of p-Si superlattices determined using the fit without constraints.

Sample	Elastic Constants			
	c_{11}	c_{13}	c_{33}	c_{44}
α [%]	[GPa]	[GPa]	[GPa]	[GPa]
59 – 48	32±7	8±3	26.2±0.8	8.2±0.6
59 – 52	8±5	3±3	22.2±0.5	8.3±0.3
59 – 70	7±7	1±6	19.1±0.1	6.5±0.5
59 – 72	12±7	5±3	18±1	6.1±0.6

Appendix B

Grimsditch-Nizzoli model for constituent layers of cubic symmetry

Derivation of the effective elastic constants using Grimsditch-Nizzoli model for the case of two constituent layers of cubic symmetry.

The equation that allows to calculate the effective elastic constants, Eq. (2.65) is of form

$$\boldsymbol{c} = (f^{[1]}\boldsymbol{c}^{[1]}\boldsymbol{M} + f^{[2]}\boldsymbol{c}^{[2]})(f^{[1]}\boldsymbol{M} + f^{[2]}\boldsymbol{I})^{-1}.$$

The boundary condition (2.61) can be written as

$$\boldsymbol{P}^{[1]}\boldsymbol{\mu}^{[1]} = \boldsymbol{P}^{[2]}\boldsymbol{\mu}^{[2]},$$

which leads to Eq. (2.62) if $\boldsymbol{M}$ is defined as

$$\boldsymbol{M} = \boldsymbol{P}^{[1]^{-1}} \boldsymbol{P}^{[2]}.$$

For a cubic layer, the matrix P is defined as

$$\boldsymbol{P}^{[\zeta]} = \begin{bmatrix} 1 & 0 & 0 & 0 & 0 & 0 \\ 0 & 1 & 0 & 0 & 0 & 0 \\ c_{12}^{[\zeta]} & c_{12}^{[\zeta]} & c_{11}^{[\zeta]} & 0 & 0 & 0 \\ 0 & 0 & 0 & c_{44}^{[\zeta]} & 0 & 0 \\ 0 & 0 & 0 & 0 & c_{44}^{[\zeta]} & 0 \\ 0 & 0 & 0 & 0 & 0 & 1 \end{bmatrix},$$

what leads to the transformation matrix $\boldsymbol{M}$ of form

$$\boldsymbol{M} = \begin{bmatrix} 1 & 0 & 0 & 0 & 0 & 0 \\ 0 & 1 & 0 & 0 & 0 & 0 \\ -\frac{c_{12}^{[1]}+c_{12}^{[2]}}{c_{11}^{[1]}} & -\frac{c_{12}^{[1]}+c_{12}^{[2]}}{c_{11}^{[1]}} & \frac{c_{11}^{[2]}}{c_{11}^{[1]}} & 0 & 0 & 0 \\ 0 & 0 & 0 & \frac{c_{44}^{[2]}}{c_{44}^{[1]}} & 0 & 0 \\ 0 & 0 & 0 & 0 & \frac{c_{44}^{[2]}}{c_{44}^{[1]}} & 0 \\ 0 & 0 & 0 & 0 & 0 & 1 \end{bmatrix}.$$

Working out the first part of Eq. (2.65), namely $\boldsymbol{A1} = f^{[1]}\boldsymbol{c}^{[1]}\boldsymbol{M}$ gives

$$\boldsymbol{A1} = \begin{bmatrix} (c_{11}^{[1]} + c_{12}^{[1]}(\frac{-c_{12}^{[1]}+c_{12}^{[2]}}{c_{11}^{[1]}}))f^{[1]} & (c_{12}^{[1]} + c_{12}^{[1]}(\frac{-c_{12}^{[1]}+c_{12}^{[2]}}{c_{11}^{[1]}}))f^{[1]} & \frac{c_{12}^{[1]}c_{11}^{[2]}f^{[1]}}{c_{11}^{[1]}} & 0 & 0 & 0 \\ (c_{11}^{[1]} + c_{12}^{[1]}(\frac{-c_{12}^{[1]}+c_{12}^{[2]}}{c_{11}^{[1]}}))f^{[1]} & (c_{11}^{[1]} + c_{12}^{[1]}(\frac{-c_{12}^{[1]}+c_{12}^{[2]}}{c_{11}^{[1]}}))f^{[1]} & \frac{c_{12}^{[1]}c_{11}^{[2]}f^{[1]}}{c_{11}^{[1]}} & 0 & 0 & 0 \\ (c_{12}^{[1]} + c_{11}^{[1]}(\frac{-c_{12}^{[1]}+c_{12}^{[2]}}{c_{11}^{[1]}}))f^{[1]} & (c_{12}^{[1]} + c_{11}^{[1]}(\frac{-c_{12}^{[1]}+c_{12}^{[2]}}{c_{11}^{[1]}}))f^{[1]} & c_{11}^{[2]}f^{[1]} & 0 & 0 & 0 \\ 0 & 0 & 0 & c_{44}^{[2]}f^{[1]} & 0 & 0 \\ 0 & 0 & 0 & 0 & c_{44}^{[2]}f^{[1]} & 0 \\ 0 & 0 & 0 & 0 & 0 & c_{44}^{[2]}f^{[1]} \end{bmatrix}.$$

The second element of the sum in the first bracket, matrix $\boldsymbol{A2} = \boldsymbol{c}^{[2]}f^{[2]}$ is equal to

$$\boldsymbol{A2} = \begin{bmatrix} c_{11}^{[2]}f^{[2]} & c_{12}^{[2]}f^{[2]} & c_{12}^{[2]}f^{[2]} & 0 & 0 & 0 \\ c_{12}^{[2]}f^{[2]} & c_{11}^{[2]}f^{[2]} & c_{12}^{[2]}f^{[2]} & 0 & 0 & 0 \\ c_{12}^{[2]}f^{[2]} & c_{12}^{[2]}f^{[2]} & c_{11}^{[2]}f^{[2]} & 0 & 0 & 0 \\ 0 & 0 & 0 & c_{44}^{[2]}f^{[2]} & 0 & 0 \\ 0 & 0 & 0 & 0 & c_{44}^{[2]}f^{[2]} & 0 \\ 0 & 0 & 0 & 0 & 0 & c_{44}^{[2]}f^{[2]} \end{bmatrix}.$$

The last element, $\boldsymbol{A3} = f^{[1]}\boldsymbol{M} + f^{[2]}\boldsymbol{I}$ is

$$\boldsymbol{A3} = \begin{bmatrix} f^{[1]}+f^{[2]} & 0 & 0 & 0 & 0 & 0 \\ 0 & f^{[1]}+f^{[2]} & 0 & 0 & 0 & 0 \\ \frac{-c_{12}^{[1]}+c_{12}^{[2]}}{c_{11}^{[1]}} f^{[1]} & \frac{-c_{12}^{[1]}+c_{12}^{[2]}}{c_{11}^{[1]}} f^{[1]} & \frac{c_{11}^{[2]}}{c_{11}^{[1]}}+f^{[2]} & 0 & 0 & 0 \\ 0 & 0 & 0 & \frac{c_{44}^{[2]}}{c_{44}^{[1]}}+f^{[2]} & 0 & 0 \\ 0 & 0 & 0 & 0 & \frac{c_{44}^{[2]}}{c_{44}^{[1]}}+f^{[2]} & 0 \\ 0 & 0 & 0 & 0 & 0 & f^{[1]}+f^{[2]} \end{bmatrix}.$$

Finally, the calculation of the inverse of matrix $\boldsymbol{A3}$, $\boldsymbol{A4} = (f^{[1]}\boldsymbol{M} + f^{[2]}\boldsymbol{I})^{-1}$ results in matrix of form

$$\boldsymbol{A4} = \begin{bmatrix} \frac{1}{f^{[1]}+f^{[2]}} & 0 & 0 & 0 & 0 & 0 \\ 0 & \frac{1}{f^{[1]}+f^{[2]}} & 0 & 0 & 0 & 0 \\ \frac{(-c_{12}^{[1]}+c_{12}^{[2]})f^{[1]}}{(f^{[1]}+f^{[2]})(c_{11}^{[1]}f^{[2]}+c_{11}^{[2]}f^{[1]})} & \frac{(-c_{12}^{[1]}+c_{12}^{[2]})f^{[1]}}{(f^{[1]}+f^{[2]})(c_{11}^{[1]}f^{[2]}+c_{11}^{[2]}f^{[1]})} & \frac{1}{\frac{c_{11}^{[2]}}{c_{11}^{[1]}}+f^{[2]}} & 0 & 0 & 0 \\ 0 & 0 & 0 & \frac{1}{\frac{c_{44}^{[2]}}{c_{44}^{[1]}}+f^{[2]}} & 0 & 0 \\ 0 & 0 & 0 & 0 & \frac{1}{\frac{c_{44}^{[2]}}{c_{44}^{[1]}}+f^{[2]}} & 0 \\ 0 & 0 & 0 & 0 & 0 & \frac{1}{f^{[1]}+f^{[2]}} \end{bmatrix}.$$

Performing the last operation, multiplication of matrices $(\boldsymbol{A1}+\boldsymbol{A2}).\boldsymbol{A4}$ gives an elastic tensor of this multilayered film, $\boldsymbol{c}$ with six independent elastic constants c_{11}, c_{12}, c_{13}, c_{33}, c_{44} and c_{66} and is of the form shown by Eq. (2.66) with the components calculated using Eqs. (2.67).

Bibliography

[1] A. Uhlir, Bell System Tech. J. **35**, (1956).

[2] V. P. Bondarenko and V. A. Yakovtseva, in *Properties of Porous Silicon*, edited by L. Canham (INSPEC, Great Britain, 1997), Chap. 12, pp. 343–348.

[3] L. Canham, Appl. Phys. Lett. **57**, 1046 (1990).

[4] A. Rosengren, L. Wallman, M. Bengtsson, T. Laurell, N. Danielsen, and L. M. Bjursten, Phys. Stat, Sol. (a) **182**, 527 (2000).

[5] L. Canham, Adv. Mater. **8**, 850 (1996).

[6] V. Lehmann, *Electrochemistry of Silicon* (Wiley-VCH, Weinheim, 2002).

[7] L. Pavesi, Riv. Nuovo Cimento **20**, 1 (1997).

[8] D. Buttard, D. Bellet, G. Dolino, and T. Baumbach, J. Appl. Phys. **83**, 5814 (1998).

[9] T. Bourbié, O. Coussy, and B. Zinszner, *Acoustics of Porous Media* (Gulf Publishing Company, Paris, 1987).

[10] R. Hérino, in *Properties of Porous Silicon*, edited by L. Canham (INSPEC, Great Britain, 1997), Chap. 2, pp. 89–96.

[11] B. Hamilton, Semicond. Sci. Technol. **10**, 1187 (1995).

[12] P. C. Searson and J. M. Macaulay, Nanotechnology **3**, 344 (1992).

[13] S. P. Duttagupta and P. M. Fauchet, in *Properties of Porous Silicon*, edited by L. Canham (INSPEC, Great Britain, 1997), Chap. 4, pp. 132–137.

[14] Y. Watanabe, Y. Arita, T. Yokoyama, and Y. Igarashi, J. Electrochem. Soc. **122**, 1351 (1975).

[15] N. W. Ashcroft and N. D. Mermin, *Solid State Physics* (Brooks/Cole Thomson Learning, USA, 1976).

[16] C. Pickering, M. I. J. Beale, D. J. Robbins, P. J. Pearson, and R. Greef, J. Phys. C: Solid State Phys. **17**, 6535 (1984).

[17] *Porous Silicon*, edited by Z. C. Feng and R. Tsu (World Scientific, Singapore, 1994).

[18] S. Borini, M. Rocchia, A. M. Rossi, L. Boarino, and G. Amato, Phys. Stat. Sol. (a) **202**, 1648 (2005).

[19] V. Lehman, F. Hofmann, F. Möller, and U. Grüning, Thin Solid Films **255**, 20 (1995).

[20] S. P. Zimin, Semiconductors **34**, 353 (2000).

[21] W. Lang, in *Properties of Porous Silicon*, edited by L. Canham (INSPEC, Great Britain, 1997), Chap. 4, pp. 138–140.

[22] Z. Gaburro, N. Doldosso, and L. Pavesi, in *Encyclopedia of Condensed Matter Physics*, edited by F. Bassani, J. Liedl, and P. Wyder (Elsevier, Amsterdam, 2005), Chap. Porous Silicon, pp. 391–401.

[23] Q. Chen, J. Zhu, G. Zhou, Z. T. Song, X. G. Li, and Y. Zhang, J. Phys.: Condens. Matter **8**, L753 (1996).

[24] H. Mizuno, H. Koyama, and N. Koshida, Appl. Phys. Lett. **69**, 3779 (1996).

[25] L. Tsybeskob, K. L. Moore, D. G. Hall, and P. M. Fauchet, Phys. Rev. B **54**, R8361 (1996).

[26] H. Föll, M. Christophersen, J. Carstensen, and G. Hasse, Mater. Sci. Eng., R **39**, 93 (2006).

[27] H. Föll, J. Carstensen, and S. Frey, J. Nanomater. **2006**, 1 (2006).

[28] D. Bellet, in *Properties of Porous Silicon*, edited by L. Canham (INSPEC, Great Britain, 1997), Chap. 4, pp. 127–131.

[29] T. Yonehara and K. Sakaguchi, Japanese International **4**, 10 (2001).

[30] S. Ottow, V. Lehmann, and H. Föll, J. Electrochem. Soc. **143**, 385 (1996).

[31] P. Steiner, F. Kozlowski, and W. Lang, Thin Solid Films **255**, 49 (1995).

[32] F. Müller, A. Birner, J. Schilling, U. Gösele, C. Kettner, and P. Hänggi, Phys. Stat. Sol. (a) **182**, 585 (2000).

[33] B. E. Collins, K.-P. S. Dancil, G. Abbi, and M. J. Sailor, Adv. Funct. Mater. **12**, 187 (2002).

[34] F. Cunin, T. A. Schmedake, J. R. Link, Y. Y. Li, J. Koh, S. N. Bhatia, and M. J. Sailor, Nat. Mater. **1**, 39 (2002).

[35] E. Richter, G. Fuhr, T. Müller, S. Shirley, S. Rogaschewski, K. Reimer, and C. Dell, J. Mater. Sci. - Mater. Med. **7**, 85 (1996).

[36] S. C. Bayliss, P. J. Harris, L. D. Buckberry, and C. Rousseau, J. Mater Sci. Lett. **16**, 737 (1997).

[37] W. Sun, J. E. Puzas, T. Sheu, and P. M. Fauchet, Phys. Stat. Sol. A **204**, 1429 (2007).

[38] L. Vaccari, D. Canton, N. Zaffaroni, R. Villa, M. Tormen, and E. di Fabrizio, Microelectron. Eng. **83**, 1598 (2006).

[39] F. Ravariu, C. Podaru, O. Nedelcu, C. Ravariu, and E. Manea, *CAS 2004 Proceedings.* (Piscataway, NJ, 2004).

[40] T. Laurell, J. Drott, L. Rosengren, and K. Lindstörm, Sens. Actuators, B **31**, 161 (1996).

[41] T. Z. Mengistu, L. DeSouza, and S. Morin, Chem. Commun. **45**, 5659 (2005).

[42] V. Lehmann, in *Properties of Porous Silicon*, edited by L. Canham (INSPEC, Great Britain, 1997), Chap. 12, pp. 390–396.

[43] V. Pacebutas, K. Grigoras, and A. Krotkus, *17th Nordic Semiconductor Meeting* (Trondheim, Norway, 1996).

[44] I. Kuzma-Filipek, F. Duerinckx, K. V. Nieuwenhuysen, G. Beaucame, J. Portmans, and R. Mertens, Phys. Stat. Sol. C **6**, 1745 (2009).

[45] K.-L. Chu, M. A. Shannon, and R. I. Masel, J. Micromch. Microeng. **17**, S243 (2007).

[46] D. Kovalev, V. Y. Timoshenko, N. Küzner, E. Gross, and F. Koch, Phys. Rev. Lett. **87**, 068301 (2001).

[47] G. G. Salgado, T. D. Becerril, H. J. Santiesteban, and E. R. Andrés, Opt. Mater. **29**, 51 (2006).

[48] C. Baratto, G. Faglia, G. Sberveglieri, Z. Gaburro, L. Pancheri, C. Oton, and L. Pavesi, Sensors **2**, 121 (2002).

[49] R. Angelucci, A. Poggi, L. Dori, A. Tagliani, G. C. Cardinali, F. Cortecelli, and M. Marisaldi, J. Porous Mater. **7**, 197 (2000).

[50] J. Dorvee and M. J. Sailor, Phys. Stat. Solidi (a) **202**, 1619 (2005).

[51] M. Bengtsson, S. Ekström, J. Drott, A. Collins, E. Csöregin, G. Marko-Varga, and T. Laurell, Phys. Stat. Sol. (a) **182**, 495 (2000).

[52] S. M. Weiss and P. M. Fauchet, IEEE J. Sel. Top. Quantum Electron. **12**, 1514 (2006).

[53] L. P. amd P. Dubos, Semicond. Sci. Technol. **12**, 570 (1996).

[54] E. Guillermain, V. Lysenko, and T. Benyattou, J. Lumin **121**, 319 (2006).

[55] C. Mazzoleni and L. Pavesi, Appl. Phys. Lett. **67**, 2983 (1995).

[56] M. Qian, X. Q. Bao, L. W. Wang, X. Lu, J. Shao, and X. S. Chen, J. Cryst. Growth **292**, 347 (2006).

[57] O. Bisi, S. Ossicini, and L. Pavesi, Surf. Sci. Rep. **38**, 1 (2000).

[58] J. Volk, N. Norbert, and I. Bársony, Phys. Stat. Sol. (a) **202**, 1707 (2005).

[59] J. Volk, T. L. Grand, I. Bársony, J. Gombköto, and J. J. Ramsden, J. Phys. D: Appl. Phys. **38**, 1313 (2005).

[60] J. Volk, J. Balázs, A. L. Tóth, and I. Bársony, Sens. Actuators, B **100**, 163 (2004).

[61] J. Volk, M. Friend, A. L. Tóth, and I. Bársony, Thin Solid Films **455-456**, 535 (2004).

[62] K. Barla, R. Hérino, G. Bomchil, J. C. Pfister, and A. Freund, J. Crys. Growth **68**, 727 (1984).

[63] F. G. Yost, Metall. Mater. Trans. A **14**, 947 (1983).

[64] R. L. Smith and G. E. Sandland, P I Mech. Eng. **102**, 623 (1922).

[65] R. J. M. Da Fonseca, J. M. Saurel, A. Foucaran, J. Camasel, E. Massone, T. Taliercio, and Y. Boumaiza, J. Mater. Sci. **30**, 35 (1995).

[66] R. J. M. Da Fonseca, J. M. Saurel, A. Foucaran, E. Massone, T. Taliercio, and J. Camassel, Thin Solid Films **225**, 155 (1995).

[67] G. T. Andrews, J. Zuk, H. Kiefte, M. J. Clouter, and E. Nossarzewska-Orlowska, Appl. Phys. Lett. **69**, 1217 (1996).

[68] M. G. Beghi, C. Bottani, G. Ghislotti, G. Amato, and L. Boarino, Thin Solid Films **297**, 110 (1997).

[69] D. J. Lockwood, M. H. Kuok, S. C. Ng, and Z. L. Rang, Phys. Rev. B. **60**, 8878 (1999).

[70] H. J. Fan, M. H. Kuok, R. B. S. C. Ng, J. M. Baribeau, J. F. Fraser, and D. J. Lockwood, Phys. Rev. C **65**, 165330, 1 (2002).

[71] H. J. Fan, M. H. Kuok, S. C. Ng, R. Boukherroub, and D. J. Lockwood, Semicond. Sci. Technol. **17**, 692 (2002).

[72] G. T. Andrews, M. J. Clouter, and J. Zuk, Semicond. Sci. and Technol. **19**, 1306 (2004).

[73] G. T. Andrews, A. M. Polomska, E. Vazsonyi, and J. Volk, Phys. Stat. Sol. A **204**, 1372 (2007).

[74] G. N. Aliev, B. Goller, D. Kovalev, and P. A. Snow, Phys. Stat. Sol. C **6**, 1670 (2009).

[75] G. Carlotti, D. Fioretto, L. Giovannini, and G. Socino, *Ultrasonic Symposium* (IEEE, USA, 1991), pp. 1079–1082.

[76] A. Yoshihara, W. Soe, and R. Yamamoto, Jpn. J. Appl. Phys., Part 1 **38**, 3072 (1999).

[77] R. Danner, R. P. Huebner, C. S. L. C. M. Grimsditch, and I. K. Schuller, Phys. Rev. B **33**, 3696 (1986).

[78] B. M. Clemens and G. L. Eesley, Phys. Rev. Lett. **61**, 2356 (1988).

[79] M. R. Scanlon, R. C. Cammarata, D. J. Keavney, J. W. Freeland, J. C. Walker, and C. Hayzelden, Appl. Phys. Lett. **66**, 46 (1995).

[80] S. Kumar, R. Bhadra, A. Fartash, M. Grimsditch, C. Kim, S. B. Qadri, and A. S. Edelstein, Phys. Rev. B **44**, 5905 (1991).

[81] M. Grimsditch and I. K. Schuller, in *Metallic Superlattices: Material Interfaces. Atomic Level Structure and Properties.*, edited by D. Wolf and S. Yip (Chapman

and Hall, United Kingdom, 1992), Chap. Elastic and structural properties of superlattices., pp. 354–363.

[82] J. Sapriel, J. C. Michel, J. C. Tolédano, R. Vacher, J. Kervarec, and A. Regreny, Phys. Rev. B **28**, 2007 (1983).

[83] M. Grimsditch, R. Bhadra, I. K. Schuller, F. Chambers, and G. Devane, Phys. Rev. B **42**, 2923 (1990).

[84] M. Grimsditch and F. Nizzoli, Phys. Rev. B **33**, 5891 (1986).

[85] G. Carlotti, G. Socino, H. Xia, K. J. Chen, Z. F. Li, W. Zheng, and X. K. Zhang, J. Phys.: Condens. Matter **6**, 6095 (1994).

[86] H. Xia, X. K. Zhang, K. J. Chen, G. X. Cheng, D. Feng, G. Socino, L. Palmieri, G. Carlottin, D. Fioretto, and F. Nizzoli, Phys. Rev. B **42**, 11288 (1990).

[87] H. Xia, G. Carlotti, G. Socino, K. J. Chen, W. Zhang, Z. F. Li, and X. K. Zhang, J. Appl. Phys. **75**, 475 (1994).

[88] S. Lee, J. R. Dutcher, G. I. Stegman, G. Duda, G. Wegner, and W. Knoll, Phys. Rev. Lett. **70**, 2427 (1993).

[89] F. Nizzoli, B. Hillebrands, S. Lee, G. I. Stegman, G. Duda, G. Wegner, and W. Knoll, Phys. Rev. B **40**, 3323 (1989).

[90] J. A. Forrest, A. C. Rowat, K. Dalnoki-Veress, J. R. Stevens, and J. R. Dutcher, J. Polym. Sci., Part B: Polym. Phys. **34**, 3009 (1996).

[91] G. Carlotti, D. Fioretto, L. Pamieri, G. Socino, A. Verdini, and C. Rigo, J. Phys.: Condens. Matter **8**, 2265 (1996).

[92] M. Mendik, M. Ospelt, H. von Känel, and P. Wachter, Appl. Surf. Sci. **50**, 303 (1991).

[93] A. de Bernabé, R. Jiménez, M. García-Hernández, and C. Prieto, Thin Solid Films **317**, 255 (1998).

[94] A. de Bernabé, C. Prieto, D. Cáceres, I. Vergara, A. G. Every, and H. E. Fisher, Phys. Stat. Sol. (a) **188**, 1023 (2001).

[95] A. M. Polomska and G. T. Andrews, Phys. Stat. Sol. C **6**, 1665 (2009).

[96] A. Kiuchi, B. Gelloz, A. Kojima, and N. Koshida, in *Materials Research Society Symposium Proceedings Series*, edited by L. Tsybeskov, D. Lockwood, C. Delerue, and M. Ichikawa (Warrendale, PA, 2005), Vol. 832.

[97] A. Reinhardt and P. A. Snow, Phys. Stat. Sol. A **204**, 1528 (2007).

[98] P. C. Chou and N. Pagano, *Elasticity. Tensor, Dyadic and Engineering Approaches* (D. van Nostrand Company, INC., USA, 1967).

[99] L. D. Landau and E. M. Lifshitz, *Theory of Elasticity*, Vol. 7 of *Landau and Lifshitz Course of Theoretical Physics*, 3rd ed. (Pergamon Press, Great Britain, 1986).

[100] P. L. Gould, *Introduction to Linear Elasticity*, 2nd ed. (Springer-Verlag, Berlin, 1994).

[101] B. A. Auld, *Acoustic Fields and Waves in Solids* (John Wiley & Sons, New York, USA, 1973), Vol. I.

[102] G. Nadeau, *Introduction to Elasticity* (Holt, Reinhart and Winston, Inc., USA, 1964).

[103] J. B. Marion and S. T. Thornton, *Classical Dynamics of Particles & Systems* (Harcourt Brace Jovanonich, Publishers, San Diego, 1988).

[104] A. Jeffrey and H. Dai, *Handbook of Mathematical Formulas and Integrals*, 4th ed. (Elsevier, USA, 2008).

[105] G. P. Srivastava, *The Physics of Phonons* (Adam Hilger, Bristol, England, 1990).

[106] C. Kittel, *Wstęp do Fizyki Ciała Stałego (Introduction to Solid State Physics)*, vii ed. (Wydawnictwo Naukowe PWN, Warszawa, 1999).

[107] J. L. Davis, *Wave Propagation in Solids and Fluids* (Springer-Verlag, New York, 1988).

[108] S. G. Lekhnitskii, *Theory of Elasticity of an Anisotropic Body* (MIR Publisher, Moscow, 1981).

[109] J. M. Carcione, *Wave Fields in Teal Media: Wave Propagation in Anisotropic, Anelastic and Porous Media* (Pergamon, Great Britain, 2001).

[110] J. F. Nye, *Physical Properties of Crystals.* (Clarendon Press, Great Britain, 1985).

[111] S. M. Rytov, Sov. Phys. JETP **2**, 466 (1956).

[112] G. E. Backus, J. Geophys. Res. **67**, 4427 (1962).

[113] E. Behrens, J. Acous. Soc. Am **42**, 378 (1967).

[114] E. Behrens, J. Acous. Soc. Am **42**, 367 (1967).

[115] M. Grimsditch, Phys. Rev. B **31**, 6818 (1985).

[116] H. Maogariec and A. Danescu, Phys. Status Solidi C **6**, 1680 (2009).

[117] *Dynamic Light Scattering*, edited by R. Pecora (Plenum Press, New York, 1985).

[118] *The Raman Effect*, edited by A. Anderson (Marcel Dekker, INC., New York, 1971), Vol. I.

[119] B. P. Stoicheff, in *Laser spectroscopy V. : Proceedings of the Fifth International Conference*, edited by A. R. W. McKellar, T. Oka, and B. P. Stoicheff (Springer-Verlag, New York, 1981), Chap. Brillouin Spectroscopy and Elastic Constants., pp. 980–1019.

[120] L. Brillouin, Ann. Phys. **349**, 177 (1914).

[121] J. R. Sandercock, in *Light Scattering in Solids III*, Vol. 51 of *Topics in Applied Physics*, edited by M. Cardona and G. Gntherodt (Springer-Verlag, Berlin, 1979), Chap. Trends in Brillouin Scattering: Studies of Opaque Materials, Supported Films and Central Modes, pp. 173–206.

[122] J. G. Dil, Rep. Prog. Phys. **45**, 287 (1982).

[123] J. A. Gonzalo, J. de Frutos, and J. Garciá, *Solid State Spectroscopies* (World Scientific, Singapore, 2002).

[124] A. M. Marvin, V. Bortolani, and F. Nizzoli, J. Phys. C: Solid St. Phys. **13**, 299 (1980).

[125] P. A. Fleury, in *Physical Acoustics. Principles and Methods.*, edited by W. P. Mason and R. N. Thurston (Academic Press, New York, 1970), Vol. vi, Chap. Light Scattering, pp. 2–64.

[126] P. H. Borcherds, Optica Acta **20**, 147 (1973).

[127] J. R. Sandercock, Solid State Comm. **26**, 547 (1978).

[128] B. E. A. Saleh and M. C. Teich, *Fundamentals of Photonics* (John Wiley Sons, INC., USA, 1991).

[129] W. Hayes, Contemp. Phys. **16**, 69 (1975).

[130] H. F. Pollard, *Sound Waves in Solids*, Vol. 9 of *Applied Physics Series* (Pion Limited, London, 1977).

[131] M. G. Cottam and D. R. Tilley, *Introduction to Surface and Superlattice Excitations* (Cambridge Univeristy Press, London, United Kingdom, 1989).

[132] G. Dresselhaus and A. Pine, Solid State Comm. **16**, 1001 (1975).

[133] S. Caponi, A. Fontana, M. Montagna, O. Pilla, F. Rossi, F. Terki, and T. Woignier, J. Non-Cryst. Solids **322**, 205149, 1 (2003).

[134] J. D. Achenbach, *Wave Propagation in Elastic Solids, Applied Mathematics and Mechanics* (North Holland Publishing, Netherlands, 1973).

[135] R. Loudon, in *Proceeding of the VII^{th} International Conference on Raman Spectroscopy*, edited by W. F. Murphy (North-Holland Publishing Company, Amsterdam, 1980), Chap. Light Scattering by Surface Vibrations on Solids and Liquids, pp. 368–370.

[136] P. R. Stoddart, J. C. Crowhurst, A. G. Every, and J. D. Comins, J. Opt. Soc. Am. B **15**, 2481 (1998).

[137] G. I. Stegeman and F. Nizzoli, in *Surface Excitatins*, Vol. 9 of *Modern Problems in Condensed Matter Sciences*, edited by V. M. Agranovich and R. Loudon (North-Holland Physics Publishing, ADDRESS, 1984), Chap. Surface Vibrations, pp. 199–378.

[138] R. Guerrero-Lemus, J. D. Moreno, and J. M. Martínez-Duart, Rev. Sci. Instrum. **67**, 3627 (1996).

[139] M. Balarin, O. Gamulin, M. Ivanda, V. Djerek, O. Celan, S. Music, M. Ristic, and K. Furic, J. Mol. Struc. **834-836**, 465 (2007).

[140] A. Halimaoui, Surf. Sci. **306**, L550 (1994).

[141] D. A. G. Bruggeman, Ann. Physik **24**, 636 (1935).

[142] S. Billat, M. Thönissen, R. Arens-Fischer, M. G. Berger, M. Krüger, and H. Lüth, Thin Solid Films **297**, 22 (1997).

[143] J. He, B. Djafari-Rouhani, and J. Sapriel, Phys. Rev. B **37**, 4086 (1988).

[144] J. M. Vaughan, *The Fabry-Pérot Interferometer* (Adam Hilger, Bristol, England, 1989).

[145] G. Hernandez, *Fabry-Pérot Interferometers, Cambridge Studies in Modern Optics* (Cambridge University Press, Great Britain, 1986).

[146] P. W. Milonni and J. H. Eberly, *Lasers* (John Wiley & Sons, New York-Toronto, 1988).

[147] J. R. Sandercock, *Tandem Fabry-Pérot Interferometer TFP-1. Operator Manual*, JRS Scientific Instruments, CH-8909 Zwillikon, Switzerland.

[148] D. K. Lynch and S. Mazuk, Appl. Optics **38**, 5229 (1999).

[149] A. M. Polomska, C. K. Young, G. T. Andrews, M. J. Clouter, A. Yin, and J. M. Xu, Appl. Phys. Lett. **90**, 201918 (2007).

[150] G. W. Farnell, in *Physical Acoustics*, edited by W. P. Mason and R. N. Thurston (Academic Press, New York, 1970), Vol. vi, Chap. Properties of Elastic Surface Waves, pp. 109–166.

[151] O. G. Sarbey, E. K. Frolova, R. D. Fedorovich, and D. B. Danko, Phys. Solid State **42**, 1240 (2000).

[152] R. Hull, in *Properties of Crystalline Silicon*, edited by A. George (Inspec, London, UK, 1999), Chap. Structural and Mechanical Properties., pp. 89–102.

[153] Y. Boumaiza, Z. Hadjoub, A. Doghmane, and L. Deboub, J. Mater. Sci. Lett. **18**, 295 (1999).

[154] C. C. Mathai, J. L. Gavartin, and A. A. Cafella, Thin Solid Films **255**, 174 (1995).

[155] J. J. Wortman and R. A. Evans, J. Appl. Phys. **36**, 153 (1965).

[156] I. A. Viktorov, *Rayleigh and Lamb Waves. Physical Theory and Applications* (Plenum Press, New York, 1967).

[157] G. W. Farnell, in *Topics in Applied Physics. Acoustic Surface Waves*, edited by A. A. Oliner (Springer-Verlag, Berlin - New York, 1978), Vol. 24, Chap. Types and Properties of Surface Waves., pp. 13–60.

[158] J. Dutcher, S. Lee, J. Kim, G. I. Stegman, and C. M. Falco, Phys. Rev. Lett. **65**, 1231 (1990).

[159] G. Carlotti, D. Fioretto, G. Socino, and E. Verona, J. Phys.: Condens. Matter **7**, 9147 (1995).

[160] G. W. Farnell and E. L. Adler, in *Physical Acoustics. Principles and Methods.*, edited by W. P. Mason and R. N. Thurston (Academic Press, New York, 1972), Vol. ix, Chap. Elastic Wave Propagation in Thin Layers, pp. 35–127.